

# **ELECTROCHEMICAL SENSOR FOR ANTIBIOTIC DETECTION**

**A Thesis Submitted  
in Partial Fulfillment of the Requirements for the  
Degree of**

**DOCTOR OF PHILOSOPHY**

**by**

**Divya Hudda**

**(2K20/PHDAC/501)**

**Under the Supervision of**

**Prof. D. Kumar**



**Department of Applied Chemistry  
DELHI TECHNOLOGICAL UNIVERSITY  
(Formerly Delhi College of Engineering)  
Shahbad Daultapur, Main Bawana Road, Delhi-110042, India**

**March 2026**



©Delhi Technological University-2026  
All rights reserved.







## ACKNOWLEDGEMENT

*First and foremost, I would like to extend my deepest gratitude to God, whose divine presence has been a guiding force throughout my life, providing me with the strength and wisdom to complete this journey. I am profoundly grateful to all the people who have entered my life, each one leaving an indelible mark and contributing to the realization of this thesis. Here, I would like to mention a few personalities and express my sincere gratitude from the bottom of my heart.*

*At the outset, I express my profound gratitude to my supervisor and Head of the Department, **Prof. D. Kumar**, Department of Applied Chemistry, Delhi Technological University, for being very humble and supportive all the time, and for their invaluable guidance, patience, and encouragement throughout this journey. I am deeply honoured to have worked under the guidance of such an excellent, enthusiastic, and distinguished supervisor. Their unwavering encouragement, constant support, meticulous supervision, and constructive criticism have been instrumental in carving another milestone in my academic journey. I feel truly privileged to have benefited from their outstanding supervision, insights, and expertise that were crucial to the successful completion of this work.*

*I express my sincere gratitude to **Prof. Ram Singh**, Department of Applied Chemistry, and **Prof. Jai Gopal Sharma**, Department of Biotechnology, Delhi Technological University, for allowing me to conduct electrochemistry work in their laboratories and for providing the necessary facilities.*

*I extend my sincere thanks to **Prof. Anil Kumar**, former Head of the Department of Applied Chemistry at Delhi Technological University, for providing the necessary research facilities within the department. It is my pleasure to express my sincere thanks to all the*



*faculty members of the Department of Applied Chemistry for their continuous encouragement and help during my research work. I am also grateful to the **technical and non-technical staff** for their timely support and cooperation whenever required.*

*Further, I extend a very special thanks to **Dr. C.M. Pandey**, Assistant Professor, SGT University, Gurugram (Haryana), for his continuous guidance during this journey. I was fortunate to have a great work atmosphere in the laboratory, which helped me complete my tasks properly. I would like to express my heartfelt gratitude to my dear former and current lab members **Dr. Owais Jalil, Dr. Deeksha Thakur, Dr. Sakshi Verma, Dr. Saroj Paneru, Dr. Sweety, Dr. Manu, Dr. Ritu Sharma, Ms. Tanushee, Ms. Tanvi, Ms. Nishtha, Ms. Vaishali, Mr. Majeed, Mr. Sunil Tomar, Mr. Kundan Singh, Ms. Anupama, Ms. Tanu Rajput, and Ms. Yashaswini** for their unwavering support in every possible way to carry forward my research work.*

*I am especially thankful to **Mr. Anurag Kaushik and Mr. Jasveer Singh**, colleagues from the Department of Applied Physics, at DTU, for their support in arranging the characterization facilities.*

*A journey is always made more memorable with some crucial friends; now it's their turn. I would like to highlight the cheerful company and consistently supportive roles of **Dr. Deeksha Thakur, Ms. Tanushee, Dr. Ramesh Kumar, Ms. Sarla, and Ms. Kanika**. Your camaraderie made this journey enjoyable and memorable.*

*It is impossible to reach any milestone without the support of family. Finally, I would like to express my gratitude to my family for their unconditional love, support, and encouragement throughout every phase of my life. I express my gratefulness to my father, **Mr. Ashok Hudda**, and my mother, **Mrs. Ritu Hudda**, who always believed in me and supported me to go out of the box to grow. I'm grateful to my grandparents, **Mr. Ramphal Hudda and Mrs. Roshni Hudda**, and my maternal grandmother, **Mrs. Shyamo Devi**, for*



*their continual love and encouragement. I'm grateful to my beloved sibling, **Mr. Gaurav Hudda**, for being my pillar of strength in my life.*

*I'm thankful to my uncle **Suryakant Kumar** for his constant help and support throughout this journey. I'm also grateful to my cousins **Kunal, Rupal, Aniket, Akshita, Vedita, and Rishita** for their unconditional love and support.*

*At last, I gratefully acknowledge the **Delhi Technological University (DTU)**, Delhi, for financial support and for extending all the necessary facilities.*

*I am deeply grateful to the divine for blessing me with the strength and wisdom to walk on this journey. To all the wonderful people who have come into my life during this road, I am profoundly thankful for your support, encouragement, and love. Your presence has made this accomplishment possible, and I carry your kindness with me always.*

*May we continue to grow, support, learn, and achieve together.*

*With deepest gratitude to all!!!*

**(Divya Hudda)**





# DELHI TECHNOLOGICAL UNIVERSITY

**Formerly Delhi College of Engineering**

(Under Delhi Act 6 of 2009, Govt. of NCT of Delhi)

Shahbad Daultapur, Bawana Road, Delhi-110 042

---

## CANDIDATE'S DECLARATION

I, **Divya Hudda (Reg. No.: 2K20/PhDAC/501)** hereby certify that the work which is being presented in the thesis entitled “*Electrochemical Sensor for Antibiotic Detection*” in partial fulfillment of the requirements for the award of the Degree of Doctor of Philosophy, submitted in the Department of *Applied Chemistry*, Delhi Technological University (Formerly Delhi College of Engineering), Delhi is an authentic record of my own work carried out during the period from January 2021 to December 2025 under the supervision of **Prof. D. Kumar**, Department of Applied Chemistry, Delhi Technological University, Delhi.

The matter presented in the thesis has not been submitted by me for the award of any degree of this or any other Institute.

**Divya Hudda**  
(Reg. No.: 2K20/PhDAC/501)





# DELHI TECHNOLOGICAL UNIVERSITY

Formerly Delhi College of Engineering  
(Under Delhi Act 6 of 2009, Govt. of NCT of Delhi  
Shahbad Daulatpur, Bawana Road, Delhi-110 042

---

## CERTIFICATE BY THE SUPERVISOR

Certified that *Ms. Divya Hudda (Reg. No.: 2K20/PhDAC/501)* has carried out her research work presented in this thesis entitled “*Electrochemical Sensor for Antibiotic Detection*” for the award of the degree of *Doctor of Philosophy* from the Department of Applied Chemistry, Delhi Technological University, Delhi, under my supervision. The thesis embodies results of original work, and studies are carried out by the candidate herself, and the contents of the thesis do not form the basis for the award of any other degree to the candidate or to anybody else from this or any other University/Institution.

**Prof. D. Kumar**

*Supervisor*

*Department of Applied Chemistry*

*Delhi Technological University*

*Delhi-110042, India*

**Prof. D. Kumar**

*Head, Department of Applied Chemistry*

*Delhi Technological University*

*Delhi-110042, India*



## ABSTRACT

The research work presented in this thesis discusses the fabrication of an electrochemical sensor utilizing a molecularly imprinted polymer approach, which provides quantitative information for detecting antibiotic residues in various fields. Antibiotics are a class of chemical compounds that are extensively used to cure and prevent infectious diseases in humans, animals, and aquaculture due to their bacteriostatic and bactericidal actions. However, most of these antibiotics are non-biodegradable and can be excreted in the form of metabolites in the environment through human or animal excreta, wastewater discharge, and agricultural land runoff. Additionally, the misuse of veterinary medicine can lead to residues in animal-derived foods, including milk, eggs, meat, and fish. These residual antibiotics or their metabolites can lead to several problems, including bacterial resistance, allergic reactions, liver damage, and cancer, thus posing a huge threat to human and animal health. Therefore, developing a sensitive and effective detection technique is crucial and necessary to accurately monitor trace amounts of antibiotic contamination, thereby protecting living beings from its injurious effects. The analytical methods commonly used for antibiotic detection are based on spectroscopic and chromatographic techniques, which have certain limitations, including long analysis times, complexity, and high expenses associated with operating highly specialized equipment, as well as low sensitivity. To overcome these limitations, we require a new method that is simple, cost-effective, has a low detection limit, and is easy to use.

Recently, electrochemical sensors have emerged as an attractive alternative to these conventional techniques due to their fast response, high sensitivity, the possibility of real-time analysis, and cost-effectiveness. However, natural receptors, such as antibodies, enzymes, and hormones, are utilized by these electrochemical sensors as their recognition components. Despite their high selectivity and sensitivity, they remain costly and sensitive to environmental factors. In this context, a molecularly imprinted polymer (MIP) is a suitable alternative due to



its ease of preparation, high selectivity and low cost. MIPs are synthetic materials with high recognition binding cavities that target the analyte. MIP films are fabricated via the electropolymerization of functional monomers in presence of template molecules (analyte) on the surface of electrode. Following electropolymerization, the embedded template molecules are extracted from the polymer matrix, leaving behind the cavities that resemble the template molecules' size, shape, and functional groups. Although MIPs have garnered considerable attention due to their unique recognition ability and high selectivity efficiency, they have several drawbacks, including low sensitivity, poor adhesion to the electrode surface, and high diffusion barriers. In this regard, incorporating 2D materials with the MIP electrochemical sensor can enhance the imprinted cavities and facilitate electron transfer.

Further, a novel two-dimensional material, MXene, an emerging transition metal carbide or carbonitrides, has been recognized for its electrochemical applications due to its high surface-to-volume ratio, superior hydrophilicity, good electrical conductivity, large specific area, and superior electron transport ability. Integrating MXene with other components or functionalizing its surface can impart additional advantageous properties to the resulting composites through synergistic effects, thus enhancing the overall biosensing capabilities. This work mainly focuses on the synthesis, characterization and application of MXene ( $\text{Ti}_3\text{C}_2\text{T}_x$ ) and its composites with  $\text{TiO}_2$ ,  $\text{CuS}$ , and  $\text{Ag}$  for the fabrication of a highly sensitive and selective MIP-based electrochemical sensor for the detection of antibiotic, i.e., levofloxacin. The synthesized material was electrophoretically deposited on the ITO-glass surface and then the modified electrode was coupled with the MIP film through electropolymerization. Furthermore, electrochemical response studies were performed using DPV and EIS techniques. Finally, the applicability of the fabricated platforms was validated with spiked real samples which prove their efficiency.



## List of Research Publications Included in Thesis

- ❖ **Divya Hudda**, Devendra Kumar, Molecularly imprinted polypyrrole decorated  $\text{Ti}_3\text{C}_2\text{T}_x$  electrochemical sensor for highly selective and sensitive detection of levofloxacin, *Journal of Materials Science*, 59 (2024) 21684-21695.
- ❖ **Divya Hudda**, Devendra Kumar, Titanium dioxide grafted MXene-based molecularly imprinted electrochemical sensor for the ultrasensitive determination of levofloxacin, *Journal of Solid State Electrochemistry*, 29 (2025) 5283-5295.
- ❖ **Divya Hudda**, Devendra Kumar, Fabrication of highly sensitive  $\text{CuS}@\text{Ti}_3\text{C}_2\text{T}_x$  supported molecularly imprinted impedimetric sensing platform for the ultra-trace detection of levofloxacin (Communicated).
- ❖ **Divya Hudda**, Devendra Kumar, A highly stable molecularly imprinted polymer-coated  $\text{Ag}/\text{TiO}_2\text{-Ti}_3\text{C}_2\text{T}_x$  nanohybrid electrochemical sensing platform for the selective analysis of levofloxacin determination (Communicated).



# TABLE OF CONTENTS

---

<b>Contents</b>	<b>Page No.</b>
<i>ACKNOWLEDGEMENTS</i>	<i>iv</i>
<i>CANDIDATE'S DECLARATION</i>	<i>vii</i>
<i>CERTIFICATE BY SUPERVISOR</i>	<i>viii</i>
<i>ABSTRACT</i>	<i>ix</i>
<i>LIST OF RESEARCH PUBLICATIONS INCLUDED IN THESIS</i>	<i>xi</i>
<i>TABLE OF CONTENTS</i>	<i>xii</i>
<i>LIST OF TABLES</i>	<i>xvii</i>
<i>LIST OF FIGURES</i>	<i>xviii</i>
<i>LIST OF ABBREVIATIONS</i>	<i>xxiv</i>
<b>Chapter 1: Introduction &amp; Literature Review</b>	<b>01-39</b>
<b>1.1 Introduction to Antibiotics</b>	<b>01</b>
<b>1.2 Classification of Antibiotics</b>	<b>02</b>
1.2.1 Based on Sources	02
1.2.2 Based on the Spectrum of Activity	02
1.2.3 Based on Chemical Structure	03
1.2.4 Based on the Mechanism of Action	03
<b>1.3 Benefits of Antibiotics in Humans and Livestock/Animals</b>	<b>05</b>
<b>1.4 Impact of Antibiotics on Human Health and Environment</b>	<b>05</b>
<b>1.5 Detection Techniques of Antibiotics</b>	<b>06</b>
1.5.1 Conventional Detection Methods	06
1.5.2 Sensors: Advanced Detection Tool	07
<b>1.6 Molecularly Imprinted Polymers (MIPs)</b>	<b>10</b>
1.6.1 Working Principle of MIP Based Electrochemical Sensor	11
1.6.2 Imprinting Approaches	12
1.6.2.1 Covalent Imprinting	12



1.6.2.2	Non-Covalent Imprinting	13
1.6.2.3	Semi-Covalent Imprinting	13
1.6.3	Polymerization Techniques for MIP Synthesis	13
1.6.3.1	Bulk Polymerization	13
1.6.3.2	Precipitation Polymerization	14
1.6.3.3	Sol-gel Polymerization	14
1.6.3.4	Electrochemical Polymerization	14
1.6.4	Challenges in MIP-Based Electrochemical Sensors	15
<b>1.7</b>	<b>Two-dimensional (2D) Materials as Electrode Modifiers</b>	<b>15</b>
1.7.1	MXene	18
1.7.2	Properties of MXene	19
1.7.2.1	Mechanical Properties	19
1.7.2.2	Thermal and Electrical Properties	20
1.7.2.3	Structural Properties	20
1.7.2.4	Optical Properties	20
<b>1.8</b>	<b>Synthesis of MXene</b>	<b>20</b>
1.8.1	Top-Down Methods	21
1.8.1.1	HF Etching	21
1.8.1.2	Etching with Fluoride Salt	22
1.8.1.3	Electrochemical Etching	22
1.8.1.4	Molten-Salt Etching	23
1.8.1.5	Hydrothermal Etching	23
1.8.1.6	Other Advanced Etching Methods	24
1.8.2	Bottom-Up Methods	25
1.8.2.1	Chemical Vapour Deposition (CVD)	25
1.8.2.2	Pulsed Laser Deposition	25
<b>1.9</b>	<b>Application of MXenes and MXene-Based Composites for Antibiotic Detection</b>	<b>26</b>
<b>1.10</b>	<b>Objectives</b>	<b>28</b>
<b>1.11</b>	<b>Thesis organization</b>	<b>29</b>
	<b>References</b>	<b>32</b>
	<b>Chapter 2: Materials and Experimental Techniques</b>	<b>40-54</b>
<b>2.1</b>	<b>Introduction</b>	<b>40</b>



<b>2.2</b>	<b>Materials</b>	<b>40</b>
2.2.1	Chemicals	40
2.2.2	Buffers	41
<b>2.3</b>	<b>Analytical Techniques</b>	<b>41</b>
2.3.1	X-Ray Diffraction (XRD)	41
2.3.2	Fourier Transform Infrared (FT-IR) Spectroscopy	43
2.3.3	Raman Spectroscopy	44
2.3.4	Field- Emission Scanning Electron Microscopy (FESEM)	45
2.3.5	Energy Dispersive X-ray (EDX) Analysis	46
2.3.6	Electrochemical Techniques	47
2.3.6.1	Cyclic Voltammetry (CV)	48
2.3.6.2	Electrochemical Impedance Spectroscopy (EIS)	49
2.3.6.3	Differential Pulse Voltammetry (DPV)	50
<b>2.4</b>	<b>Protocols Used for the Determination of Various Performance-related Parameters for MXene and its Composite-Based Electrochemical Sensor</b>	<b>51</b>
2.4.1	Linear range, Detection Limit, and Sensitivity	51
2.4.2	Selectivity, Reproducibility and Stability	52
	<b>References</b>	<b>53</b>
<b>Chapter 3:</b>	<b>MXene-based Molecularly Imprinted Electrochemical Sensor for Antibiotic Detection</b>	<b>55-68</b>
<b>3.1</b>	<b>Introduction</b>	<b>55</b>
<b>3.2</b>	<b>Experimental Details</b>	<b>56</b>
3.2.1	Synthesis of $Ti_3C_2T_x$	56
3.2.2	Electrophoretic Deposition of $Ti_3C_2T_x$ on ITO	56
3.2.3	Fabrication of MIP-Based Electrochemical Sensor	56
<b>3.3</b>	<b>Results and Discussion</b>	<b>57</b>
3.3.1	Structural and Morphological Studies	57
3.3.2	Electrochemical Characterization	59
3.3.3	Optimization Studies	61
3.3.4	Performance of the MIP Sensor for LEV Detection	63
3.3.5	Selectivity, Reproducibility, and Stability Studies	64
3.3.6	Real Sample Analysis	66



<b>3.4 Conclusion</b>	<b>67</b>
<b>References</b>	<b>68</b>
<b>Chapter 4: Titanium Dioxide Anchored MXene-based Molecularly Imprinted Electrochemical Sensor for Antibiotic Detection</b>	<b>69-84</b>
<b>4.1 Introduction</b>	<b>69</b>
<b>4.2 Experimental Details</b>	<b>70</b>
4.2.1 Synthesis of $Ti_3C_2T_x$ and $TiO_2-Ti_3C_2T_x$ Composite	70
4.2.2 Electrophoretic Deposition of $TiO_2-Ti_3C_2T_x$	70
4.2.3 Fabrication of $TiO_2-Ti_3C_2T_x$ Modified MIP-Based Electrochemical Sensing Platform	70
<b>4.3 Results and Discussion</b>	<b>71</b>
4.3.1 Structural Studies	71
4.3.2 Morphological Studies	72
4.3.3 Electrochemical Studies	74
4.3.4 Optimization Parameters	77
4.3.5 Analytical Performance of $TiO_2-Ti_3C_2T_x/ITO@MIP$	79
4.3.6 Interference, Reproducibility, Repeatability, and Stability Analysis	80
4.3.7 Real Sample Analysis	82
<b>4.4 Conclusion</b>	<b>83</b>
<b>References</b>	<b>84</b>
<b>Chapter 5: CuS Embedded <math>Ti_3C_2T_x</math>- based Molecularly Imprinted Impedimetric Sensor for Levofloxacin Detection</b>	<b>85-99</b>
<b>5.1 Introduction</b>	<b>85</b>
<b>5.2 Experimental Details</b>	<b>86</b>
5.2.1 Synthesis of CuS and $CuS/Ti_3C_2T_x$	86
5.2.2 Electrophoretic Deposition of $CuS/Ti_3C_2T_x$	86
5.2.3 Fabrication of $CuS/Ti_3C_2T_x/ITO@MIP$ Sensing Platform	87
<b>5.3 Results and Discussion</b>	<b>87</b>
5.3.1 Structural Characterization	87



5.3.2	Morphological Characterization	88
5.3.3	Electrochemical Characterization	89
5.3.4	Optimization of Experimental Conditions	93
5.3.5	Electrochemical Response Studies for LEV Determination	95
5.3.6	Selectivity, Reproducibility, and Stability Studies	96
5.3.7	Real Sample Analysis	97
<b>5.4</b>	<b>Conclusion</b>	<b>98</b>
	<b>References</b>	<b>99</b>
<b>Chapter 6: Ag/TiO<sub>2</sub>-Ti<sub>3</sub>C<sub>2</sub>T<sub>x</sub> Modified Molecularly Imprinted Electrochemical Sensor for Levofloxacin Detection</b>		<b>100-115</b>
<b>6.1</b>	<b>Introduction</b>	<b>100</b>
<b>6.2</b>	<b>Experimental Details</b>	<b>101</b>
6.2.1	Synthesis of TiO <sub>2</sub> -Ti <sub>3</sub> C <sub>2</sub> T <sub>x</sub> and Ag/TiO <sub>2</sub> -Ti <sub>3</sub> C <sub>2</sub> T <sub>x</sub>	101
6.2.2	Electrophoretic Deposition of Ag/TiO <sub>2</sub> -Ti <sub>3</sub> C <sub>2</sub> T <sub>x</sub> Composite	101
6.2.3	Preparation of Ag/TiO <sub>2</sub> -Ti <sub>3</sub> C <sub>2</sub> T <sub>x</sub> /ITO@MIP Sensor	101
<b>6.3</b>	<b>Results and Discussion</b>	<b>102</b>
6.3.1	Structural and Morphological Studies	102
6.3.2	Electrochemical Characterization	104
6.3.3	Optimization of Experimental Parameters	108
6.3.4	Analytical Performance of the Fabricated MIP Sensor for LEV Detection	110
6.3.5	Selectivity, Reproducibility, Repeatability, and Stability Analysis	111
6.3.6	Real Sample Analysis	113
<b>6.4</b>	<b>Conclusion</b>	<b>114</b>
	<b>References</b>	<b>115</b>
<b>Chapter 7: Conclusion, Future Scope, and Social Impact</b>		<b>116-119</b>
<b>7.1</b>	<b>Conclusion</b>	<b>116</b>
<b>7.2</b>	<b>Future Scope</b>	<b>118</b>
<b>7.3</b>	<b>Social impact</b>	<b>119</b>
	<b>List of Publications</b>	<b>120</b>
	<b>Plagiarism Certificate</b>	<b>125</b>
	<b>Curriculum Vitae</b>	<b>127</b>



## LIST OF TABLES

<b>Table No.</b>	<b>Table Captions</b>	<b>Page No.</b>
1.1	Recent advances in electrochemical sensors for antibiotic detection	27
3.1	Detection of LEV in spiked real samples using $\text{Ti}_3\text{C}_2\text{T}_x/\text{ITO}@MIP$ electrode	66
4.1	Detection of LEV in spiked real samples using $\text{TiO}_2\text{-Ti}_3\text{C}_2\text{T}_x/\text{ITO}@MIP$ electrode	82
5.1	Data of LEV in spiked real samples using $\text{CuS}/\text{Ti}_3\text{C}_2\text{T}_x/\text{ITO}@MIP$ electrode	98
6.1	Data of LEV in spiked real samples using $\text{Ag}/\text{TiO}_2\text{-Ti}_3\text{C}_2\text{T}_x/\text{ITO}@MIP$ electrode	113



# LIST OF FIGURES

<b>Figure No.</b>	<b>Figure Captions</b>	<b>Page No.</b>
1.1	A brief history of antibiotics	1
1.2	Chemical structures of different classes of antibiotics	3
1.3	Mechanism of antibiotics function	4
1.4	Schematic illustration of the circulation of antibiotics in the environment	6
1.5	Conventional techniques for antibiotic detection	7
1.6	Schematic representation of a sensor	8
1.7	Classification of sensors	10
1.8	A pictorial view of the MIP film	11
1.9	Diagrammatic illustration of 2D materials along with their structures	16
1.10	Schematic representation of the characteristics and synthesis methods of 2D materials	17
1.11	General structure of $Ti_3C_2T_x$	19
1.12	General synthesis of MXene	21
2.1	(A) Pictorial illustration of XRD (B) XRD pattern of $TiAl_3C_2$ , $Ti_3C_2T_x$ and $TiO_2-Ti_3C_2T_x$	42
2.2	(A) Schematic illustration of a Michelson interferometer (B) FT-IR spectra of $Ti_3C_2T_x$	44
2.3	(A) Schematic diagram of a Raman spectrometer (B) Raman spectrum of $Ti_3C_2T_x$ and $TiO_2-Ti_3C_2T_x$	45



2.4	(A) Pictorial view of FESEM (B) FESEM image of $Ti_3C_2T_x$	46
2.5	Schematic diagram of the working of the Potentiostat	48
3.1	Schematic representation for the fabrication of $Ti_3C_2T_x$ -based MIP sensor	55
3.2	(A) XRD pattern of $Ti_3AlC_2$ (black curve) and $Ti_3C_2T_x$ (red curve) (B) FTIR spectra of $Ti_3C_2T_x$	57
3.3	FESEM micrographs of (A) $Ti_3AlC_2$ (B) $Ti_3C_2T_x$ (C) $Ti_3C_2T_x/ITO@MIP$ before elution (D) $Ti_3C_2T_x/ITO@MIP$ after elution; EDX analysis of (E) $Ti_3AlC_2$ and (F) $Ti_3C_2T_x$	58
3.4	(A) CV plots of various modified electrodes: (a) ITO (b) $Ti_3C_2T_x/ITO$ (c) $Ti_3C_2T_x/ITO@MIP$ before elution (d) $Ti_3C_2T_x/ITO@MIP$ after elution (e) $Ti_3C_2T_x/ITO@MIP$ after rebinding and (f) $Ti_3C_2T_x/ITO@NIP$ after elution (B) scan rate studies (10-300 mV/s), (C) linear plot of redox peak potential with log of scan rate and (D) linear plot of peak current vs. square root of scan rate for $Ti_3C_2T_x/ITO@MIP$ electrode	60
3.5	Optimization key parameters for (A) electropolymerization solution pH (B) template to functional monomer (LEV: Pyrrole) concentration ratio (C) number of scan cycles (D) scan rate (E) elution time and (F) adsorption time $Ti_3C_2T_x/ITO@MIP$ for LEV	63
3.6	(A) DPV response study of $Ti_3C_2T_x/ITO@MIP$ electrode after incubation at various concentrations (1 pM-100 nM; top to bottom) of LEV and (B) Plot depicting the linearity between $\Delta I$ and $\log(C_{LEV})$	64
3.7	(A) Interference study of $Ti_3C_2T_x/ITO@MIP$ electrode in the presence of other interfering species (10 nM) with respect to LEV (1 nM), (B) Reproducibility of the fabricated $Ti_3C_2T_x/ITO@MIP$ sensor and (C) Stability of the $Ti_3C_2T_x/ITO@MIP$ sensor	65



4.1	Diagrammatic illustration showing the fabrication of TiO <sub>2</sub> -Ti <sub>3</sub> C <sub>2</sub> T <sub>x</sub> -based MIP electrochemical sensor	69
	(A) XRD spectra of Ti <sub>3</sub> AlC <sub>2</sub> (black), Ti <sub>3</sub> C <sub>2</sub> T <sub>x</sub> (red), TiO <sub>2</sub> -Ti <sub>3</sub> C <sub>2</sub> T <sub>x</sub> (blue)	
4.2	(B) FTIR and (C) Raman spectra of Ti <sub>3</sub> C <sub>2</sub> T <sub>x</sub> (black) and TiO <sub>2</sub> -Ti <sub>3</sub> C <sub>2</sub> T <sub>x</sub> (red)	72
4.3	FESEM images of (A) Ti <sub>3</sub> AlC <sub>2</sub> (B) Ti <sub>3</sub> C <sub>2</sub> T <sub>x</sub> (C) TiO <sub>2</sub> -Ti <sub>3</sub> C <sub>2</sub> T <sub>x</sub> (D) TiO <sub>2</sub> -Ti <sub>3</sub> C <sub>2</sub> T <sub>x</sub> /ITO@MIP before elution (E) TiO <sub>2</sub> -Ti <sub>3</sub> C <sub>2</sub> T <sub>x</sub> /ITO@MIP after elution and (F) EDX spectra of TiO <sub>2</sub> -Ti <sub>3</sub> C <sub>2</sub> T <sub>x</sub>	73
4.4	(A) CV plots and (B) EIS curves of various modified electrodes: (a) ITO (b) Ti <sub>3</sub> C <sub>2</sub> T <sub>x</sub> /ITO (c) TiO <sub>2</sub> -Ti <sub>3</sub> C <sub>2</sub> T <sub>x</sub> /ITO (d) TiO <sub>2</sub> -Ti <sub>3</sub> C <sub>2</sub> T <sub>x</sub> /ITO@MIP before elution (e) TiO <sub>2</sub> -Ti <sub>3</sub> C <sub>2</sub> T <sub>x</sub> /ITO@MIP after elution (f) TiO <sub>2</sub> -Ti <sub>3</sub> C <sub>2</sub> T <sub>x</sub> /ITO@MIP after rebinding and (g) TiO <sub>2</sub> -Ti <sub>3</sub> C <sub>2</sub> T <sub>x</sub> /ITO@NIP after elution	75
4.5	(A) CV curves of scan rate studies (10-300 mV/s) (B) linear curves of redox peak potential with log of scan rate and (C) linear curves of peak current vs. square root of scan rate for TiO <sub>2</sub> -Ti <sub>3</sub> C <sub>2</sub> T <sub>x</sub> /ITO@MIP electrode	76
4.6	Optimization key parameters for preparing TiO <sub>2</sub> -Ti <sub>3</sub> C <sub>2</sub> T <sub>x</sub> /ITO@MIP electrode: (A) Effect of electropolymerization solution pH (B) concentration ratio of template to monomer (C) scan cycles (D) scan rate (E) elution time and (F) incubation time	79
4.7	(A) DPV response study of fabricated TiO <sub>2</sub> -Ti <sub>3</sub> C <sub>2</sub> T <sub>x</sub> /ITO@MIP electrode at various LEV concentrations (1 pM-100 nM) and (B) calibration plot depicting a linear behaviour between the ΔI and log (C <sub>LEV</sub> )	80
4.8	(A) Interference study of TiO <sub>2</sub> -Ti <sub>3</sub> C <sub>2</sub> T <sub>x</sub> /ITO@MIP electrode in the presence of other interfering species (10 nM) along with 0.1 nM LEV (B)	81



	Reproducibility of the fabricated $\text{TiO}_2\text{-Ti}_3\text{C}_2\text{T}_x/\text{ITO@MIP}$ sensor (C)	
	Repeatability of the fabricated $\text{TiO}_2\text{-Ti}_3\text{C}_2\text{T}_x/\text{ITO@MIP}$ sensor and (D)	
	Shelf-life study of the $\text{TiO}_2\text{-Ti}_3\text{C}_2\text{T}_x/\text{ITO@MIP}$ sensor	
5.1	Scheme representing the $\text{CuS}/\text{Ti}_3\text{C}_2\text{T}_x$ modified MIP impedimetric sensor for LEV detection	85
5.2	(A) XRD pattern and (B) FTIR spectra of $\text{Ti}_3\text{C}_2\text{T}_x$ (black), CuS (red), and $\text{CuS}/\text{Ti}_3\text{C}_2\text{T}_x$ (blue)	88
5.3	FESEM micrographs of (A) $\text{Ti}_3\text{AlC}_2$ (B) $\text{Ti}_3\text{C}_2\text{T}_x$ (C) $\text{CuS}/\text{Ti}_3\text{C}_2\text{T}_x$ (D) $\text{CuS}/\text{Ti}_3\text{C}_2\text{T}_x/\text{ITO@MIP}$ before elution (E) $\text{CuS}/\text{Ti}_3\text{C}_2\text{T}_x/\text{ITO@MIP}$ after elution and (F) EDX analysis of $\text{CuS}/\text{Ti}_3\text{C}_2\text{T}_x$	89
5.4	(A) CV plots and (B) EIS curves of various modified electrodes: (a) ITO (b) $\text{Ti}_3\text{C}_2\text{T}_x/\text{ITO}$ (c) $\text{CuS}/\text{Ti}_3\text{C}_2\text{T}_x/\text{ITO}$ (d) $\text{CuS}/\text{Ti}_3\text{C}_2\text{T}_x/\text{ITO@MIP}$ before elution (e) $\text{CuS}/\text{Ti}_3\text{C}_2\text{T}_x/\text{ITO@MIP}$ after elution (f) $\text{CuS}/\text{Ti}_3\text{C}_2\text{T}_x/\text{ITO@MIP}$ after rebinding, and (g) $\text{CuS}/\text{Ti}_3\text{C}_2\text{T}_x/\text{ITO@NIP}$ after elution	91
5.5	(A) Cyclic voltammograms curves at various scan rates (10-300 mV/s) (B) linear curves of redox peak potential with log of scan rate, and (C) linear curves of peak current against square root of scan rate for $\text{CuS}/\text{Ti}_3\text{C}_2\text{T}_x/\text{ITO@MIP}$ electrode	92
5.6	Optimization of the MIP fabrication conditions: Effect of (A) electropolymerization solution pH value (B) template to functional monomer concentration ratio (C) scan cycles (D) MIP scan rate (E) elution time and (F) incubation time of $\text{CuS}/\text{Ti}_3\text{C}_2\text{T}_x/\text{ITO@MIP}$ for LEV	94
5.7	(A) Electrochemical response of the fabricated $\text{CuS}/\text{Ti}_3\text{C}_2\text{T}_x/\text{ITO@MIP}$ sensor against various LEV concentrations (0.01-1000 pM) using the EIS	95



	method and <b>(B)</b> Linear fit curve between and the logarithm of different LEV concentrations and $\Delta R_{ct}$	
	<b>(A)</b> Selectivity study of CuS/Ti <sub>3</sub> C <sub>2</sub> T <sub>x</sub> /ITO@MIP sensor towards LEV and other interfering species, <b>(B)</b> Reproducibility study of CuS/Ti <sub>3</sub> C <sub>2</sub> T <sub>x</sub> /ITO@MIP sensor towards LEV using five different electrodes and <b>(C)</b> Stability of CuS/Ti <sub>3</sub> C <sub>2</sub> T <sub>x</sub> /ITO@MIP sensor over a period of 6 weeks	97
<b>6.1</b>	Scheme depicting the fabrication of Ag/TiO <sub>2</sub> -Ti <sub>3</sub> C <sub>2</sub> T <sub>x</sub> modified MIP electrochemical sensor	100
<b>6.2</b>	<b>(A)</b> XRD spectra of Ti <sub>3</sub> AlC <sub>2</sub> (black curve), Ti <sub>3</sub> C <sub>2</sub> T <sub>x</sub> (red curve), TiO <sub>2</sub> -Ti <sub>3</sub> C <sub>2</sub> T <sub>x</sub> (blue curve), and Ag/TiO <sub>2</sub> -Ti <sub>3</sub> C <sub>2</sub> T <sub>x</sub> (green curve) <b>(B)</b> FTIR spectra of Ti <sub>3</sub> C <sub>2</sub> T <sub>x</sub> (black curve) and Ag/TiO <sub>2</sub> -Ti <sub>3</sub> C <sub>2</sub> T <sub>x</sub> (green curve)	103
<b>6.3</b>	FESEM images of <b>(A)</b> Ti <sub>3</sub> C <sub>2</sub> T <sub>x</sub> <b>(B)</b> TiO <sub>2</sub> -Ti <sub>3</sub> C <sub>2</sub> T <sub>x</sub> <b>(C)</b> Ag/TiO <sub>2</sub> -Ti <sub>3</sub> C <sub>2</sub> T <sub>x</sub> <b>(D)</b> Ag/TiO <sub>2</sub> -Ti <sub>3</sub> C <sub>2</sub> T <sub>x</sub> /ITO@MIP before template elution <b>(E)</b> Ag/TiO <sub>2</sub> -Ti <sub>3</sub> C <sub>2</sub> T <sub>x</sub> /ITO@MIP after template elution and <b>(F)</b> EDX spectra of Ag/TiO <sub>2</sub> -Ti <sub>3</sub> C <sub>2</sub> T <sub>x</sub>	104
<b>6.4</b>	<b>(A)</b> CV plots and <b>(C)</b> EIS curves of <b>(a)</b> ITO <b>(b)</b> Ti <sub>3</sub> C <sub>2</sub> T <sub>x</sub> /ITO <b>(c)</b> TiO <sub>2</sub> -Ti <sub>3</sub> C <sub>2</sub> T <sub>x</sub> /ITO and <b>(d)</b> Ag/TiO <sub>2</sub> -Ti <sub>3</sub> C <sub>2</sub> T <sub>x</sub> /ITO <b>(B)</b> CV plots and <b>(D)</b> EIS curves of <b>(a)</b> Ag/TiO <sub>2</sub> -Ti <sub>3</sub> C <sub>2</sub> T <sub>x</sub> /ITO@MIP before elution <b>(b)</b> Ag/TiO <sub>2</sub> -Ti <sub>3</sub> C <sub>2</sub> T <sub>x</sub> /ITO@MIP after elution <b>(c)</b> Ag/TiO <sub>2</sub> -Ti <sub>3</sub> C <sub>2</sub> T <sub>x</sub> /ITO@MIP after rebinding and <b>(d)</b> Ag/TiO <sub>2</sub> -Ti <sub>3</sub> C <sub>2</sub> T <sub>x</sub> /ITO@NIP after elution	106
<b>6.5</b>	<b>(A)</b> CV curves of scan rate studies (10-300 mV/s) <b>(B)</b> linear curves of redox peak potential with log of scan rate and <b>(C)</b> linear curves of peak current vs. square root of scan rate for Ag/TiO <sub>2</sub> -Ti <sub>3</sub> C <sub>2</sub> T <sub>x</sub> /ITO@MIP electrode	107



6.6	Optimization experimental conditions for <b>(A)</b> impact of pH of the electropolymerization solution <b>(B)</b> concentration of LEV: Pyrrole <b>(C)</b> electropolymerization scan cycles <b>(D)</b> scan rate <b>(E)</b> elution time and <b>(F)</b> incubation time	110
6.7	<b>(A)</b> DPV method showing the electrochemical response of Ag/TiO <sub>2</sub> -Ti <sub>3</sub> C <sub>2</sub> T <sub>x</sub> /ITO@MIP electrode against varying concentration of LEV (0.1 fM to 1000 nM) and <b>(B)</b> Linear curve between $\Delta I$ and the logarithm of different LEV concentrations	111
6.8	<b>(A)</b> Selectivity study of Ag/TiO <sub>2</sub> -Ti <sub>3</sub> C <sub>2</sub> T <sub>x</sub> /ITO@MIP sensor towards LEV and other interfering species <b>(B)</b> Reproducibility study of Ag/TiO <sub>2</sub> -Ti <sub>3</sub> C <sub>2</sub> T <sub>x</sub> /ITO@MIP sensor towards LEV using five different electrodes <b>(C)</b> Repeatability of the Ag/TiO <sub>2</sub> -Ti <sub>3</sub> C <sub>2</sub> T <sub>x</sub> /ITO@MIP sensor for ten successive determinations of LEV on same electrode and <b>(D)</b> Stability of Ag/TiO <sub>2</sub> -Ti <sub>3</sub> C <sub>2</sub> T <sub>x</sub> /ITO@MIP sensor over a period of 7 weeks	112



## ABBREVIATIONS

MIP	Molecularly Imprinted Polymer
NIP	Non-Imprinted Polymer
LEV	Levofloxacin
Py	Pyrrole
Ppy	Polypyrrole
Ti <sub>3</sub> AlC <sub>2</sub>	Titanium aluminum carbide
XRD	X-Ray Diffraction
FT-IR	Fourier Transform Infrared Spectroscopy
FESEM	Field Emission Scanning Electron Microscopy
EDX	Energy Dispersive X-ray
CV	Cyclic Voltammetry
DPV	Differential Pulse Voltammetry
EIS	Electrochemical Impedance Spectroscopy
ITO	Indium Tin Oxide
EPD	Electrophoretic Deposition
PBS	Phosphate Buffer Saline
RSD	Relative Standard Deviation
LOD	Limit of Detection
NOR	Norfloxacin
CIP	Ciprofloxacin
OME	Omeprazole
AZY	Azithromycin
AMP	Ampicillin



## Introduction & Literature Review

### 1.1 Introduction to Antibiotics

Antibiotics, named as “wonder drugs,” have caused a remarkable revolution in the medical field over the twentieth century [1]. These are chemical compounds that can inhibit the growth or kill the microorganisms. In both humans and animals, they are widely used to treat and prevent bacterial infections. Penicillin, the first antibiotic in human history, was discovered in 1929 by Sir Alexander Fleming. Since then, numerous other antibiotics have been developed and utilized to safeguard human and animal health [2]. Based on their actions, antibiotics are divided into two categories: (i) Bacteriostatic agents and (ii) Bactericidal agents. Bacteriostatic kills bacteria, whereas bactericidal inhibits their growth. A brief history of different classes of antibiotics is illustrated in Fig. 1.1.

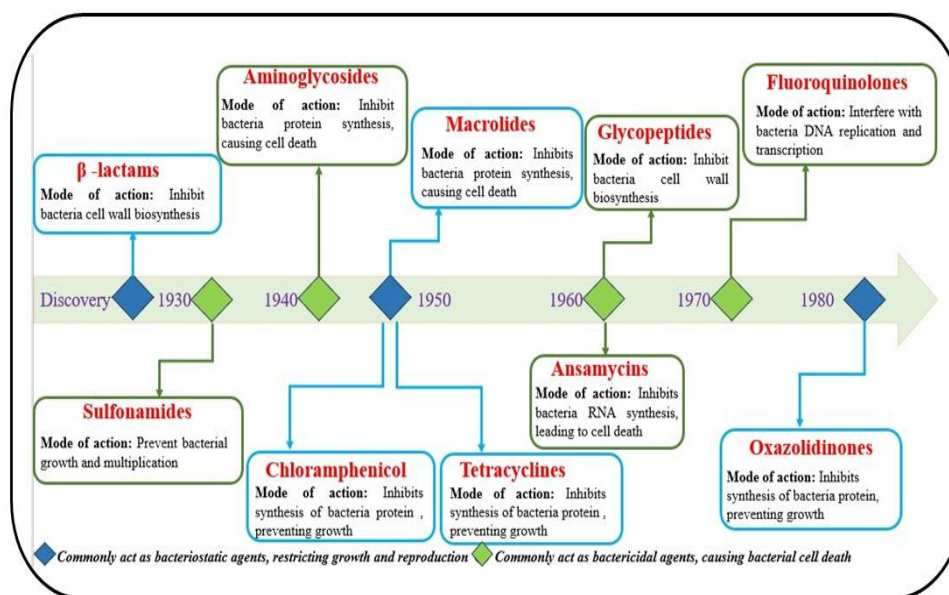


Fig. 1.1 A brief history of antibiotics

## **1.2 Classification of Antibiotics**

Antibiotics' diverse range has given rise to a number of classification schemes, commonly based on their sources, chemical structure, spectrum of activity, and mechanism of action.

### **1.2.1 Based on Sources**

Based on the source, antibiotics can be broadly classified in three categories, namely, natural, semi-synthetic and synthetic.

- **Natural antibiotics:** These antibiotics are being obtained directly from natural sources, including plants, herbs, or microorganisms, and have the ability to damage or eradicate specific bacterial, viral, or fungal diseases [3]. Examples: garlic, turmeric, echinacea, penicillin.
- **Semi-synthetic antibiotics:** These antibiotics retain the original chemical compound from microbes and undergo additional modification to improve stability and reduce toxicity. Examples: aminoglycosides, tetracyclines [4].
- **Synthetic antibiotics:** These antibiotics are obtained through chemical synthesis in the laboratory and utilized to combat dangerous microbes in our surroundings. Examples: ampicillin, sulfonamides [3].

### **1.2.2 Based on the Spectrum of Activity**

An antibiotic's spectrum of activity refers to the variety of microorganisms it can suppress or eradicate. Based on this activity, they are divided into two categories:

1. **Narrow-spectrum antibiotics:** This type of antibiotics act against a certain type of bacterial species (either gram-positive or gram-negative). Examples include fidaxomicin, sarecycline and vancomycin.
2. **Broad-spectrum antibiotics:** This type of antibiotics are effective against both gram-positive and gram-negative microorganisms. Examples include doxycycline, fluoroquinolones and azithromycin [5].

### 1.2.3 Based on Chemical Structure

The effect of antibiotics on a particular species of bacteria is determined by its molecular structure. Antibiotics belonging to the same structural groups usually exhibit similar patterns of efficacy, toxicity and allergic potential side effects [6]. They are classified into various classes based on their chemical structure including  $\beta$ -lactams, fluoroquinolones, macrolides, sulfonamides, glycopeptides, aminoglycosides and tetracyclines, as shown in **Fig. 1.2**.

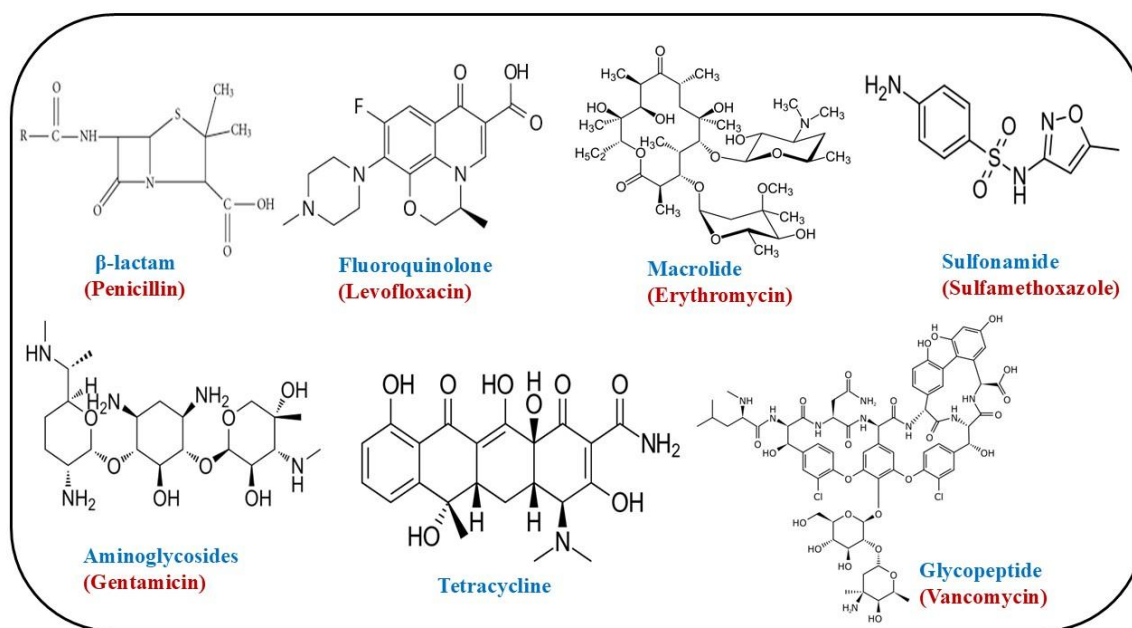


**Fig. 1.2** Chemical structures of different classes of antibiotics

### 1.2.4 Based on the Mechanism of Action

The ability of antibiotics to inhibit bacterial growth by disrupting microorganisms' metabolic activities allows them to be classified by mode of action. The microorganisms need this machinery to survive, maintain, and replicate. As shown in **Fig. 1.3** below, antibiotics are supposed to damage the bacterial cell membranes by one or more modes of action [7, 8].

*Mode 1: Inhibition of the cell wall:* Most bacteria break down or die without the protection of their rigid cell wall. In this mechanism, the antibiotics work by inhibiting the bacterial enzymes (peptidases) that aid in synthesizing the rigid cellular wall.

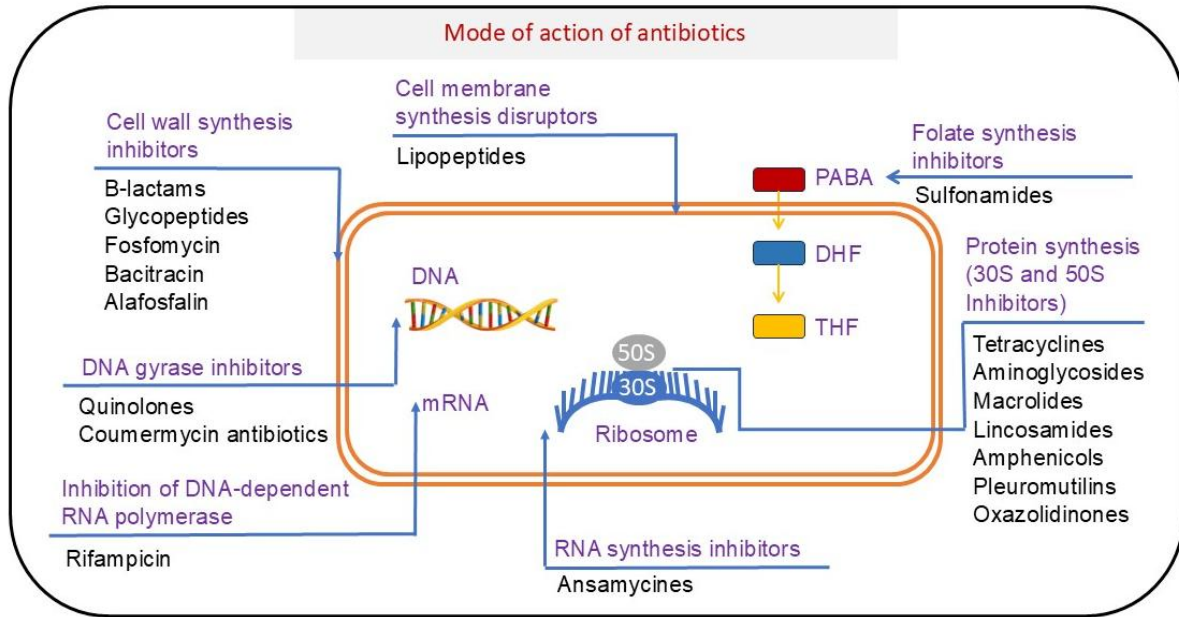


**Fig. 1.3** Mechanism of antibiotics function

*Mode 2: Protein synthesis inhibition:* The primary building block for the synthesizing protein is the ribosome. Here, antibiotics work by attaching to the structural subunits and preventing protein synthesis, which disrupts the ribosomal activity.

*Mode 3: Cell membrane disruptors:* Antibiotics damage the bacterial cell membranes' integrity by interacting with the membrane's lipids, which results in cellular content leakage and death.

*Mode 4: Genetic synthesis interference:* Here, antibiotics block the DNA polymerase enzyme, which facilitates DNA sequence replication and the growth of resistant bacteria. Thus, cell death results from a disturbance in bacterial DNA synthesis.

*Mode 5: Inhibition of RNA synthesis:* In this mode, the messenger RNA transcription suppresses which in turn prevents the synthesis of protein and causes cell death.

*Mode 6: Inhibition of metabolic pathways:* Here, the antibiotic stops the further synthesis of the end product by metabolically inhibiting the enzyme that is responsible for the synthesis of metabolic end product.

### **1.3 Benefits of Antibiotics in Humans and Livestock/Animals**

Antibiotics' discovery or innovation in science is a boon to humans and livestock/animals. When administered carefully, the antibiotics serve as life-saving drugs to safeguard both humans and animals from bacterial infections. In humans, various bacterial infections such as respiratory infections, skin and soft tissue infections, urinary tract infections, pneumonia, sinusitis, sepsis, bronchitis and bone and joint infections [9] are being treated. In animals/livestock, antibiotics are effective in treating gastrointestinal, urogenital and respiratory infections. Their use not only reduces the bacterial infections but also acts as a growth promoter, improving the mass growth rates and efficiency of livestock animals in food production [10].

### **1.4 Impact of Antibiotics on Human Health and Environment**

Antibiotics have emerged as groundbreaking medications in the health industry for the treatment of infections in both humans and livestock. However, due to their structural complexity, most antibiotics are excreted in their original forms which contaminates the soil and natural water resources. In addition, the excessive use of these antibiotics in livestock and aquaculture industries may result in antibiotic residues in foodstuffs such as meat, milk, eggs, honey, chicken and fish which are consumed by humans (**Fig. 1.4**). Antibiotic concentrations typically vary from ng to  $\mu\text{g}$  in environmental samples [11]. However, excessive levels of antibiotic residues may lead to toxic effects on human health such as reproductive disorders, nephropathy, mutagenicity, hepatotoxicity, carcinogenicity and allergic reactions [12]. In addition to these infections, the WHO declared antimicrobial resistance (AMR) a global threat to public health. According to its report, AMR is one of the leading causes of mortality globally with 1.27 million deaths reported directly from AMR in 2019 and contributing to about 5 million deaths globally. According to the studies, AMR may cause more than 8 million deaths annually, more than the total deaths from

diabetes and cancer [13] by 2050. Therefore, an efficient technique is crucial for the quantification, rapid and effective detection of antibiotics.

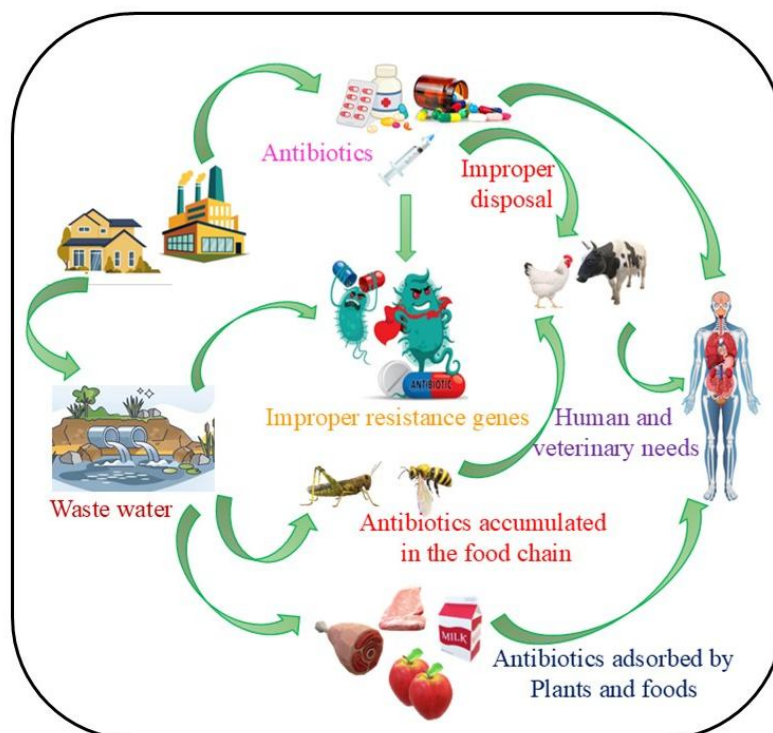


**Fig. 1.4** Schematic illustration of the circulation of antibiotics in the environment

## 1.5 Detection Techniques of Antibiotics

To achieve the benefits of antibiotics while minimizing the health problems arising from their misuse, a highly reliable technique is required to optimally detect them in real samples. Over the past few decades, numerous detection methods have been developed to address this issue.

### 1.5.1 Conventional Detection Methods

The analytical techniques frequently used for quantifying antibiotics include high-performance liquid chromatography (HPLC) [14], flow injection spectrophotometry [15], capillary electrophoresis [16], nuclear magnetic resonance spectroscopy [17], chemiluminescence [18] and enzyme-linked immunosorbent assay (ELISA) [19]. Although these technologies are reliable and susceptible but their applications are restricted due to their high cost, complex sample pre-treatment, time-consuming processes and inability for

on-site detection [20]. Due to these shortcomings, such techniques (**Fig. 1.5**) can be replaced with advanced analytical methods that provide a rapid, straightforward and highly sensitive channel for antibiotic identification.

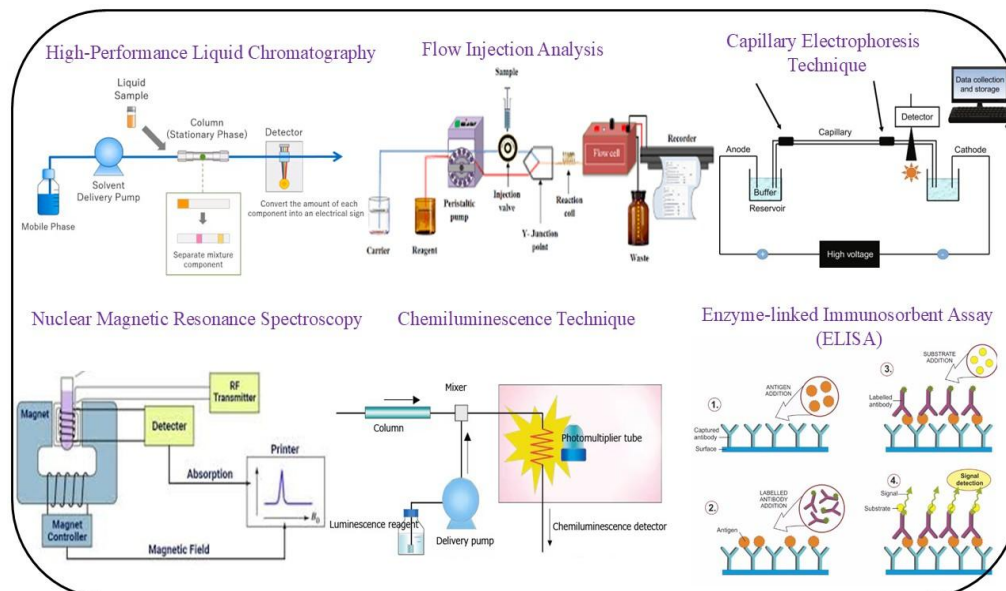


**Fig. 1.5** Conventional techniques for antibiotic detection

### 1.5.2 Sensors: Advanced Detection Tool

Recently, sensors with the advantages of low cost, ease of miniaturisation, rapid response, high portability and sensitivity have gained popularity as an attractive alternative to traditional methods. The term “sensor” originates from a Latin verb “sentire” which means “to perceive”. A sensor is an integrated device that provides precise quantitative or semi-quantitative analytical data by placing a recognition element in direct spatial contact with a transducer [21]. It primarily consists of two major components: a recognition element or receptor for selective target identification and a transducer for signal amplification as shown in **Fig.1.6**. As a recognition element in a sensor (biological receptors such as enzymes, nucleic acids, antibodies or synthetic receptors like molecularly imprinted polymers, nanomaterials etc.), receptors have the ability to bind to analytes with precision, leading to highly specific detection. The transducer is responsible for converting the output received from the interaction of the target analyte with the recognition element into

detectable electrical signals [22]. In other words, it converts one form of energy to another and the process is called signalization.

Depending on the sensing mechanism used, transducers are classified into various categories, including optical, electrochemical, thermal and piezoelectric transducers [23] etc. Among all these, electrochemical transducers are used more frequently for sensing applications due to their rapid responses, simplicity, good sensitivity and high selectivity and reproducibility.

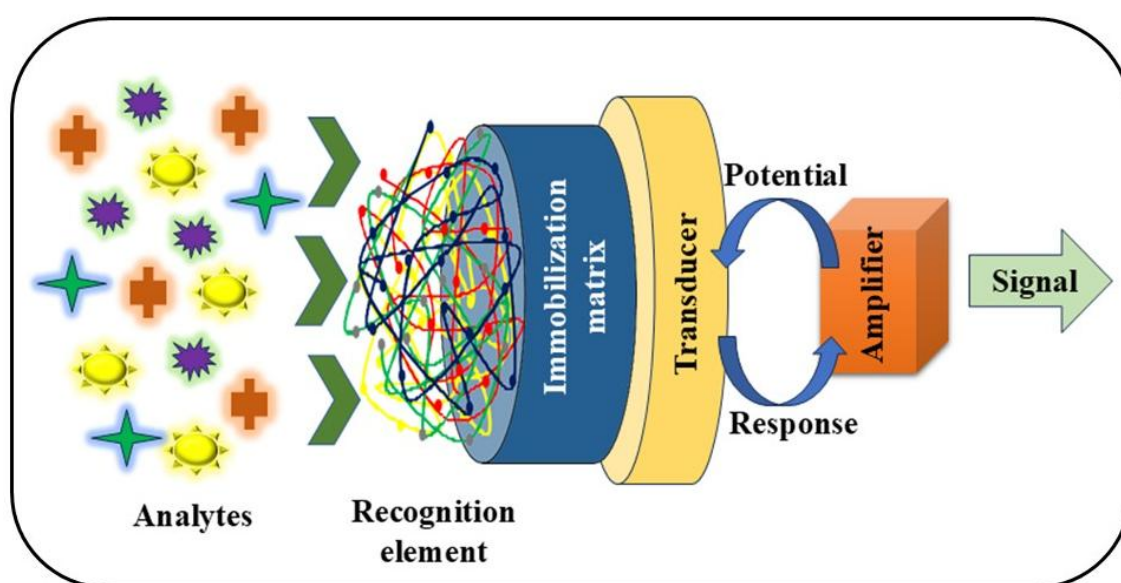


**Fig. 1.6** Schematic representation of a sensor

Electrochemical sensors, a subcategory of chemical sensors, are an integrated tool that transforms the electrochemical reactions into measurable electrical signals. They consist of a three-electrode system, primarily comprising of Ag/AgCl, which serves as a reference electrode, Pt functions as a counter electrode and the fabricated electrode acts as working electrode [24]. The interaction between an analyte and recognition element causes a change in current, potential and impedance which further categorises an electrochemical sensor into four distinct types as given in **Fig. 1.7**.

1. Amperometric sensor: This technique involves measuring the change in current response at a constant potential. A steady voltage is applied to the working electrode, causing a

current to flow in the amperometric sensor, which is recorded as a function of time. They offer sensitive and selective measurements depending on a particular potential for a given analyte. Amperometric sensors have diverse analytical applications in clinical diagnosis, environmental monitoring, neurotransmitter and biomarker detection.

2. Potentiometric sensor: These sensors make a prominent class of electrochemical sensors that assess the potential difference between indicator and reference electrodes resulting from the redox reaction of the analyte with the recognition element. These are employed in ion, gas and pH sensing applications.
3. Conductometric sensor: They measure the electrical conductivity driven by the changes in charge carrier mobility and concentration during the chemical reaction between the two-electrode system in a solution. They are made up of two or more electrodes with an insulating layer between them. The conductivity of the solution around the electrodes changes as a result of the target analyte's interaction with the receptor. The analyte concentration is responsible for the measurement and correlation of this change.
4. Impedance sensor: This sensor is an emerging class of electrochemical technique where impedance is measured by applying a tiny sinusoidal potential to the working electrode of an electrochemical cell, where the resulting current is monitored in the frequency dependence.

The biological or chemical molecular recognition component serves as the sensor's interface, selectively binding to the target analyte. Antibodies, enzymes and nucleic acids are primarily used as recognition elements in sensors; however, their practical applications are hindered by their high cost, limited environmental tolerance and short shelf life [25]. Presently, the research focuses on developing artificial receptors that mimic the sensitivity and selectivity of natural bioreceptors.

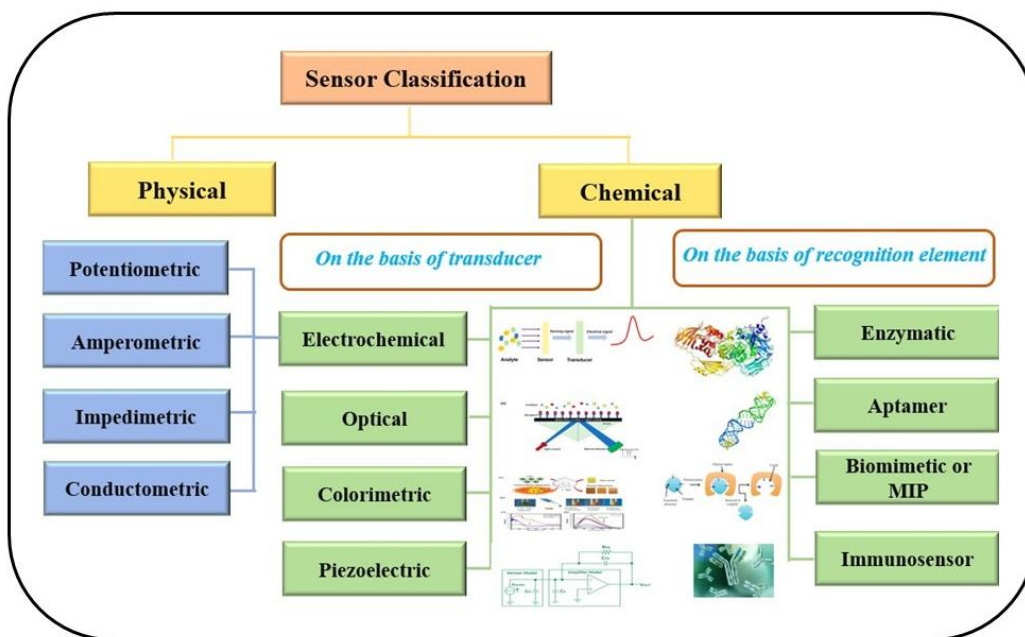
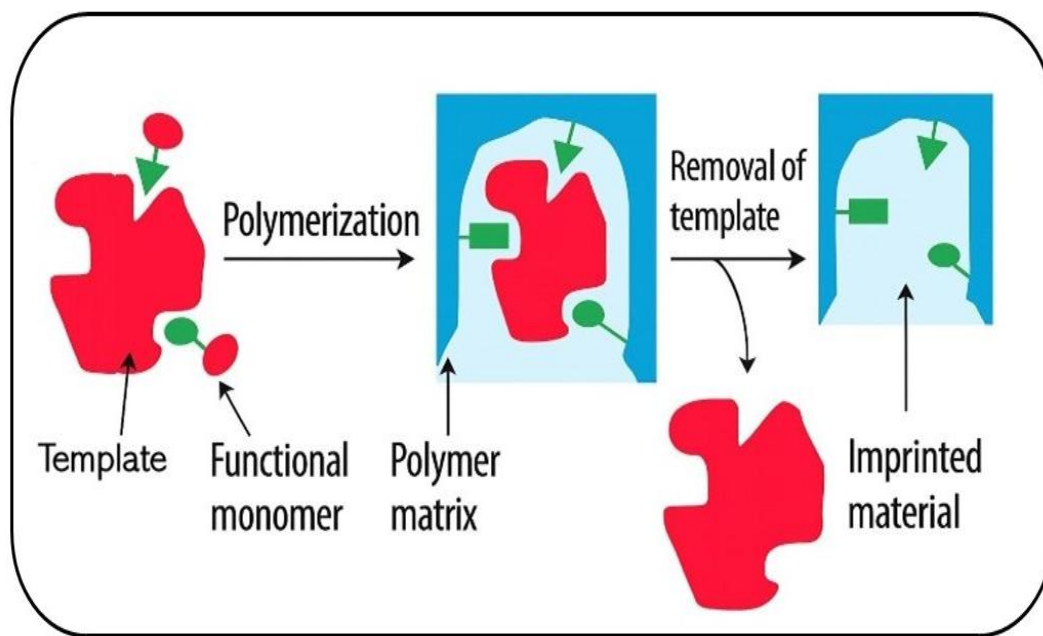


Fig. 1.7 Classification of sensors

## 1.6 Molecularly Imprinted Polymers (MIPs)

The concept of molecularly imprinted polymer (MIP) was initially introduced by Wulff and Mosbach in the 1970s. Wulff developed the covalent approach for imprinting, whereas Mosbach demonstrated the effectiveness of the non-covalent approach, which is now frequently used to synthesize MIP [26]. MIPs are tailor-made synthetic polymer materials that mimic natural bioreceptors by having specific binding sites that serve as recognition sites for the target analyte [27]. These are prepared by mixing the template molecules with the monomers in an inert solvent, resulting in the formation of a pre-polymerisation complex. Afterwards, the template molecules are extracted from the polymeric matrix, leading to the formation of binding cavities that complement the shape, size and chemical functionalities of the target analytes [28]. In this way, molecular memory is created in the polymeric matrix, which acquires the capability to selectively bind the target analyte with high precision (**Fig.1.8**). Due to their long-term stability, predetermined selectivity and tolerance to harsh environmental conditions, they are widely applied in various fields including chromatography, drug delivery, solid-phase extraction and sensor development

[29]. Their combination with electrochemical sensors increases their potential use in biomedical and clinical diagnostics such as biomarkers or pathogen detection and environmental monitoring including the detection of pesticides, heavy metals and pollutants making them valuable tools in a variety of sensing applications.



**Fig. 1.8** A pictorial view of the MIP film

### 1.6.1 Working Principle of MIP Based Electrochemical Sensor

The basic principle of MIP-based electrochemical sensor is to imprint molecular cavities in synthetic materials that selectively recognise and bind the target analyte, transforming these binding events into an electrochemical signal. The fabrication of MIP-based electrochemical sensor involves four consecutive steps:

1. Preparation of template: In this step, the template molecules (target analyte) and selected functional monomer in a solution form a stable pre-polymerization complex. Depending on the chemical functionalities of monomers, the interaction between template molecules and monomers can either result in the formation of covalent bonds or non-covalent bonds including hydrogen bonding, hydrophobic interactions and electrostatic forces.

2. Polymerization: In this step, the functional monomer polymerized around the template molecule to form the rigid polymer matrix. Different polymerization processes have been employed, each with unique characteristics depending on the application and required MIP properties.
3. Elution of template molecules: During this process, the embedded template molecules are removed from the polymeric film which leads to the formation of abundant binding cavities that are complementary in functionality, shape and size of the target analyte.
4. Binding of template molecules: In this step, upon exposure to the template molecules, the imprinted cavities recognize the complementary template molecules thus contributing to MIP selectivity [30].

## **1.6.2 Imprinting Approaches**

Based on the interactions between the functional monomers and the template molecule, three different strategies like covalent, non-covalent and semi-covalent imprinting methods have been established for the molecular imprinting process.

### **1.6.2.1 Covalent Imprinting**

The concept of covalent approach was developed by Wulff and co-workers, in which the functional monomers and template molecules are bonded together through covalent bonds during the polymerization process. After polymerization, the covalent linkage between the monomer and template molecules is chemically cleaved, resulting in imprinted cavities with functional groups that allow the template molecules to bind, re-establishing covalent interactions. High stability of the covalent bond leads to the formation of an even distribution of binding sites within the synthesized polymer. However, the strong covalent interactions between the monomer and template molecules make the rebinding process sluggish, due to which the covalent rebinding process is thought to be less versatile [27, 31].

### **1.6.2.2 Non-Covalent Imprinting**

Mosbach and co-workers have developed the most widely used approach as non-covalent imprinting which involves the non-covalent interactions like hydrogen bonding, electrostatic interactions and van der Waals forces between the template and functional monomers. This is a simple technique that requires a suitable solvent to extract the template molecules leaving behind imprinted cavities tailored to the template molecules. In comparison to covalent imprinting, non-covalent imprinting possesses several advantages, such as consequent breaking of chemical bonds, faster and efficient template removal, lack of polymeric structural collapse and rapid binding-rebinding kinetics which allows a wide range of functional monomers to be employed with a variety of templates [32, 33].

### **1.6.2.3 Semi-Covalent Imprinting**

This technique combines the properties of both covalent imprinting with durability and non-covalent imprinting with quick target uptake. In this approach, the template molecules are covalently bonded to the functional monomers and rebinding involves the non-covalent interactions [34].

## **1.6.3 Polymerization Techniques for MIP Synthesis**

Up to now, MIPs have been prepared using a variety of polymerization techniques including bulk polymerization, precipitation polymerization, sol-gel polymerization and electrochemical polymerization.

### **1.6.3.1 Bulk Polymerization**

This is a simple and traditional method used to produce a monolithic block by mixing all core components (monomers, template, cross-linkers, and initiators) in an aprotic solvent through polymerization. After that, the obtained polymer is crushed and sieved to obtain the particles of the desired size. Despite being simple and cost-effective, this technique

damages the template during the grinding process, yielding particles with irregular forms which results in slow binding kinetics of the template molecules [35, 36].

### **1.6.3.2 Precipitation Polymerization**

This is an efficient method for the preparation of imprinted particles by dissolving monomers, template and cross-linking agents in a solvent that causes the polymer to precipitate as the reaction proceeds. The polymer precipitate does not require grinding in order to form evenly sized particles [37].

### **1.6.3.3 Sol-gel Polymerization**

The sol-gel process is a technique that facilitates the synthesis of MIP in aqueous matrices. In this method, silica-based materials serve as a supporting material, which, when combined with MIPs, provides high thermal stability and porosity, thereby enhancing the sensor's performance. However, slow diffusion kinetics and low sensitivity are some of the demerits of this technique [38, 39].

### **1.6.3.4 Electrochemical Polymerization**

Electrochemical polymerization is a simple, frequently used, and fast procedure in which a conductive polymer layer, typically pyrrole, o-phenylenediamine, aniline or thiophene, is coated onto the fabricated electrode in the presence of desired analyte. These electrochemical layers are formed using a three-electrode system in which the working, reference and auxiliary electrodes are immersed in a solution containing a monomer, template molecules and a supporting electrolyte. All these components are vital to the surface morphology of the imprinted film [40]. After the formation of the MIP layer, the template molecules are removed from the polymeric film, creating binding cavities that resemble the shape, size and functionalities of the target analyte.

### **1.6.4 Challenges in MIP-Based Electrochemical Sensors**

Recently, MIPs have become an essential recognition component in the field of electrochemical sensors due to their facile preparation and cost-effectiveness. The MIP-based electrochemical sensors exhibit several inherent advantages including high sensitivity, selectivity, reusability, robust chemical and mechanical stability and miniaturization which are derived from both MIP films and electrochemical transducers [36]. Despite these benefits, conventional MIPs lack intrinsic conductivity and electrocatalytic activities. Other drawbacks include incomplete binding sites, variable size distribution and limited sensitivity towards target recognition, among others which may restrict the electrochemical signal output [41]. To overcome these limitations and significantly enhance the analytical performance of the MIP-based electrochemical sensor, modifying the MIP electrode with nanomaterials (0D, 1D, 2D and 3D) is a superior route to increase conductivity and boost the overall sensitivity of the sensor.

### **1.7 Two-Dimensional (2D) Materials as Electrode Modifiers**

Two-dimensional materials are crystalline solids with one or more atomic layers that are stacked by van der Waals forces between adjacent layers and are strongly connected by covalent or ionic bonds within the layers [42]. Based on their chemical composition and structural arrangements, these materials are classified as insulators, metals, semiconductors and superconductors. In particular, 2D materials are well-suited for enhancing their physicochemical properties and achieving atomic-level functionalities through surface functionalization, element doping, bandgap engineering and thickness control, all of which are challenging to achieve in bulk materials [43]. Recently, two-dimensional materials like graphene, transition metal dichalcogenide (TMDs) and other 2D materials like graphitic carbon nitride (g-C<sub>3</sub>N<sub>4</sub>), hexagonal boron nitride (h-BN), transition metal oxides (TMOs), layered double hydroxide (LDH), black phosphorous (BP) and MXenes have garnered a

lot of attraction due to their novel properties and wide range of technological applications [44]. **Fig. 1.9** represents the various 2D materials with their structures.

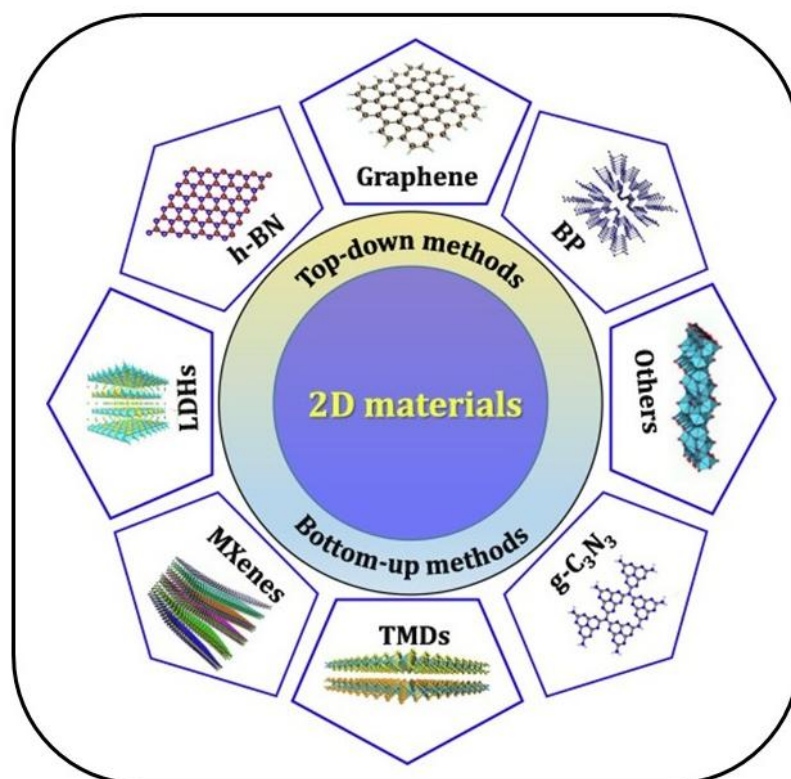


**Fig. 1.9** Diagrammatic illustration of 2D materials along with their structures, Reproduced from ref. [43]. Copyright [2022]

The development of 2D heterostructures is based on their potential application and area of fundamental interest. The formation of a heterojunction by the stacking of two distinct materials together is referred to as a heterostructure. Based on their different functionalities, a variety of heterostructures, including semiconductor-metal, semiconductor-inorganic and semiconductor-carbon, have been described [45]. Recently, numerous heterostructure materials based on their dimensions, such as 2D/0D, 2D/1D, 2D/2D, and 2D/3D, have been fabricated. However, the design and utilization of 2D/2D heterostructures for electrochemical applications have emerged as a fascinating topic. The route chosen to fabricate a 2D heterostructure can determine its size, morphology and crystalline structure,

which in turn alter its physicochemical characteristics, including interfacial interactions, electronic density and electronic band structure [46]. 2D heterostructures have been fabricated by using both in-situ and ex-situ methods. In ex-situ technique, each 2D material component is being prepared individually and then 2D heterostructure composites are being formed using chemical vapour deposition (CVD), liquid-phase exfoliation or epitaxial growth [47]. The ex-situ approach has numerous benefits in terms of cost-effectiveness and scalability. Moreover, obtaining the component ingredient is a time-consuming process that involves complicated synthesis processes and costly instruments. In comparison to ex-situ synthetic approaches, in-situ synthesis strategies enable the synthesis of 2D heterostructures at the nanoscale level with uniform distribution using hydrothermal, solvothermal and sol-gel techniques [48, 49]. **Fig. 1.10** shows the schematic illustration of the synthesis and properties of the 2D heterostructures.

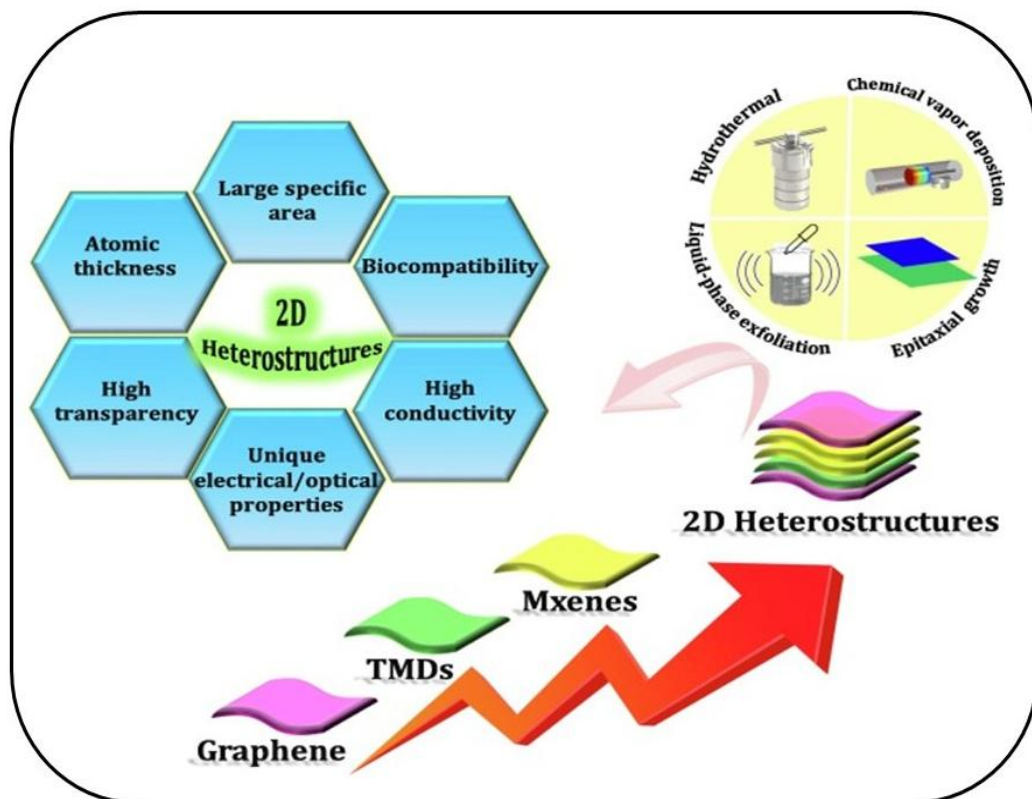


**Fig. 1.10** Schematic representation of the characteristics and synthesis methods of 2D-materials, Reproduced from ref. [43]. Copyright [2022]

The 2D heterostructures exhibit distinct physical and chemical properties like high surface area, desired electrical conductivity and varied chemical compositions making them promising sensing materials that can enhance the performance of the MIPs. Recently, MXene, a novel 2D material has been extensively studied which possesses unique electronic characteristics, a large surface area and numerous active groups (hydroxyl groups, oxygen, and fluorine ions) which make it a suitable candidate for sensing applications [50].

### **1.7.1 MXene**

A new class of 2D materials (MXene) was developed by researchers at Drexel University [51] in 2011. MXene represent the large family of transition metal carbides, nitrides and carbonitrides with the general formula  $M_{n+1}X_nT_x$  where M is early transition metals (Sc, Ti, Zr, V, Nb, Ta, Cr, Mo, etc.), X=carbon and/or nitrogen, n is an integral number between 1 and 3 and T denotes the surface termination groups like -OH, -F, -Cl, -O. In general, the MXene is synthesized by the selective etching of 'A' atomic layer present in MAX phase ( $M_{n+1}AX_n$ ) where A belongs to group 13 and 14 [52]. MAX phase ( $M_{n+1}AX_n$ ) is a closely packed multi-layered structure that consists of alternating M and A layers in which M-A is linked by a metallic bond which can easily be broken in comparison to M-X which links via covalent or ionic bonds. Therefore, by using the proper etching agent, the M-A bond can be broken without disrupting the M-X bond, allowing for the formation of MXene layers [53]. The structural features of MXene are inherited from their corresponding MAX phases which show that the atom X occupies the hexagonal and octahedral sites. Due to the difference in M atom order,  $M_{n+1}X_n$  changes from  $M_2X$  to  $M_3X_2$  and  $M_4X_3$ . Based on structural stability,  $M_2X$  displays hexagonal close packing while both  $M_3X_2$  and  $M_4X_3$  have face-centred cubic packing [54]. Among the various MXene that have been synthesized,  $Ti_3C_2T_x$  is one of the most widely researched MXene due to its good electrical conductivity,

large surface area and ease of functionalization which enables  $Ti_3C_2T_x$  to be used effectively in fields such as sensing, supercapacitors, energy conversion and lithium-ion batteries. **Fig. 1.11** represents the 2D structure of  $Ti_3C_2T_x$ .

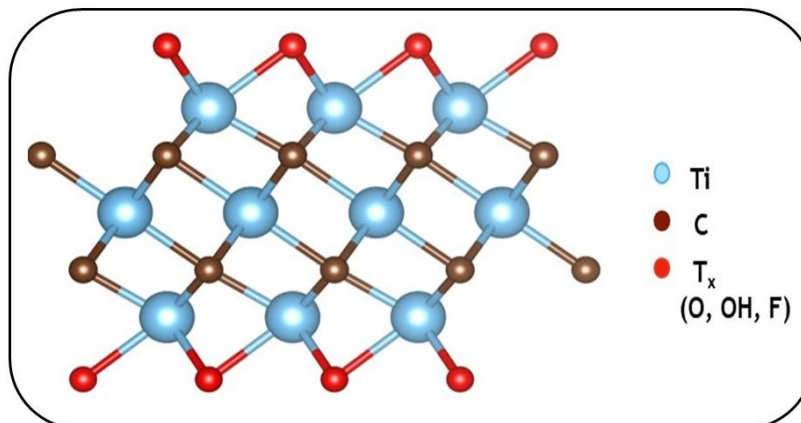


**Fig.1.11** General structure of  $Ti_3C_2T_x$

## 1.7.2 Properties of MXene

MXene's distinctive characteristics include its tunable band gap, high Young's modulus and good thermal and electrical conductivities. Notably, the hydrophilic nature and metallic conductivity of MXene make it different from other 2D materials [55]. Furthermore, the properties of MXene can be tuned by modifying its composition, altering structure/morphology and surface functionalization.

### 1.7.2.1 Mechanical Properties

MXene's mechanical characteristics are based on its surface termination groups. It is anticipated that MXene terminated with the -O group exhibits greater stiffness than MXene terminated with other groups like -F and -OH which shows low elastic stiffness. This may be due to the MXene varying lattice constant with different termination groups. The surface functionalized MXene has large flexibility compared to bare MXene. For example, Guo et al. discovered that  $Ti_2C$  functionalization lowers the Young's modulus but functionalized  $Ti_2C$  is more resilient to strain in comparison to both bare  $Ti_2C$  and even graphene [56].

### **1.7.2.2 Thermal and Electrical Properties**

It is known that both thermal conductivity and thermal oxidation of  $Ti_3AlC_2$  are high. The thermal conductivity of  $Ti_3C_2T_x$  film is found to be approximately 2.84 W/mK.  $Ti_3C_2T_x$  films are extremely flexible with a metallic conductivity of 2400 S/cm making them ideal for wearable electronics-based applications [57]. Moreover, both the annealing temperature and film thickness have a significant impact on the conductivity of sheets.

### **1.7.2.3 Structural Properties**

MXene exhibits high structural and chemical stability due to its remarkable conductivity and abundance of surface functionalities which serve as carriers of intrinsic active and other functional materials for various applications. Until now, various synthetic approaches have been employed to fabricate the porous MXenes with suitable topologies which can be utilized in a wide range of applications including energy storage and conversion due to their porous structure and tunable physicochemical features [58].

### **1.7.2.4 Optical Properties**

The main optical characteristics of  $Ti_3C_2T_x$  are high transparency in the visible region and photothermal effect which make MXenes a promising candidate for flexible transparent electrode applications.  $Ti_3C_2T_x$  showed transmittance up to 91.2% at a thickness of 5 nm and could adsorb light in the UV-vis region (300-500 nm). Moreover, it exhibits a broad absorption band at around 700-800 nm based on the thickness of  $Ti_3C_2T_x$  film which is crucial for photothermal therapy treatment [59].

## **1.8 Synthesis of MXene**

The synthesis techniques employed during the development of MXene significantly influenced their physicochemical characteristics and electrical properties. These techniques are divided into two classes, namely, Top-down method and bottom-up approach [60].

### 1.8.1 Top-Down Methods

In case of top-down method, the ‘A’ layer is selectively etched out from the MAX phase for the synthesis of MXene while maintaining the layered structure. The MAX phases are often obtained by mixing powders of M, A and X elements in a specific proportion and heating at a particular temperature [61]. Currently, a variety of techniques via a top-down approach have been used to synthesise MXene. Hydrofluoric acid (HF) etching, hydrothermal etching, fluorine-free etching, electrochemical etching etc. are some of the commonly used top-down methods for the synthesis of MXene. **Fig.1.12** represents the synthesis of MXene.

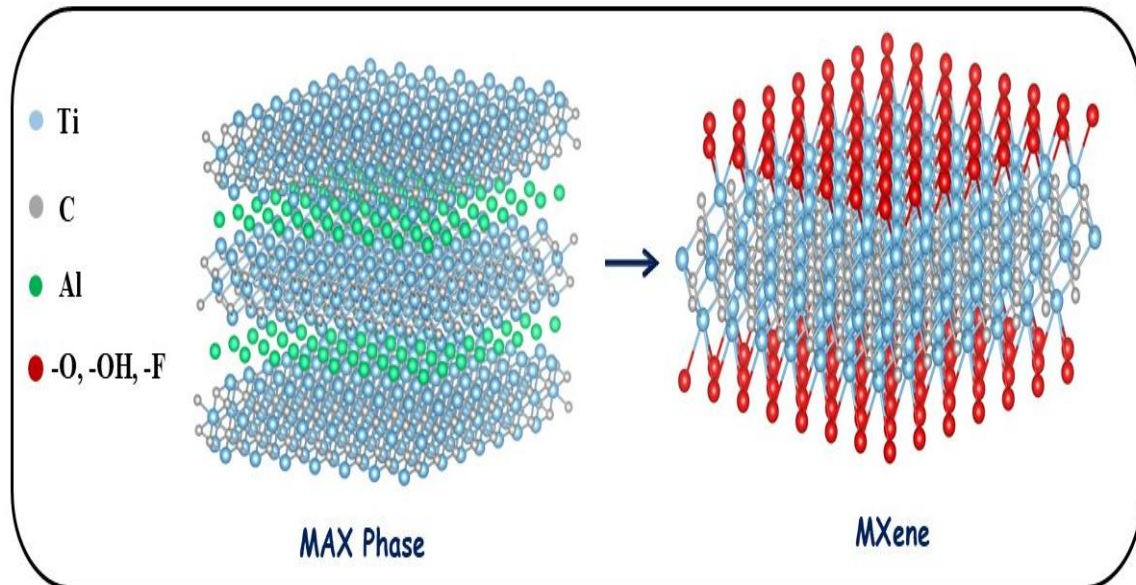
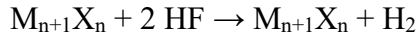


**Fig. 1.12** General synthesis of MXene

#### 1.8.1.1 HF Etching

This is one of the most commonly used methods for the preparation of MXene. To prepare MXene, the MAX phase is directly immersed in aqueous HF solution to selectively etch out the ‘A’ layer and subsequently the surface functionalities (-OH, -O, -F) replace the etched ‘A’ layers which further leads to the formation of multi-layered MXene. Naguib et al. synthesized the  $Ti_3C_2$  by directly using HF as an etching reagent in which they dissolved

the MAX phase ( $\text{Ti}_3\text{AlC}_2$ ) in 50% aqueous HF solution and etched continuously for two hours at room temperature to obtain MXene [62]. The etching approach is described as follows:



In MAX phase, the M-A metal bond is weaker than the M-X bond. Due to their binding energy variation, HF interacts with A-layer components of MAX phase to produce  $\text{H}_2$  and corresponding MXene which is shown by the aforementioned equations [63]. Although for the fabrication of MXene, direct etching of the MAX phase by HF is most commonly used method but the aforementioned approach is hazardous to the environment as well as to humans due to its high toxicity.

### **1.8.1.2 Etching with Fluoride Salt**

Apart from HF, the in situ-generated HF using the mixture of acid (HCl) and fluoride salts (LiF, NaF, KF,  $\text{NaHF}_2$ ,  $\text{NH}_4\text{HF}_2$ , etc) is less aggressive, more economically viable and easier to obtain [64]. For MXene synthesis, the in-situ HF etching method using LiF/HCl is the most widely used approach due to its intercalating characteristics and fast intercalation time. Furthermore, during the etching process, the intercalation of  $\text{Li}^+$ ,  $\text{Na}^+$ ,  $\text{K}^+$  and  $\text{NH}_4^+$  ions increases the interlayer spacing between the MXene sheets which further contributes to MXene's exceptional properties [65]. As a result, this method demonstrated a faster rate of single-step synthesis of MXene in comparison to hazardous HF etching approach and time-consuming multi-step synthesis process.

### **1.8.1.3 Electrochemical Etching**

In the electrochemical process, MXene can be produced by selectively removing the 'A' layers at a particular voltage using the MAX phase as an electrode in an electrolyte such as NaCl, HCl or  $\text{NH}_4\text{Cl}$ . Sun et al. [66] reported an electrochemical etching process using a

low concentration of HCl to synthesize fluoride-free three-layered  $Ti_2C$  sheets from  $Ti_2AlC$ . However, longer etching time led to the removal of Ti layers resulting in the formation of the end product known as carbide-derived carbons (CDC). Pang et al. [67] employed an electrochemical approach to prepare narrow-floral architecture (25 nm)  $Ti_2CT_x$ ,  $Cr_2CT_x$ , and  $V_2CT_x$  MXene sheets. However, the low yield from the electrochemical etching method led to the formation of CDC layers over MXene. Hence, more efficient techniques are needed to eliminate CDC layers and to enable large-scale MXene production.

#### **1.8.1.4 Molten-Salt Etching**

Molten salt etching is one of the effective method to synthesise fluoride-free MXene especially nitride-based MXenes which have higher formation energies compared to carbide-based MXenes [68]. Nitride-based MXenes can be degraded in fluoride-based aqueous solution due to their low cohesive energy and poor structural stability which makes them less effective for etching. These limitations can be overcome by the molten salt etching process which selectively etches the 'A' layer from the MAX phase component by using high-temperature molten salts and does not require HF or other fluoride-based solutions [69]. Urbankowski et al. used the molten-salt etching technique to fabricate titanium nitride MXene. This approach has been widely used to synthesise various nitride and carbide MXenes and by varying the salt composition, etching kinetics and MXene characteristics can be controlled [70]. This technique is an attractive choice for synthesising high-quality, defect-free and environmentally friendly MXene without the need for fluoride-based functionalities.

#### **1.8.1.5 Hydrothermal Etching**

The hydrothermal process is an effective method to isolate HF exposure and etching MXene precursors in a closed environment. Sealing the MAX phase and etchant in a vessel at high pressure and temperature can control the morphologies and crystallinity of the

composites [71]. Guo et al. [72] successfully obtained  $\text{Mo}_2\text{CT}_x$  MXene by hydrothermal etching of  $\text{Mo}_2\text{Ga}_2\text{C}$  at temperatures ranging from 140 to 180°C for 24 h. Peng et al. [73] used a hydrothermal approach to synthesize  $\text{Ti}_3\text{C}_2\text{T}_x$  and  $\text{Nb}_2\text{CT}_x$  by using a mixture of HCl and  $\text{NaBF}_4$  and then compared the results with those of the directly etched HF counterparts. Notably, in contrast to the traditional HF etching process, the strongest peaks of TiC impurities began to appear after more than 20 h etching at temperatures between 140-180°C. This analysis demonstrates the effectiveness of the hydrothermal process for precursors that are difficult to exfoliate.

### 1.8.1.6 Other Advanced Etching Methods

To achieve a safe, effective and eco-friendly production of MXenes, various synthesis routes are being continuously explored. Husmann et al. [74] used an ionic liquid water mixture to etch the Al layer from  $\text{Ti}_3\text{AlC}_2$  and  $\text{Ti}_2\text{AlC}$  thereby synthesising  $\text{Ti}_3\text{C}_2\text{T}_x$  and  $\text{Ti}_3\text{CT}_x$ , without the need of acid. The ionic liquid is intercalated between the MXene sheets while Al is selectively etched by the fluorine-containing ionic liquids through hydrolysis.

Electromagnetic and mechanical waves are also used to etch the 'A' layers from the MAX phase. Mei et al. [75] used ultraviolet light (100 W) in presence of  $\text{H}_3\text{PO}_4$  solution for 3 to 5 h to selectively etch the MAX phase precursor  $\text{Mo}_2\text{Ga}_2\text{C}$  producing mesoporous  $\text{Mo}_2\text{C}$  MXene. This method is highly effective and does not require harmful corrosive acids. Ghazaly et al. [76] utilized surface acoustic waves to achieve ultrafast conversion of  $\text{Ti}_3\text{AlC}_2$  to  $\text{Ti}_3\text{C}_2\text{T}_x$  without requiring an acid supply upon exposure to a low concentration of LiF solution. The A layers were selectively etched by a combination of fluorine ions from LiF and protons generated by surface acoustic waves.

Mei et al. [77] reported the synthesis of  $\text{Ti}_2\text{C}$  sheets from the corresponding sulfur-containing  $\text{Ti}_2\text{SC}$  MAX phase by utilising the thermal reduction method. Layered  $\text{Ti}_2\text{C}$  were produced when weakly bonded sulfur atoms dissociated at high temperature.

However, this process highly depends on the sulfur-containing MAX phase and results in the partial etching of the MAX phase. Additionally, TiO<sub>2</sub> nucleates when the temperature exceeds 700°C, which impacts the MXene yield.

## **1.8.2 Bottom-Up Methods**

MXene produced by top-down methods has been extensively studied, however, it still poses challenges in meeting the needs of various point-of-care devices due to its uneven thickness, thermal instability and small crystal sizes. Furthermore, MXene has various functional groups such as –O, –Cl and –OH which have limited electrochemical applications due to their poor electrical characteristics and flawed structures [78]. To address this issue, bottom-up methods provide a novel approach to creating high-quality and thermally stable MXenes.

### **1.8.2.1 Chemical Vapour Deposition (CVD)**

CVD is an advanced technique used to fabricate a novel two-dimensional material - MXenes. In this method, a thin film is generated by adding volatile precursors into a reaction chamber where they react or break down with a hot substrate. CVD precisely control the film thickness and composition which is essential for improving the MXenes properties for certain applications. Xu et al. [79] employed the CVD approach to fabricate a high-quality ultrathin 2D Mo<sub>2</sub>C with a large surface area. The remarkable chemical and thermal stability of ultrathin Mo<sub>2</sub>C displayed strong anisotropy in the magnetic field direction and two-dimensional features of the superconducting transitions.

### **1.8.2.2 Pulsed Laser Deposition (PLD)**

PLD is an efficient and advanced technique for producing MXene. In this method, a target is subjected to a high-power pulsed laser to generate a fine layer. This method provides precise control over the film's thickness, composition and microstructure by modifying several parameters, including laser fluency, pulse duration and deposition environment [68].

## **1.9 Application of MXenes and MXene-Based Composites for Antibiotic Detection**

The literature review reveals that MXene and its composites have been utilized as a sensing platform for detecting antibiotics. Zhou et al. [80] developed an MIP-based electrochemical sensor using MXene-modified glassy carbon electrode (GCE) for the detection of chloramphenicol. An efficient screen-printed carbon electrode (SPCE) modified with MXene and graphene has been developed by Essousi et al. [81] for the selective detection of oxytetracycline. Further, Yang et al. [82] constructed an electrochemical sensing platform for ofloxacin detection using gold nanoparticles and MXene composite. A novel MIP electrochemical sensor has been designed by Zhang et al. [83] for the sensitive detection of chlortetracycline using MXene and gold-platinum ruthenium nanocomposite. The ternary composite AuNPs/AgNWs/Ti<sub>3</sub>C<sub>2</sub>T<sub>x</sub> was further used by Wang et al. [84] to fabricate an MIP electrochemical sensor for the detection of sulfathiazole. An amperometric sensor was developed by Vilian et al. [85] for the detection of nitrofurantoin using a gold nanoparticle-decorated polypyrrole-MXene composite. Kabir et al. [86] proposed an electrochemical sensor based on SiO<sub>2</sub>-MXene-SnO<sub>2</sub> nanocomposite for the sensitive and selective detection of ciprofloxacin. Shen et. al [87] fabricated a hydrophobic carbon paper modified with CoFe/MXene as a sensing platform for the ultrasensitive detection of chloramphenicol. Furthermore, a self-assembled sensing interface based on an aptamer functionalized MXene was reported by Xiong et al. [88] for the detection of kanamycin and tetracycline. A novel MIP-based ratiometric electrochemical sensor was constructed by Qi et al. [89] using Fe-MOF-NH<sub>2</sub>/CNT-NH<sub>2</sub>/MXene composite for the detection of ofloxacin. Dong et al. [90] developed an ultrasensitive aptasensor for detecting chloramphenicol using a liquid-exfoliated graphene/MXene composite. Furthermore, Zhang et al. [91] fabricated a Co, N-Ti<sub>3</sub>C<sub>2</sub>T<sub>x</sub>/C/PEDOT-based MIP electrochemical sensor for the ultrasensitive

detection of gatifloxacin. Additionally, **Table 1.1** summarizes the recent advancements in the analytical performance of electrochemical sensors for detecting various antibiotics.

**Table 1.1:** Recent advances in electrochemical sensors for antibiotic detection

Electrode material	Analyte	Method	Sample	Linear range	LOD	Ref
CuZnS@MXene	CAP	Amperometry	Milk, honey, human urine, eye drop	0.002-100 $\mu\text{M}$	0.15 nM	[92]
		DPV		0.002-6.75 $\mu\text{M}$	0.18 nM	
VS <sub>2</sub> /Ti <sub>3</sub> C <sub>2</sub> T <sub>x</sub>	NFT	LSV	Tap water, lake water, milk, honey	0.01-400 $\mu\text{M}$	4.7 nM	[93]
AgNPs-rGO	CIP	DPV	River water, Tap water	0.15-13 $\mu\text{M}$	6.25 nM	[94]
WO <sub>3</sub> /rGO	TC	DPV	Milk, lake water, Fish, and tap water	0.1-400 $\mu\text{M}$	202 nM	[95]
MIP-MoS <sub>2</sub> @CNTs	TMP	DPV	Lake water, Tap water, Fish from lake water, Fish from river water	50-3000 nM	27.0 nM	[96]
V <sub>3</sub> Se <sub>4</sub> / $\beta$ -CDN/rGONs	MFH	DPV	Human blood, wastewater, river water	0.02-873.39 $\mu\text{M}$	0.015 $\mu\text{M}$	[97]
Fe-MOF@GDY	CAP	DPV	Lake water	1 pM-24 mM	0.54 pM	[98]
N-HCS@PEDOT-PMAA/MIP	NOR	DPV	Lake water, honey, milk	0.5 nM-33 $\mu\text{M}$	0.061 nM	[99]
CeV/CN	LV	DPV	Human blood serum	0.025-276.35 $\mu\text{M}$	6.60 nM	[100]

Fe <sub>3</sub> O <sub>4</sub> - MoS <sub>2</sub> @MXene	LEV	DPV	Waste water	6-17 μM	900 nM	[101]
MoS <sub>2</sub> @MWCN T	Ofloxacin	DPNV LSV	Distilled water, Tap water, Rain water	0.29-0.82 μM 0.24-0.82 μM	0.12 μM 0.17 μM	[102]
UiO-66- NH <sub>2</sub> /CNTs	OFL	CV	Prescription drugs	0.1 nM-20 μM	0.03 nM	[103]

### 1.10 Objective

The main aim of this research study is to develop an electrochemical sensor utilizing a new class of 2D materials, i.e., MXene and its hybrids with metals, metal oxides and metal sulphides for the detection of an antibiotic, specifically levofloxacin. The fabrication of an electrochemical sensor has been accomplished by the following stages:

- Synthesis and modification of MXene by a less hazardous method as well as investigating the parameters that affect the electrochemical performance.
- Characterization of synthesized materials by structural and morphological techniques.
- Fabrication of a transducer matrix by electrophoretic deposition of material on an ITO-coated glass electrode.
- Fabrication of MIP layer on the modified electrode via electropolymerization followed by elution of template molecules using a suitable solvent.
- Electrochemical response studies of the fabricated electrode using different electrochemical techniques for antibiotic detection.
- Reproducibility, selectivity and stability studies of the sensors.
- Validation of the results using spiked real samples with the fabricated sensor.

## **1.11 Thesis Organization**

This thesis focuses on the synthesis, characterization and application of  $Ti_3C_2T_x$  and its hybrid with Ag,  $TiO_2$  and CuS in order to create an efficient electrochemical sensor for the targeted detection of antibiotic (Levofloxacin). **The entire research work of the thesis comprised of seven chapters which are organised as given below:**

**Chapter 1** presents an overview of antibiotics, their classification, harmful consequences on human health and environment and various techniques available for their detection. Furthermore, the concept of molecularly imprinted polymers (MIP) and their role in electrochemical sensing have been discussed. Additionally, an attempt has been made to provide a descriptive literature review of MXene properties and various synthesis methods.

**Chapter 2** outlines the details of various experimental techniques including FTIR spectroscopy, Raman spectroscopy, X-ray diffraction (XRD), Field emission scanning electron microscopy (FE-SEM) and Energy dispersive X-ray spectroscopy (EDX) that have been used to characterise the  $Ti_3C_2T_x$  and  $Ti_3C_2T_x$ -based nanocomposite-modified electrodes. Electrochemical methods such as cyclic voltammetry (CV) and electrochemical impedance spectroscopy (EIS) are being used to characterize the  $Ti_3C_2T_x$  and its nanocomposite-based electrodes. The electrochemical response of various nanohybrid sensors to antibiotic (LEV) concentration has been studied by using the DPV approach. Attempts have also been made to describe the procedures and protocols used to determine various parameters related to the performance of  $Ti_3C_2T_x$  composite-based sensor for antibiotic detection.

**Chapter 3** describes the results of studies focused on developing a sensitive and efficient molecularly imprinted-based electrochemical sensor for levofloxacin (LEV) detection using  $Ti_3C_2T_x$ . The hydrothermally synthesised  $Ti_3C_2T_x$  proved to be an efficient material for fabricating a sensor platform in sensing studies due to its high metal-like conductivity

and hydrophilic nature. For the MIP sensor construction, initially the synthesised  $\text{Ti}_3\text{C}_2\text{T}_x$  was electrophoretically deposited on the indium tin oxide (ITO) coated glass substrate followed by the electropolymerization of pyrrole as a monomer and LEV as template molecules to create MIP layer for the selective determination of LEV. Successful synthesis was confirmed by using various spectroscopic, microscopic and electrochemical techniques. The electrochemical response of the fabricated sensor ( $\text{Ti}_3\text{C}_2\text{T}_x/\text{ITO}@\text{MIP}$ ) shows a high sensitivity ( $40.20 \mu\text{A} (\text{pM})^{-1}\text{cm}^{-2}$ ) with a broad linear range of 1 pM-100 nM, and a low detection limit (0.76 pM). The selectivity study suggests that the fabricated sensor efficiently detects the LEV. Additionally, the fabricated sensor exhibits good stability and reproducibility in detecting the LEV in tap water and soil with an excellent recovery rate.

The fabrication of a highly selective and sensitive molecularly imprinted electrochemical sensor utilising  $\text{TiO}_2\text{-Ti}_3\text{C}_2\text{T}_x$  nanohybrid as a sensing platform is reported in **Chapter 4**. The in-situ development of 2D- $\text{TiO}_2$  on the  $\text{Ti}_3\text{C}_2\text{T}_x$  sheets enhances surface area and improves electrochemical performance compared to  $\text{Ti}_3\text{C}_2\text{T}_x$ . Various spectroscopic and morphological techniques have been used to validate the formation of  $\text{TiO}_2\text{-Ti}_3\text{C}_2\text{T}_x$  nanohybrid. Electrochemical results confirm that the fabricated sensor ( $\text{TiO}_2\text{-Ti}_3\text{C}_2\text{T}_x/\text{ITO}@\text{MIP}$ ) showed high sensitivity, broad linear range (1 pM-100 nM) and low LOD (0.41 pM). Moreover, the developed sensor exhibits acceptable stability, good reproducibility and excellent selectivity towards LEV detection. Consequently, the  $\text{TiO}_2\text{-Ti}_3\text{C}_2\text{T}_x/\text{ITO}@\text{MIP}$  sensor proves to be a viable platform for LEV detection in biological and environmental samples (urine, human serum, river water, and soil), with good recovery rates.

**Chapter 5** reveals the development of a CuS-anchored 2D  $\text{Ti}_3\text{C}_2\text{T}_x$  nanohybrid-based MIP impedimetric sensor. The synthesized  $\text{CuS}/\text{Ti}_3\text{C}_2\text{T}_x$  has been characterized using a series of structural, elemental, and morphological analysis. Furthermore, the MIP-based

impedimetric sensor has been fabricated using the electropolymerization technique on a CuS/Ti<sub>3</sub>C<sub>2</sub>T<sub>x</sub> modified electrode followed by an elution process. Electrochemical investigations indicate that the CuS/Ti<sub>3</sub>C<sub>2</sub>T<sub>x</sub>-modified MIP sensor (CuS/Ti<sub>3</sub>C<sub>2</sub>T<sub>x</sub>@MIP) offers a relatively large surface area and a better electron transfer coefficient compared to MIP/Ti<sub>3</sub>C<sub>2</sub>T<sub>x</sub>. The sensing response of the electrode exhibits linearity over a concentration range of 0.01 pM to 1000 nM, with a detection limit of 10 fM. Moreover, the sensor was successfully validated in river water and milk and it was found to be highly stable and selective for the detection of LEV.

In **Chapter 6**, the results pertaining to the development of an electrochemical sensor based on Ag/TiO<sub>2</sub>-Ti<sub>3</sub>C<sub>2</sub>T<sub>x</sub> hybrid have been reported. Various spectroscopic and morphological techniques have been used to validate the formation of Ag/TiO<sub>2</sub>-Ti<sub>3</sub>C<sub>2</sub>T<sub>x</sub>. Furthermore, a novel electrochemical sensing platform has been fabricated by electrophoretic deposition of the synthesised material on the ITO surface, followed by an electropolymerization process for the selective recognition of LEV. The excellent conducting and catalytic properties of Ag/TiO<sub>2</sub>-Ti<sub>3</sub>C<sub>2</sub>T<sub>x</sub> facilitate the superior electroanalytical capabilities of the fabricated electrodes. As a result, the developed sensor exhibits stable, rapid and high sensing performance with linearity in the concentration range of 0.1 fM to 1000 nM (LOD = 0.1 fM). The performance of the sensor was validated with river water, soil and milk samples. The sensor shows an excellent recovery rate of nearly 93.4-105.2% which justifies the efficacy of the fabricated electrodes for LEV detection.

**Chapter 7** briefly summarises the studies related to the applications of MXene-based 2D materials for antibiotic detection. Furthermore, this chapter also highlights the futuristic potential and possibilities of MXene-based composites for sensing in other systems.

**References**

1. S. Dawadi, R. Thapa, B. Modi, S. Bhandari, A.P. Timilsina, R.P. Yadav, B. Aryal, S. Gautam, P. Sharma, B.B. Thapa, N. Aryal, S. Aryal, B.P. Regmi, and R. Parajuli, Technological advancements for the detection of antibiotics in food products, *Processes*, 9 (2021) 1500.
2. C. Liu, B.Li, M. Liu, and S. Mao, Demand, status, and prospect of antibiotics detection in the environment, *Sensors and Actuators B: Chemical*, 369 (2022) 132383.
3. A. Kalyani, M. Mahalakshmi, N. Ahlaya, P. Anusha, S.D. Seema, and T. Maneesha, Classification Of Different Antibiotics And Their Adverse Effects And Uses From Origin To Present, *International Journal of Pharmaceutical Sciences*, 2 (2024) 98-121.
4. M.F. Haddad, B.A. Abdullah, H.A. AlObeidi, and M.F. Haddad, Antibiotic classification, mechanisms, and indications: A review, *International Journal of Medical and All Body Health Research*, 5 (2024) 39-46.
5. A. Grada and C.G. Bunick, Spectrum of antibiotic activity and its relevance to the microbiome, *JAMA Network Open*, 4 (2021) e215357-e215357.
6. E. Etebu and I. Arikekpar, Antibiotics: Classification and mechanisms of action with emphasis on molecular perspectives, *International Journal of Applied Microbiology and Biotechnology Research*, 4 (2016) 90-101.
7. I. Sanseverino, A. Navarro Cuenca, R. Loos, D. Marinov, and T. Lettieri, State of the Art on the Contribution of Water to Antimicrobial Resistance. Publications Office of the European Union (2018).
8. A.L. Fymat, Antibiotics and antibiotic resistance, *Biomedical Journal of Scientific and Technical Research*, 1 (2017) 1-16.
9. M. Jiang, F. Taghizadeh, and P.S. Steyger, Potential mechanisms underlying inflammation-enhanced aminoglycoside-induced cochleotoxicity, *Frontiers in Cellular Nanoscience*, 11 (2017) 362.
10. R.K. Sajwan, S.Z.H Hashmi, J.K. Himanshu, A. Kumari, and P.R. Solanki, Current advancement in nanomaterial-based emerging techniques for the determination of aminoglycosides antibiotics for antibiotic resistance surveillances, *Materials Advances*, 5 (2024) 961-985.
11. A. Joshi, K.-H. Kim, Recent advances in nanomaterial-based electrochemical detection of antibiotics: Challenges and future perspectives, *Biosensors and Bioelectronics*, 153 (2020) 112046.
12. M. Majdinasab, R.K. Mishra, X.Tang, and J.L. Marthy, Detection of antibiotics in food: New achievements in the development of biosensors, *TrAC Trends in Analytical Chemistry*, 127 (2020) 115883.
13. C.J.L. Murray, et al., Global burden of bacterial antimicrobial resistance in 2019: a systematic analysis, *The Lancet*, 399 (2022) 629-655.
14. M.R. Payán, M.Á.B. López, R. Fernández-Torres, J.A.O. González, and M.C. Mochón,, Hollow fiber-based liquid phase microextraction (HF-LPME) as a new approach for the HPLC determination of fluoroquinolones in biological and

- environmental matrices, *Journal of Pharmaceutical and Biomedical Analysis*, 55 (2011) 332-341.
15. I.J.Al-Momani, Flow injection spectrophotometric determination of the antibacterial levofloxacin in tablets and human urine, *Analytical letters*, 39 (2006) 741-750.
  16. Y.M. Liu, J.T. Cao, W. Tian, and Y.L. Zheng, Determination of levofloxacin and norfloxacin by capillary electrophoresis with electrochemiluminescence detection and applications in human urine, *Electrophoresis*, 29 (2008) 3207-3212.
  17. A. Salem, H. Mossa, and B.N. Barsoum, Quantitative determinations of levofloxacin and rifampicin in pharmaceutical and urine samples using nuclear magnetic resonance spectroscopy, *Spectrochimica Acta Part A: Molecular and Biomolecular Spectroscopy*, 62 (2005) 466-472.
  18. X. Shao, Y. Li, Y. Liu, and Z. Song, Rapid determination of levofloxacin in pharmaceuticals and biological fluids using a new chemiluminescence system, *Journal of Analytical Chemistry*, 66 (2011) 102-107.
  19. A.-C. Huet, C. Charlier, S.A. Tittlemier, G. Singh, S. Benrejeb, and P. Delahaut, Simultaneous determination of (fluoro) quinolone antibiotics in kidney, marine products, eggs, and muscle by enzyme-linked immunosorbent assay (ELISA), *Journal of Agricultural and Food Chemistry*, 54 (2006) 2822-2827.
  20. D.M. de Farias, L.V. de Faria, T.P. Lisboa, M.A.C. Matos, R.A.A. Muñoz, and R.C. Matos, Determination of levofloxacin in pharmaceutical formulations and urine at reduced graphene oxide and carbon nanotube-modified electrodes, *Journal of Solid State Electrochemistry*, 24 (2020) 1165-1173.
  21. Z. Xu, X. Chen, and S. Dong, Electrochemical biosensors based on advanced bioimmobilization matrices, *TrAC Trends in Analytical Chemistry*, 25 (2006) 899-908.
  22. C. Zhou, H. Zou, C. Sun, and Y. Li, Recent advances in biosensors for antibiotic detection: Selectivity and signal amplification with nanomaterials, *Food Chemistry* 361 (2021) 130109.
  23. S.G. Priya, Biosensor classification and principle operation, in *Biosensors: Developments, Challenges and Perspectives*, Springer (2024) 1-12.
  24. H.A. Saputra, Electrochemical sensors: basic principles, engineering, and state of the art, *Monatshefte für Chemie-Chemical Monthly*, 154 (2023) 1083-1100.
  25. S. Han, R. Sun, L. Zhao, C. Yan, and H. Chu, Molecularly imprinted electrochemical sensor based on synergistic interaction of honeycomb-like Ni-MOF decorated with AgNPs and N-GQDs for ultra-sensitive detection of olaquinox in animal-origin food, *Food Chemistry*, 418 (2023) 136001.
  26. N. Shah, M. Ul-Islam, M. Haneef, and J.K. Park, A brief overview of molecularly imprinted polymers: from basics to applications, *Journal of Pharmacy Research*, 5 (2012) e3317.
  27. L. Chen, X. Wang, W. Lu, X. Wu, and J. Li, Molecular imprinting: perspectives and applications, *Chemical Society Reviews*, 45 (2016) 2137-2211.

28. H. Lu, M. Liu, H. Cui, Y. Huang, L. Li, and Y. Ding, An advanced molecularly imprinted electrochemical sensor based bifunctional monomers for highly sensitive detection of nitrofurazone, *Electrochimica Acta*, 427 (2022) 140858.
29. P. Rebelo, E. Costa-Rama, I. Seguro, J.G. Pacheco, H.P.A. Nouws, M.N.D.S. Cordeiro, and C.D-Matos, Molecularly imprinted polymer-based electrochemical sensors for environmental analysis, *Biosensors and Bioelectronics*, 172 (2021) 112719.
30. V. Ayerdurai, M. Cieplak, and W. Kutner, Molecularly imprinted polymer-based electrochemical sensors for food contaminants determination, *TrAC Trends in Analytical Chemistry*, 158 (2023) 116830.
31. S. Ansari and M. Karimi, Recent progress, challenges and trends in trace determination of drug analysis using molecularly imprinted solid-phase microextraction technology, *Talanta*, 164 (2017) 612-625.
32. N. Tarannum, S. Khatoon, and B.B. Dzantiev, Perspective and application of molecular imprinting approach for antibiotic detection in food and environmental samples: A critical review, *Food Control*, 118 (2020) 107381.
33. M.R. Gama, and C.B.G. Bottoli, Molecularly imprinted polymers for bioanalytical sample preparation, *Journal of Chromatography B*, 1043 (2017) 107-121.
34. H. Dong, L. Tong, M. Cheng, and S. Hou, Utilizing electrospun molecularly imprinted membranes for food industry: Opportunities and challenges, *Food Chemistry*, 460 (2024) 140695.
35. J.J. BelBruno, Molecularly imprinted polymers, *Chemical Reviews*, 119 (2018) 94-119.
36. L.S.K. Rokhmat, S. Zuliska, Y.S. Ridwan, R.P. Fauzia, P.R. Ramdani, and Y.M. Hartati, Molecularly Imprinted Polymer Technology for Electrochemical Detection of Diabetes-Related Biomarkers, *Sensors and Actuators Reports*, (2025) 100353.
37. S. Pardeshi, and S.K. Singh, Precipitation polymerization: a versatile tool for preparing molecularly imprinted polymer beads for chromatography applications, *RSC Advances*, 6 (2016) 23525-23536.
38. M.M. Moein, A. Abdel-Rehim, and M. Abdel-Rehim, Recent applications of molecularly imprinted sol-gel methodology in sample preparation, *Molecules*, 24 (2019) 2889.
39. T. Zhou, L. Ding, G. Che, W. Jiang, and L. Sang, Recent advances and trends of molecularly imprinted polymers for specific recognition in aqueous matrix: Preparation and application in sample pretreatment, *TrAC Trends in Analytical Chemistry*, 114 (2019) 11-28.
40. R.D. Crapnell, A. Hudson, C.W. Foster, K. Eersels, B. Grinsven, T.J. Cleij, C.E. Banks, and M. Peeters, Recent advances in electrosynthesized molecularly imprinted polymer sensing platforms for bioanalyte detection, *Sensors*, 19 (2019) 1204.
41. A.A. Lahcen and A. Amine, Recent advances in electrochemical sensors based on molecularly imprinted polymers and nanomaterials, *Electroanalysis*, 31 (2019) 188-201

42. M. Velický and P.S. Toth, From two-dimensional materials to their heterostructures: An electrochemist's perspective, *Applied Materials Today*, 8 (2017) 68-103.
43. R. Sakthivel, M. Keerthi, R.-J. Chung, and J.-H. He, Heterostructures of 2D materials and their applications in biosensing, *Progress in Materials Science*, 132 (2023) 101024.
44. A.Di Bartolomeo, Emerging 2D materials and their van der Waals heterostructures, *Nanomaterials*, (2020) 579.
45. X. Guan, X. Yu, D Periyanaounder, M.R. Benzigar, J.K. Huang, C.H. Lin, J. Kim, S. Singh, L. Hu, D. Li, and J.-H. He, Recent progress in short-to long-wave infrared photodetection using 2D materials and heterostructures, *Advanced Optical Materials*, 9 (2021) 2001708.
46. A.K. Geim and I.V. Grigorieva, Van der Waals heterostructures, *Nature*, 499 (2013) 419-425.
47. A. Yan, J. Velasco Jr, S. Kahn, K. Watanabe, T. Taniguchi, F. Wang, M.F. Crommie, A. Zettl, Direct growth of single-and few-layer MoS<sub>2</sub> on h-BN with preferred relative rotation angles, *Nano Letters*, 15 (2015) 6324-6331.
48. W. Li, F. Wang, S. Feng, J. Wang, Z. Sun, B. Li, Y. Li, J. Yang, A.A. Elzatahry, Y. Xia, and D. Zhao, Sol-gel design strategy for ultradispersed TiO<sub>2</sub> nanoparticles on graphene for high-performance lithium ion batteries, *Journal of the American Chemical Society*, 135 (2013) 18300-18303.
49. K. Xie, K. Yuan, X. Li, W. Lu, C. Shen, C. Liang, R. Vajtai, P. Ajayan, and B. Wei, Superior potassium ion storage via vertical MoS<sub>2</sub> “nano-rose” with expanded interlayers on graphene, *Small*, 13 (2017) 1701471.
50. H. Zhang, Z. Wang, F. Wang, Y. Zhang, H. Wang, and Y. Liu, Ti<sub>3</sub>C<sub>2</sub> MXene mediated Prussian blue in situ hybridization and electrochemical signal amplification for the detection of exosomes, *Talanta*, 224 (2021) 121879.
51. M. Naguib, M. Kurtoglu, V. Presser, J. Lu, J. Niu, M. Heon, L. Hultman, Y. Gogotsi, and M.W. Barsoum, Two-dimensional nanocrystals produced by exfoliation of Ti<sub>3</sub>AlC<sub>2</sub>, MXenes, (2023) 15-29.
52. M. Naguib and Y. Gogotsi, Synthesis of two-dimensional materials by selective extraction, *Accounts of Chemical Research*, 48 (2015) 128-135.
53. P.K. Kalambate, N.S. Gadhari, X.Li, Z.Rao, S.T. Navale, Y. Shenet, V.R. Patil, and Y. Huang, Recent advances in MXene-based electrochemical sensors and biosensors, *TrAC Trends in Analytical Chemistry*, 120 (2019) 115643.
54. M. Sajid, MXenes: are they emerging materials for analytical chemistry applications?—a review, *Analytica Chimica Acta*, 1143 (2021) 267-280.
55. F. Shahzad, M. Alhabeb, C.B. Hatter, B. Anasori, S. Man Hong, C.M. Koo, Y. Gogotsi, Electromagnetic interference shielding with 2D transition metal carbides (MXenes), *Science*, 353 (2016) 1137-1140.
56. X. Zhan, C. Si, J. Zhou, and Z. Sun, MXene and MXene-based composites: synthesis, properties and environment-related applications, *Nanoscale Horizons*, 5 (2020) 235-258.

57. U.U. Rahman, M. Humayun, U. Ghani, M. Usman, H. Ullah, A. Khan, N.M. El-Metwaly, A. Khan, MXenes as emerging materials: synthesis, properties, and applications, *Molecules*, 27 (2022) 4909.
58. K. Chaturvedi, V Hada, S. Paul, B Sarma, D Malvi, M Dhargar, H Bajpai, A Singhwane, A.K. Srivastava, and S. Verma, The rise of MXene: a wonder 2D material, from its synthesis and properties to its versatile applications—a comprehensive review, *Topics in Current Chemistry*, 381 (2023) 11.
59. M. Mariano, O. Mashtalir, F.Q. Antonio, W.H. Ryu, B. Deng, F. Xia, Y. Gogotsi, and A.D. Taylor, Solution-processed titanium carbide MXene films examined as highly transparent conductors, *Nanoscale*, 8 (2016) 16371-16378.
60. L. Jiang, D. Zhou, J. Yang, S. Zhou, H. Wang, X. Yuan, J. Liang, X. Li, Y. Chen, and H. Li, 2D single-and few-layered MXenes: synthesis, applications and perspectives, *Journal of Materials Chemistry A*, 10 (2022) 13651-13672.
61. M. Tang, J. Li, Y. Wang, W. Han, S. Xu, M. Lu, W. Zhang, and H. Li, Surface terminations of MXene: synthesis, characterization, and properties, *Symmetry*, 14 (2022) 2232.
62. M. Naguib, O. Mashtalir, J. Carle, V. Presser, J. Lu, L. Hultman, Y. Gogotsi, and M.W. Barsoum, Two-dimensional transition metal carbides, *ACS Nano*, 6 (2012) 1322-1331.
63. T. Zhang, L. Pan, H. Tang, F. Du, Y. Guo, T. Qiu, and J. Yang, Synthesis of two-dimensional  $Ti_3C_2T_x$  MXene using  $HCl+LiF$  etchant: enhanced exfoliation and delamination, *Journal of Alloys and Compounds*, 695 (2017) 818-826.
64. V. Natu, R. Pai, M. Sokol, M. Carey, V. Kalra, and M.W. Barsoum, 2D  $Ti_3C_2T_z$  MXene synthesized by water-free etching of  $Ti_3AlC_2$  in polar organic solvents, *Chem* 6 (2020) 616-630.
65. A. Feng, Y. Yu, L. Mi, Y. Yu, and L. Song, Comparative study on electrosorptive behavior of  $NH_4HF_2$ -etched  $Ti_3C_2$  and HF-etched  $Ti_3C_2$  for capacitive deionization, *Ionics*, 25 (2019) 727-735.
66. W. Sun, S.A. Shah, Y. Chen, Z. Tan, H. Gao, T. Habib, M. Radovic, and M.J. Green, Electrochemical etching of  $Ti_2AlC$  to  $Ti_2CT_x$  (MXene) in low-concentration hydrochloric acid solution, *Journal of Materials Chemistry A*, 5 (2017) 21663-21668.
67. S.-Y. Pang, Y.T. Wong, S. Yuan, Y. Liu, M.K. Tsang, Z. Yang, H. Huang, W.T. Wong, and J. Hao, Universal strategy for HF-free facile and rapid synthesis of two-dimensional MXenes as multifunctional energy materials, *Journal of the American Chemical Society*, 141 (2019) 9610-9616.
68. A. Singh, N. Lalotra, S.S. Shah, M.D. Rather, EA Lopez-Maldonado, K Pathania, R.G. Abaszade, M. Stetsenko, and S. Arya, A Comprehensive Review on the Synthesis and Properties of MXenes for Supercapacitor Applications, *Applied Energy Materials*, 8 (2025) 4884-4914.
69. Y. Wei, P. Zhang, R.A. Soomro, Q. Zhu, and B. Xu, Advances in the synthesis of 2D MXenes, *Advanced Materials*, 33 (2021) 2103148.

70. P. Urbankowski, B. Anasori, T. Makaryan, D. Er, S. Kota, P.L. Walsh, M. Zhao, V.B. Shenoy, M.W. Barsoum, and Y. Gogotsi, Synthesis of two-dimensional titanium nitride  $Ti_4N_3$  (MXene), *Nanoscale*, 8 (2016) 11385-11391.
71. Q. Zhong, Y. Li, and G. Zhang, Two-dimensional MXene-based and MXene-derived photocatalysts: Recent developments and perspectives, *Chemical Engineering Journal*, 409 (2021) 128099.
72. Y. Guo, S. Jin, L. Wang, P. He, Q. Hu, L.-Z. Fan, A. Zhou, Synthesis of two-dimensional carbide  $Mo_2CT_x$  MXene by hydrothermal etching with fluorides and its thermal stability, *Ceramics International*, 46 (2020) 19550-19556.
73. C. Peng, P. Wei, X. Chen, Y. Zhang, F. Zhu, Y. Cao, H. Wang, H. Yu. and F. Peng, A hydrothermal etching route to synthesis of 2D MXene ( $Ti_3C_2$ ,  $Nb_2C$ ): Enhanced exfoliation and improved adsorption performance, *Ceramics International*, 44 (2018) 18886-18893.
74. S. Husmann, Ö. Budak, H. Shim, K. Liang, M. Aslan, A. Kruth, A. Quade, M. Naguib, V. Presser, Ionic liquid-based synthesis of MXene, *Chemical Communications*, 56 (2020) 11082-11085.
75. J. Mei, G.A. Gayoko, C. Hu, J.M. Bell, and Z. Sun, Two-dimensional fluorine-free mesoporous  $Mo_2C$  MXene via UV-induced selective etching of  $Mo_2Ga_2C$  for energy storage, *Sustainable Materials and Technologies*, 25 (2020) e00156.
76. A.E. Ghazaly, H. Ahmed, A.R. Rezk, J. Halim, P.O. Persson, L.Y. Yeo, and J. Rosen, Ultrafast, one-step, salt-solution-based acoustic synthesis of  $Ti_3C_2$  MXene, *Nano*, 15 (2021) 4287-4293.
77. J. Mei, G.A. Gayoko, C. Hu, and Z. Sun, Thermal reduction of sulfur-containing MAX phase for MXene production, *Chemical Engineering Journal*, 395 (2020) 125111.
78. J.-C. Gui, L. Han, and W. Cao, Lamellar MXene: A novel 2D nanomaterial for electrochemical sensors, *Journal of Applied Electrochemistry*, 51 (2021) 1509-1522.
79. C. Xu, L. Wang, Z. Liu, L.Chen, J. Guo, N. Kang, X.L. Ma, H.M. Chen, and W. Ren Large-area high-quality 2D ultrathin  $Mo_2C$  superconducting crystals, *Nature Materials*, 14 (2015) 1135-1141.
80. Y. Zhou, Y. He, T. Zhang, Y. Xu, K.Qu, Z. Cui, and J.Chen, A MXene-based molecularly imprinted electrochemical sensor for sensitive detection of chloramphenicol in aquaculture seawater, *Microchemical Journal*, (2026) 117257.
81. H. Essousi, J. Wannassi, A. Elloumi, E. Ali, and H. Barhoumi, Electrochemical sensor of oxytetracycline based on molecularly imprinted poly (3,4-ethylenedioxythiophene)/MXene on graphene screen printed electrode, *Microchemical Journal*, (2025) 114425.
82. Z. Yang, J Hu, X Zhang, H Yang, P Meng, H Zhao, and Y. Sun, MXene-based composites as an electrochemical sensor for ultrasensitive determination of ofloxacin, *Microchemical Journal*, 415 (2023) 157-166.
83. B. Zhang, Y. Han, Y. Chen, C. Wang, G. Fang, and S.Wang, Fabrication of surface molecularly imprinted electrochemical sensor based on  $V_2CT_x$  MXene heterogeneous

- functionalized Au-PtRu nanoalloy for the sensitive detection of chlortetracycline in food, *Food Chemistry*, (2025) 145644.
84. Y. Wang, W. Hao, M. Guo, L. Cai, B. Zhang, G. Fang, and S. Wang, Fabrication of a new molecularly imprinted electrochemical sensor by AgNWs/Ti<sub>3</sub>C<sub>2</sub>T<sub>x</sub> synergistic AuNPs for ultrasensitive and targeted detection of sulfathiazole in food, *Microchemical Journal*, (2025) 114217.
  85. A.E. Vilian, S.K. Hwang, G. Bhaskaran, M. Ahlammadi, S. Kim, J.N. Tiwari, Y.S. Huh, and Y.K. Han, Polypyrrole-MXene supported gold nanoparticles for the trace-level detection of nitrofurantoin, *Chemical Engineering Journal*, 454 (2023) 139980.
  86. L. Kabir, Y.J. Joo, K.Y. Cho, and W.C. Oh, Optimized and cost-effective electrochemical sensor based on Self-Assembly of 2D/3D MXene/Metal oxides nanocomposite for identification of antibiotics, *Inorganic Chemistry Communications*, 174 (2025) 113935.
  87. B. Shen, B. Hong, X. Guo, R. Hu, L. Wang, Y. Jiang, W. Li, W. Liu, Z. Wu, and P. Yang, Facile fabrication of sensing electrode based on CoFe-MOFs/MXene for ultrasensitive detection of picomolar chloramphenicol, *Talanta*, 286 (2025) 127552.
  88. S. Xiong, Z. Wu, F. Li, P. Zhao, H. Li, H. Bao, and X. Yang, Self-assembled sensing interface based on specific aptamer functionalized Ti<sub>3</sub>C<sub>2</sub> MXene for ultrasensitive antibiotic detection in milk, *LWT*, 200 (2024) 116186.
  89. Y. Qi, Y. Chen, Q. Li, X. Dang, and H. Chen, A novel ratiometric electrochemical sensing platform combined with molecularly imprinted polymer and Fe-MOF-NH<sub>2</sub>/CNTs-NH<sub>2</sub>/MXene composite for efficient detection of ofloxacin. *Analytica Chimica Acta*, 1316 (2024) 342876.
  90. P. Dong, F. Li, Z. Wu, L. Xue, M. Luo, Y. Tan, H. Li, and X. Yang, Liquid Exfoliated Graphene/Ti<sub>3</sub>C<sub>2</sub> MXene Composite Based Aptasensor for Ultrasensitive Electrochemical Detection of Chloramphenicol in Milk and Honey, *Food Analytical Methods*, 18 (2025) 2063-2075.
  91. G. Zhang, Z. Wang, R. Jamal, T. Abdiryim, F. Xu, Y. Zhou, S. Xie, K. Song, J. Li, L. Ma, and J. Tan, Defect-rich Co, N-doped Ti<sub>3</sub>C<sub>2</sub>T<sub>x</sub>/C/poly (3, 4-ethylenedioxy thiophene) molecularly imprinted sensor for ultrasensitive electrochemical detection of gatifloxacin, *Talanta*, (2025) 128364.
  92. S. Kotteeswaran, S. Kondee, W. Pon-On, W.H. Al-Qahtani, C. Wongchoosuk, and M. Govindasamy, CuZnS microflowers anchored on MXene nanosheets based electrochemical sensor for pico-molar determination of chloramphenicol in biological samples and dairy products, *Microchemical Journal*, 212 (2025) 113291.
  93. M. Liu, T. Zhe, L. Zhu, F. Li, K. Ma, C. Xuan, Q. Feng, S. Ouyang, and L. Wang, Interfacial engineering of VS<sub>2</sub>/Ti<sub>3</sub>C<sub>2</sub>T<sub>x</sub> MXene heterojunctions for portable electrochemical sensing of nitrofurantoin residues in food and water samples. *Food Chemistry*, (2025) 144624.
  94. Y. Liang, G. Qu, K. Pan, Y. Yuan, and J. Li, Sensitive electrochemical sensor for the detection of ciprofloxacin by reduced graphene oxide-loaded spherical silver nanoparticles, *Microchemical Journal*, 213 (2025) 113796.

95. B. Parasuraman, S. Chinnapaiyan, B. Kandasamy, P. Shanmugam, A.A. Alothman, P. Thangavelu, and C.-H Huang, Fabrication of dual-functional smart materials: 2D-WO<sub>3</sub>/rGO nanocomposite for electrochemical detection and photocatalytic degradation of tetracycline, *Sensors and Actuators A: Physical*, 379 (2024) 115873.
96. X. Deng, Z. Yi, Y. Xiong, X. Gao, R. Huang, X. Chen, D. Deng, C. Xiong, J. Zhang, and G. Huang, Molecularly imprinted ratiometric electrochemical sensor based on 3D-1D MoS<sub>2</sub>@CNTs hetero-nanoflower for selective detection of trimethoprim, *Microchemical Journal*, 201(2024) 110522.
97. K.-Y. Hwa, A. Santhan, A. Ganguly, and R. Murugan, Vanadium selenide encapsulated β-Cyclodextrin/rGO nanosheets: An effective electrochemical detection of antibiotic in environmental aquatic and biological samples, *Journal of the Taiwan Institute of Chemical Engineers*, 165 (2024) 105749.
98. K. Zhang, Z. Shi, Y. Li, X. Wu, Z. Ma, W. Sun, C.M. Li, and C. Guo, Graphdiyne chelated iron-based metal–organic frameworks for electrochemical sensing of antibiotic chloramphenicol with ultralow detection limit, *Microchemical Journal*, 201 (2024) 110526.
99. Y. Zhou, A. Abdurexit, R. Jamal, T. Abdiryim, X. Liu, F. Liu, F. Xu, Y. Zhang, and Z. Wang, Highly sensitive electrochemical sensing of norfloxacin by molecularly imprinted composite hollow spheres, *Biosensors and Bioelectronics*, 251 (2024) 116119.
100. B.K. Raja, S. Ramar, M. K. Muthukumaran, and A. Suvitha, CeVO<sub>4</sub>–Wakefieldite Nanocubes Supported on a Triazine-Based 2D Polymer as an Electrochemical Sensing System for the Detection of Levofloxacin in Human Blood Serum, *Applied Nano Materials*, 8 (2025) 17910-17922.
101. Sahil, V.B. Jaryal, R. Sharma, K.K. Thakur, F.S. Ataya, N. Gupta, and D. Singh, Facile One-Pot Synthesis of Fe<sub>3</sub>O<sub>4</sub>– MoS<sub>2</sub>@MXene Nanocomposite as an Electrochemical Sensor for the Detection of Levofloxacin, *ChemistrySelect*, 10 (2025) e202405959.
102. R. Sharma, S. Kumar, D.S. Rana, S. Thakur, N. Gupta, D. Singh, Molybdenum disulfide nanostructure grown on multi-walled carbon nanotube for the electrochemical detection of ofloxacin, *Journal of Environmental Chemical Engineering*, 12 (2024) 112413.
103. S. Chen, J. Guo, Q. Sun, Y. Wang, M. Du, A. Wang, X. Yu, and L. Ding, Enhanced electrochemical sensor based on UiO-66-NH<sub>2</sub>/carbon nanotubes hybrid for selective detection of ofloxacin, *Materials Today Chemistry*, 42 (2024) 102441.



---

## Materials & Experimental Techniques

---

### 2.1 Introduction

This chapter describes about the materials and various experimental techniques used in the fabrication of MXene and its composite-based electrochemical sensor for antibiotic detection. Furthermore, several analytical approaches have been used to characterize  $Ti_3C_2T_x$ ,  $TiO_2-Ti_3C_2T_x$ ,  $CuS/Ti_3C_2T_x$ ,  $Ag/TiO_2-Ti_3C_2T_x$  and other modified electrodes. An attempt has also been made to discuss methodologies and strategies used to determine several factors related to the efficacy of synthesized materials for antibiotic detection. Additionally, various protocols used to calculate the number of matrices for determining the reliability of the electrochemical sensor have also been reported.

### 2.2 Materials

The detailed description of the materials used during experimentation is discussed in the following sections:

#### 2.2.1 Chemicals

Titanium aluminium carbide ( $Ti_3AlC_2$ , size  $\leq 100\mu m$ ), lithium fluoride (LiF), sodium tetrafluoroborate ( $NaBF_4$ ), levofloxacin (LEV,  $\geq 98\%$ ), norfloxacin (NOR,  $\geq 98\%$ ), ciprofloxacin (CIP,  $\geq 98\%$ ), omeprazole (OME), ampicillin (AMP,  $\geq 95\%$ ), azithromycin dihydrate (AZY,  $\geq 98\%$ ), pyrrole, glucose and silver nitrate ( $AgNO_3$ ) were all procured from Sigma-Aldrich, India. Hydrochloric acid (HCl), ethanol, sodium chloride (NaCl), potassium phosphate ( $KH_2PO_4$ ), dibasic potassium phosphate ( $K_2HPO_4$ ), copper sulphate pentahydrate ( $CuSO_4.5H_2O$ ,  $\geq 98\%$ ) were taken from Thermo-Fischer Scientific while

sodium thiosulfate pentahydrate ( $\text{Na}_2\text{SO}_3 \cdot 5\text{H}_2\text{O}$ ) and sodium hydroxide ( $\text{NaOH}$ ) were purchased from Qualigens. Indium tin oxide (ITO, resistivity  $\leq 10$  ohms/sq.) coated glass was procured from Techinstro. All the solutions including buffer were prepared with Milli-Q water ( $18.2 \text{ M}\Omega \text{ cm}$ ).

### 2.2.2 Buffers

- 0.1 M Phosphate buffer saline (PBS), 7.0 pH, NaCl (0.9%).
- PBS containing 5mM  $[\text{Fe}(\text{CN})_6]^{3-/4-}$  as redox indicator.

### 2.3 Analytical Techniques

The work presented in this thesis includes (i) the preparation of  $\text{Ti}_3\text{C}_2\text{T}_x$  (MXene) and its composites followed by the deposition of synthesised materials film onto the ITO glass surface and (ii) the formation of MIP layer onto the fabricated electrode by using electropolymerization technique followed by the elution process to study their potential application for antibiotic detection. The synthesised materials and polymerized electrodes were characterized at different stages of fabrication by a range of techniques like X-ray diffraction (XRD), Fourier transform infrared (FT-IR), Raman spectroscopy for structural and field emission electron microscopy (FE-SEM), elemental analysis (EDX) for morphological and electrochemical techniques, namely, cyclic voltammetry (CV), electrochemical impedance spectroscopy (EIS) and differential pulse voltammetry (DPV).

#### 2.3.1 X-Ray Diffraction (XRD)

This non-destructive structural characterisation technique is used to investigate the crystalline nature and chemical composition of unknown materials [1]. With this technique, the atomic structure of macromolecules can be determined whereas for small-scale materials, it can identify their crystallinity, strain, crystal size and structure as well as their composition [2]. The structural information of the sample including crystallite size, crystallographic structure, interplanar distance, defects, polycrystalline orientation

distribution and band angles can all be deduced with this technique. The working principle of this technique is based on Bragg's law, which describes how an X-ray beam incident on the sample's crystal lattice is reflected at a particular angle providing details about the sample's crystalline structure or phases based on the intensity and location of the peak. The XRD spectrum is recorded using an X-ray diffractometer. **Fig. 2.1** shows the fundamental pictorial representation of the X-ray diffractometer setup.

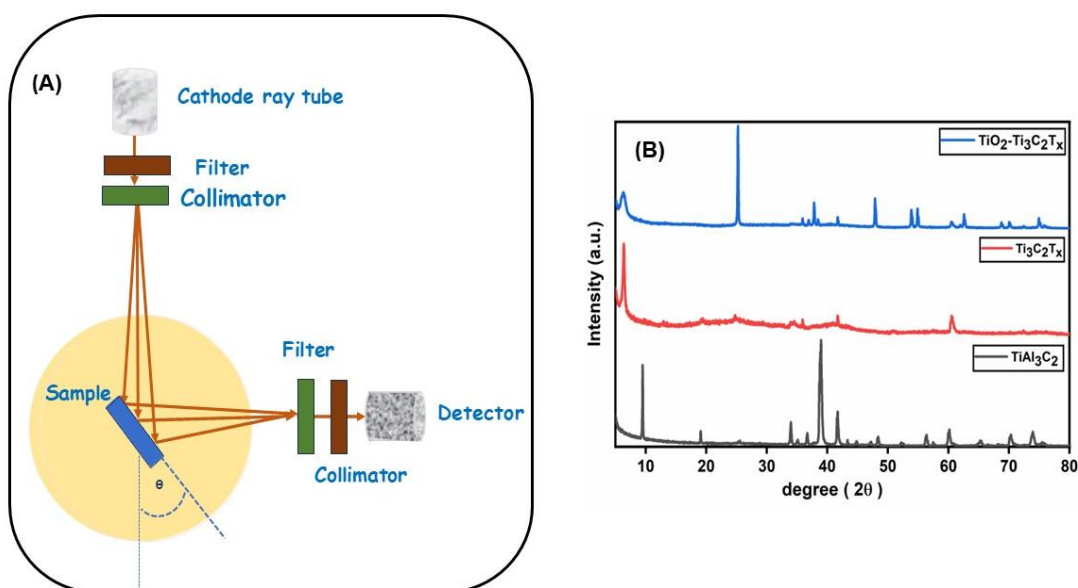


**Fig. 2.1** (A) Pictorial illustration of XRD (B) XRD pattern of  $\text{TiAl}_3\text{C}_2$ ,  $\text{Ti}_3\text{C}_2\text{T}_x$  and  $\text{TiO}_2\text{-Ti}_3\text{C}_2\text{T}_x$

The most prominent diffraction peaks are utilized to determine the average peak broadening and acquire the peak broadening data. Thereafter, the material's structural characteristics can be analysed using this information. The Debye-Scherrer equation (**Eq. 2.1**) has been used to calculate the average particle size of any material by analysing peak broadening in the XRD pattern [3].

$$D = K \lambda / \beta \cos \theta \quad (2.1)$$

In this equation, D represents the particle crystalline size, K denotes the Scherrer constant (0.98),  $\lambda$  is the wavelength of X-ray beam,  $\theta$  is the Bragg's angle and  $\beta$  represents the full-

width at half maxima. In this thesis, the Malvern Empryean X-ray diffractometer, having a monochromatic radiation of wavelength 1.54 Å with diffraction angle  $2\theta = 5-80^\circ$  and speed  $2^\circ/\text{min}$  has been used to carry out the structural analysis of all the synthesised materials like  $\text{Ti}_3\text{C}_2\text{T}_x$  (MXene) and its composites and modified electrodes.

### **2.3.2 Fourier Transform Infrared (FT-IR) Spectroscopy**

The Fourier transform infrared spectrometer is based on infrared radiation which examines the interaction of electromagnetic radiation with the material. Due to its superior sensitivity, high accuracy, ease of handling and rapid analysis, it is widely used to investigate the presence of functional groups, vibrational changes and structural changes in the sample. The basic principle of FT-IR is based on the molecule's atomic vibration which absorbs infrared radiation at particular frequencies or energies. When the sample absorbs electromagnetic radiation from the laser beam at each wavelength, it results in various spectral lines which further reveal the composition of the materials or chemical substances [4].

The Michelson interferometer in FT-IR spectroscopy examines the chemical composition of any material. Its basic setup consists of four main components: (a) filament (light source), (b) beam splitter, (c) two mirrors, and (d) detector, as shown below in **Fig.2.2**. The source emits infrared radiation, which is then divided into two portions via the beam splitter. These two separate light beams continue to travel along two different paths as they are reflected off the end mirrors. After reflection, these distinct beams recombine to produce interference which the detector then analysed. FT-IR is an efficient characterisation technique that offers numerous benefits over dispersive measurements including a wider spectral range, increased sensitivity, faster data acquisition, reduced sample requirement and an improved signal-to-noise ratio [5]. The Perkin Elmer Spectrum 2 with frequency range of  $400-4000\text{ cm}^{-1}$  was used in attenuated total reflection (ATR) mode to examine the functional groups present in all the synthesised materials.

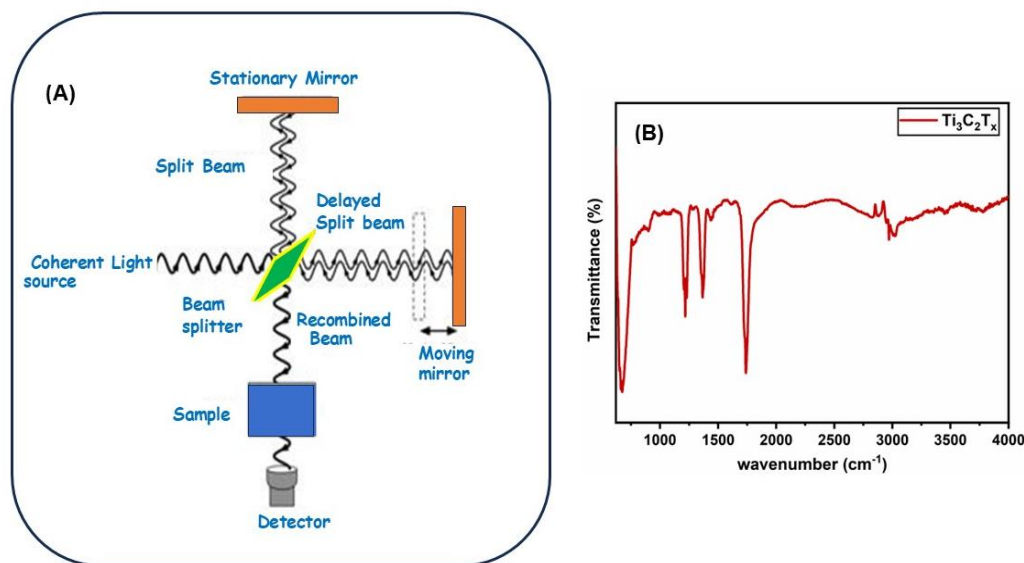


**Fig. 2.2** (A) Schematic illustration of a Michelson interferometer (B) FT-IR spectra of Ti<sub>3</sub>C<sub>2</sub>T<sub>x</sub>

### 2.3.3 Raman Spectroscopy

Raman spectroscopy is another sophisticated tool that emerged with the discovery of the well-known Raman effect. This phenomenon occurs when monochromatic light is inelastically scattered by the compound causing the reflected light to be emitted at distinct wavelengths that differ from those of the incident light. The effect of light on molecular vibration provides insight into molecular structure or aids in the identification of functional groups. This technique utilises a laser as the source beam and the laser's bandwidth determines the spectral radiation. Afterwards, the sample molecule is placed in the chamber that accepts the laser beam and then the dispersed light is transmitted through high-quality filters which further distinguish the Rayleigh scattered light (elastic scattering) and Raman scattered light (inelastic scattering) preventing additional laser simulations [6]. The light is then focused on the detector as it passes through the grating. The compound's spectrum then displays a range of weak and strong bands reflecting its distinct characteristics. By analyzing the spectra, several factors including crystallinity, amorphous behaviour,

chemical composition and tacticity can be discovered [7]. In this thesis, Raman spectrometer (Model: Invia Reflex) equipped with a laser source of 532 nm was used to collect the data of  $\text{Ti}_3\text{C}_2\text{T}_x$  and  $\text{TiO}_2\text{-Ti}_3\text{C}_2\text{T}_x$  composite (**Fig. 2.3**).

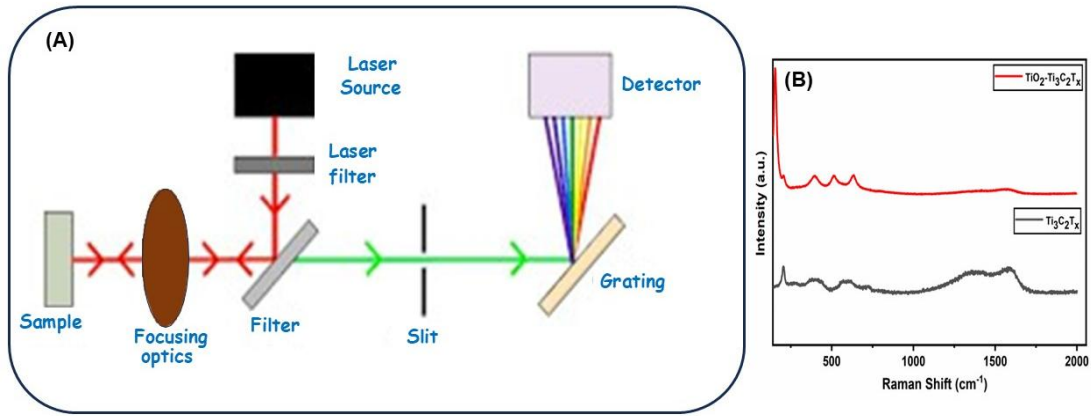


**Fig. 2.3** (A) Schematic diagram of a Raman spectrometer (B) Raman spectrum of  $\text{Ti}_3\text{C}_2\text{T}_x$  and  $\text{TiO}_2\text{-Ti}_3\text{C}_2\text{T}_x$

### 2.3.4 Field Emission Scanning Electron Microscopy (FESEM)

The sample's surface morphology can be examined via FESEM. Instead of using light, the FESEM uses electrons to observe the sample's image. Compared to other microscopes, FESEM offers the benefits of a higher depth of field enabling simultaneous access to more specimens. The primary components of FESEM are: an electron source (Field emission gun), a column that allows the electron beam to pass through electromagnetic lenses, an electron detector, a specimen chamber, a computer and a display unit to see the images. As seen in **Fig. 2.4**, the FESEM produces signals at solid objects' surface using the focused highly energetic electron beam [8]. This technique operates by generating high-energy electrons at the uppermost part of the column which are then accelerated in the downward direction before travelling to several lenses and striking the specimen surface in a focused beam. Furthermore, FESEM utilizes a series of pumps to create a vacuum condition inside the specimen chamber generating the specimen micrographs [9, 10]. The interaction between the specimen and the electron generates signals that are then perceived by the detector. In

the present work, the morphology of the surface of all the prepared materials and modified electrodes was studied by using FESEM (Zeiss Gemini SEM 500).

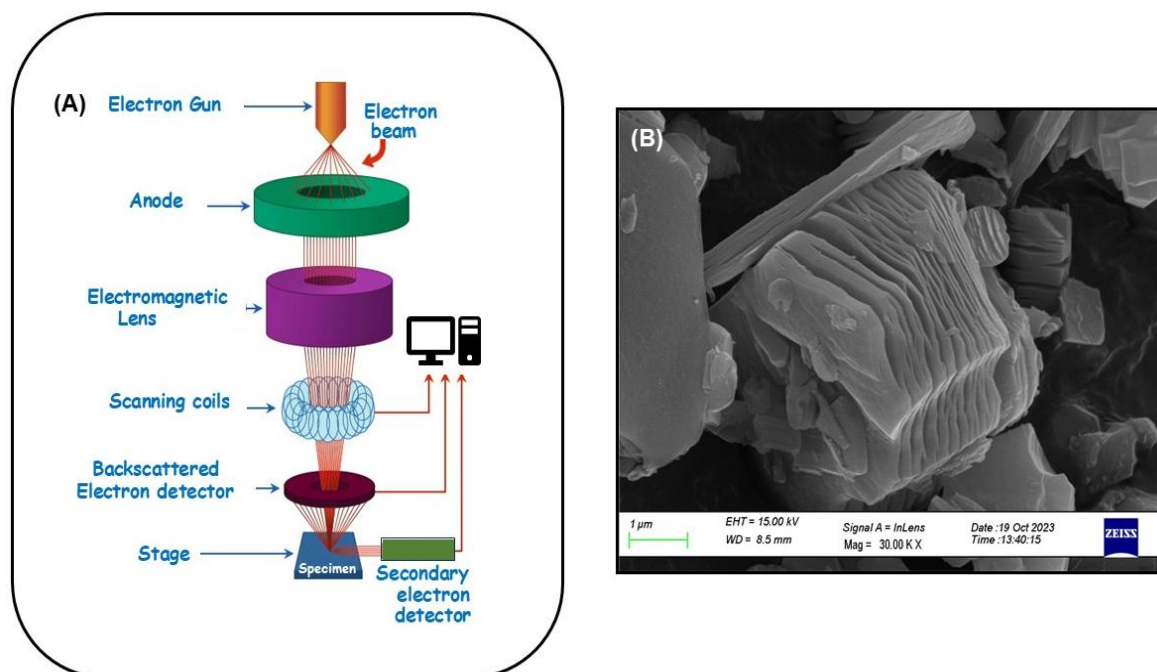


**Fig. 2.4 (A)** Pictorial view of FESEM **(B)** FESEM image of  $\text{Ti}_3\text{C}_2\text{T}_x$

### 2.3.5 Energy Dispersive X-ray (EDX) Analysis

This technique provides a compressive mapping of the sample by examining near-surface elements and approximates the elemental proportions at various positions. The basic fundamentals of EDX are applied in conjunction with FESEM. The material under examination produces X-rays when an electron beam (10-20 keV) hits the surface of sample and resulting X-ray is unique to each element. Therefore, this characteristic X-ray is used to identify and quantify chemical constituents in the sample. During EDX analysis, an image of the elements present in the sample is generated by moving the electron beam across it. In EDX, the composition and the amount of heavy metal ions of the nanoparticles that are present near or at the sample's surface can be readily detected but for elements with atomic number below 11 are difficult to detect. For instance, EDX makes it easy to recognize gold, silver and palladium surface-bound nanoparticles [11]. In this thesis,

elemental analysis of all the synthesized materials was performed using FESEM-EDX (Zeiss Gemini SEM 500).

### **2.3.6 Electrochemical Techniques**

Electroanalytical techniques are being used to measure the responses in terms of potential or current within an electrochemical cell. This technique is highly useful for determining the chemical reactivity of an analyte by capturing data for changes in potential or current with respect to analyte concentration when an electric potential is applied. In the majority of electrochemical experiments, a three-electrode system containing a working electrode (WE), a reference electrode (RE) and a counter or auxiliary electrode (CE) is generally used to evaluate the electrochemical properties of the compound being tested [12]. These electrodes are successfully connected to a potentiostat, a device that measures the resulting current by regulating the working electrodes' potential. In an electrochemical experiment, when a working electrode is subjected to a potential, the resulting current response is measured and plotted counter to time. In other cases, when the applied potential varied linearly, the obtained current is plotted against the applied potential. Nernst's equation provides a quantitative aspect of potential (E) in an electrolytic solution for the known concentration of the reduced and oxidised forms of the redox couple as shown by **Eq. 2.2**.

$$E = E_o + (RT/nF) \ln ([C_{oxi}]/[C_{red}]) \quad (2.2)$$

Here,  $E_o$  represent the potential of the electrode, R is the gas constant, T is the temperature, F denotes the Faraday's constant and  $[C_{oxi}]$  and  $[C_{red}]$  signify the concentration of oxidized and reduced species. The operation of the three-electrode system depends on the applied voltage and the redox species reacting at the electrode surface controls the concentration ratio to satisfy the Nernst equation.

In this thesis, the Autolab (Ecochemie, Netherlands) Potentiostat/Galvanostat instrument, featuring Ag/AgCl (reference) and platinum (counter) electrodes has been utilized to

perform electrochemical characterizations (Cyclic voltammetry, Differential pulse voltammetry) of all the fabricated sensors. A potentiostat utilizes a DC power source to generate a steady current at a constant voltage thereby achieving a precise, controlled and stable potential. **Fig.2.5** represents the schematic picture of the electrochemical workstation.

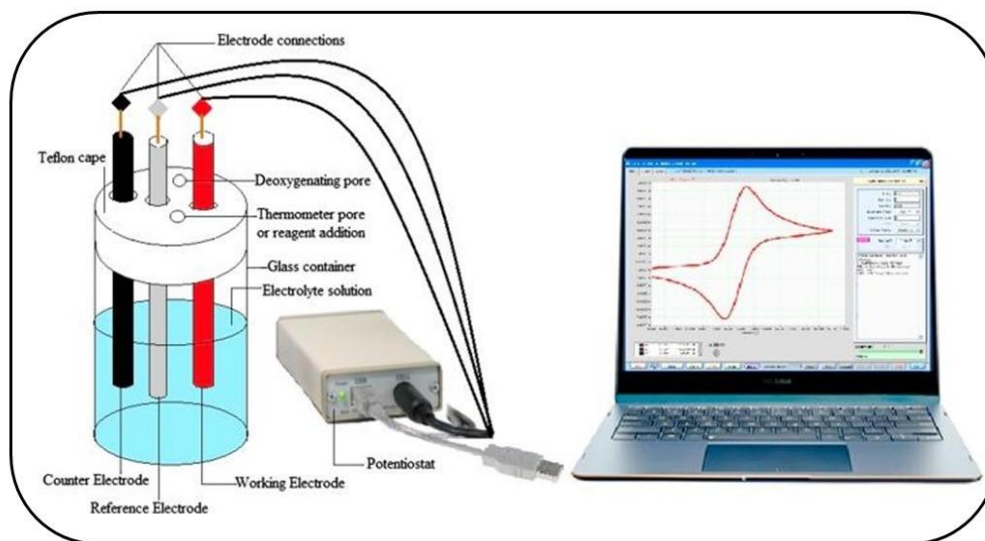


**Fig. 2.5** Schematic diagram of the working of the Potentiostat

### 2.3.6.1 Cyclic Voltammetry (CV)

CV is one of the most useful electroanalytical methods to examine the electrochemical processes of an electroactive species. During CV experiments, the working electrode's potential varied linearly over time. In this study, the sweeping potential of the working electrodes is swept in one direction across time and then returned to its original point in the opposite direction once it reaches the fixed point. In order to create CV graphs, these potential cycles, as required, can be swept at different scan rates. Moreover, CV provides more insight into the electrochemical reactions with known redox potential for the electroactive species. The electrons are transferred from the source signal to WE through CE and the current is monitored at WE during a potential scan against RE. During the oxidation-reduction process, an electrolytic solution is required to supply the ions to the electrodes [13]. The efficiency of fabricated electrodes can be examined by calculating

various physical parameters using the obtained peak current during the CV studies. Using Laviron's theory, charge transfer coefficient ( $\alpha$ ) and heterogeneous rate transfer constant ( $K_s$ ) can be calculated using **Eqs. 2.3 to 2.5**.

$$E_{pa} = 2.303 RT/(1-\alpha) nF; \text{ and } E_{pc} = 2.303 RT/\alpha n F \quad (2.3)$$

$$\Delta E_p = E_{pa} - E_{pc} \quad (2.4)$$

$$\ln K_s = \alpha \cdot \ln (1-\alpha) + (1-\alpha) \cdot \ln(\alpha) \ln (RT/n F v) - \alpha (1-\alpha) \cdot n F \cdot \Delta E_p/RT \quad (2.5)$$

Here,  $E_{pa}$  and  $E_{pc}$  are the anodic and cathodic peak potentials and  $v$  is the scan rate.

Other electrochemical parameters such as diffusion coefficient ( $D$ ), surface coverage ( $\tau$ ) [14] can be computed by using the Randles-Sevick equation:

$$I_p = 2.69 \times 10^5 n^{3/2} A C D^{1/2} v^{1/2} \quad (2.6)$$

$$I_p = n^2 F^2 A \tau v / 4RT \quad (2.7)$$

Where  $I_p$ ,  $n$ , and  $C$  represent the anodic peak current, oxidized or reduced electrons and molar concentration of  $[\text{Fe}(\text{CN})_6]^{3-/4-}$  in mole/cm<sup>3</sup>. In this thesis, CV studies were performed at different scan rates ranging from 10 to 300 mVs<sup>-1</sup> for all modified electrodes to examine their electrochemical characteristics.

### **2.3.6.2 Electrochemical Impedance Spectroscopy (EIS)**

EIS is a powerful electroanalytical technique that is used to examine the electrochemical behaviour at the conducting electrode and electrolyte interface. For an ideal resistor, Ohm's law specifies the power of an individual component of an electric circuit to resist the current flow (Resistance,  $R$ ). This is expressed in terms of the ratio between the voltage ( $V$ ) and current ( $I$ ). However, the properties of such circuits cannot be applied or utilized in the real world due to their complex behaviour, thus impedance takes precedence over the concept of resistance. The most popular method for determining the electrochemical impedance is to apply an AC potential to an electrochemical cell and then analyse the resulting current flow. Most likely, the generated AC signals are analyzed by using a sinusoidal potential simulation [15].

Electrochemical impedance is measured by using a small excitation pulse to obtain a pseudo linear response from the electrochemical cell. When a sinusoidal potential is applied to a linear system, the matching current exhibits a sinusoidal waveform with the same frequency regardless of the phase shift. The significant properties of an electrochemical system can be obtained by modelling the impedance data in terms of  $R_{ct}$  (charge transfer resistance),  $R_s$  (solution resistance),  $C_{PE}$  (constant phase element) and  $C_{dl}$  (double layer capacitance).  $Z_w$  (Warburg element) represents the mass transport impedance or the cell's diffusion. In an electrochemical cell, the complex electrochemical reaction that occurs at the electrode-electrolyte interface is stimulated by the equivalent circuit model. EIS spectra are represented and analysed by Nyquist plots which comprise both real and imaginary impedance components along the X and Y axis [16].

This thesis presents the calculation of charge transfer resistance ( $R_{ct}$ ) through fitting the acquired EIS spectra, utilizing the modified Randles equivalent circuit model. By using the obtained  $R_{ct}$  values, the exchange current per unit area ( $i_o$ ) and heterogeneous electron transfer rate constant ( $K_{app}$ ) were estimated using Eqs. 2.8 and 2.9.

$$i_o = nRT/R_{ct}F \quad (2.8)$$

$$k_{app} = RT/n^2F^2AR_{ct}C \quad (2.9)$$

where  $n$  is the number of transferred electrons,  $R$  is the universal gas constant,  $T$  is the temperature (Kelvin),  $F$  is Faraday's constant,  $A$  represents the geometric area of the electrode, and  $C$  denotes the redox-probe concentration [17].

### **2.3.6.3 Differential Pulse Voltammetry (DPV)**

DPV is an advanced and more sensitive electrochemical technique that offers a better detection limit and improved resolution processes compared to cyclic voltammetry. DPV operates by applying a linearly ramped potential to the working electrode subjected to a voltage versus time programme. This technique computes the current difference ( $\Delta I$ ) before

and after the pulse, thereby successfully distinguishing the faradaic current (originating from the analyte's redox reactions) from the non-faradaic current. The current between the pulse voltage and ramped baseline voltage is reported after a sequence of small pulses has been superimposed on a slowly increasing linear potential ramp. The current for each pulse is measured at two different points: once before the pulse (called the baseline) and after the pulse when the system has stabilised [18]. The difference between these two measurements represents the differential current. DPV reduces background noise interference by separating the faradaic current thereby enhancing sensitivity and making it suitable for low-concentration analytes. DPV currents offer a higher detection limit compared to CV and other voltammetric techniques due to their superior ability to distinguish between charging current and faradaic impurity current.

## **2.4 Protocols Used for the Determination of Various Performance-related Parameters for MXene and its Composite-based Electrochemical Sensor**

### **2.4.1 Linear Range, Detection Limit and Sensitivity**

The concentration ranges across which the current response varies proportionally with various analyte concentrations demonstrates the sensor's linearity range. In this thesis, DPV (Chapters 3, 4 and 6) and EIS (Chapter 5) methods have been used to determine the linear range.

The lowest concentration of the analyte that can be detected by the sensor is known as the detection limit (LOD) and can be computed using the following expression (**Eq. 2.10**).

$$\text{LOD} = 3\sigma/S \quad (2.10)$$

Here,  $\sigma$  represents the electrode's standard deviation and S is the slope of the calibration plot.

The sensitivity of the sensor refers to the correlation between the variation in analyte concentration and the strength of the signal produced by the transducer. Generally, a sensor should be able to identify and provide a signal for even the slightest variation in the target analyte's concentration.

$$\text{Sensitivity} = \text{slope}/\text{effective surface area of the working electrode} \quad (2.11)$$

### **2.4.2 Selectivity, Reproducibility and Stability**

Selectivity of a sensor refers to the ability of a recognition probe to precisely identify the target analyte even in the presence of other potential sources of interference substances. Meanwhile, the sensor's longevity has been determined by its stability and reproducibility. The stability or shelf life of a sensor refers to how long it functions appropriately while maintaining its maximum efficiency during storage which can be monitored by measuring the current at regular time intervals. On the other hand, reproducibility measures the drift or scatter in a sequence of observations or discoveries made over time.

**References**

1. A. Ali, Y.W. Chiang, and R.M. Santos, X-ray diffraction techniques for mineral characterization: A review for engineers of the fundamentals, applications, and research directions, *Minerals* 12 (2022) 205.
2. G. Rajender, and P.K. Giri, Strain induced phase formation, microstructural evolution and bandgap narrowing in strained TiO<sub>2</sub> nanocrystals grown by ball milling, *Journal of Alloys and Compounds* 676 (2016) 591-600.
3. J. Epp, X-ray diffraction (XRD) techniques for materials characterization, *Materials characterization using nondestructive evaluation (NDE) methods*, Elsevier, (2016) 81-124.
4. F. Mangolini and A. Rossi, Attenuated total reflection-Fourier transform infrared spectroscopy: a powerful tool for investigating polymer surfaces and interfaces, *Polymer Surface Characterization* (2014) 113-152.
5. J.M. Chalmers, H.G.M. Edwards, and M.D. Hargreaves, Vibrational spectroscopy techniques: basics and instrumentation, *Infrared and Raman Spectroscopy in Forensic Science*, (2012) 9-44.
6. E. Smith, and G. Dent, *Modern Raman spectroscopy: a practical approach*, John Wiley & Sons, (2019).
7. J.R. Ferraro, K. Nakamoto, and C.W. Brown, Chapter 1-basic theory, *Introductory Raman Spectroscopy*, 2 (2003) 1-94.
8. R.S. Prabhu, R. Priyanka, M. Vijay, and G.R.K. Vikashini, Field Emission Scanning Electron Microscopy (Fesem) with a very big future in pharmaceutical research, 11 (2021) 183-187.
9. W. Zhou, R. Aparkian, Z.L. Wang, and D. Joy, Fundamentals of scanning electron microscopy (SEM), in *Scanning microscopy for nanotechnology: techniques and applications*, (2006 ) 1-40.
10. J.I. Goldstein, D.E. Newbury, J.R. Michael, N.W. Ritchie, J.H.J. Scott, and D.C. Joy, *Scanning electron microscopy and X-ray microanalysis*, Springer (2017)
11. T.R. Shojaei, S. Soltani, and M. Derakhshani, Synthesis, properties, and biomedical applications of inorganic bionanomaterials, *Fundamentals of bionanomaterials*, Elsevier (2022) 139-174.
12. S. Verma, C.M. Pandey, and D. Kumar, A highly efficient rGO grafted MoS<sub>2</sub> nanocomposite for dye adsorption and electrochemical detection of hydroquinone in wastewater, *New Journal of Chemistry*, 46 (2022) 21190-21200.
13. N. Elgrishi, K.J. Rountree, B.D. McCarthy, E.S. Rountree, T.T. Eisenhart, J.L. Dempsey, *A practical beginner's guide to cyclic voltammetry*, 95 (2018) 197-206.
14. D. Hudda, and D. Kumar, Molecularly imprinted polypyrrole decorated Ti<sub>3</sub>C<sub>2</sub>T<sub>x</sub> electrochemical sensor for highly selective and sensitive detection of levofloxacin, *Journal of Materials Science*, 59 (2024) 21684-21695.
15. Bavafa-Toosi, Y.J.I.t.L.C.S., 6-Nyquist plot. 2019, Academic Press. p. 533-640.
16. N. Zhang, M.A. Halali, and C.F. de Lannoy, Detection of fouling on electrically conductive membranes by electrical impedance spectroscopy, 242 (2020) 116823.

17. S. Chatterjee, H. Singh, D. Hudda, Sweety, and D. Kumar, A Novel Acetylcholinesterase-Based Electrochemical Biosensor Using g-C<sub>3</sub>N<sub>4</sub>@ MoS<sub>2</sub> Nanohybrid for the Detection of Trichlorfon, *Applied Organometallic Chemistry* 38 (2024) e7721.
18. A.J. Bard, L.R. Faulkner, and H.S. White, *Electrochemical methods: fundamentals and applications*, John Wiley & Sons (2022).



## MXene-based Molecularly Imprinted Electrochemical Sensor for Antibiotic Detection

### 3.1 Introduction

This chapter describes a highly specific and efficient  $Ti_3C_2T_x$  (MXene)-modified molecularly imprinted polymer (MIP) based electrochemical sensor for levofloxacin (an antibiotic) detection (**Fig. 3.1**). The incorporation of  $Ti_3C_2T_x$  with MIP improves the sensitivity of the sensor by offering large surface area and facilitating better electron transfer rate [1, 2]. The fabricated sensor shows high selectivity and a low detection limit for the precise analysis of levofloxacin in two real samples. The details of MXene synthesis, along with MIP sensor fabrication, characterization, optimization, and electrochemical sensing results, are discussed in the following sections.

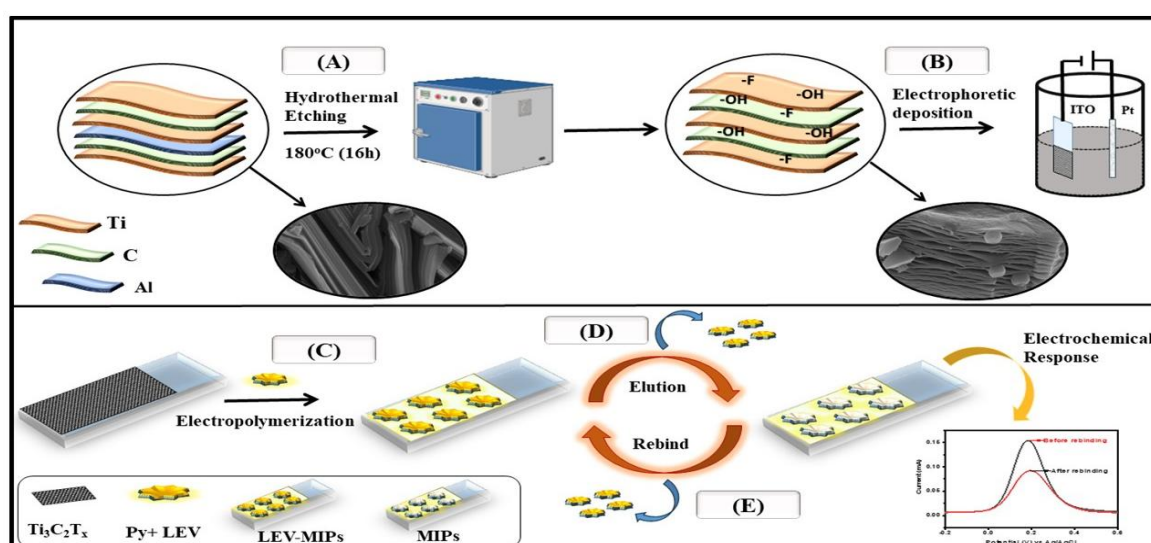


**Fig. 3.1** Schematic representation for the fabrication of  $Ti_3C_2T_x$ -based MIP sensor

## **3.2 Experimental Details**

### **3.2.1 Synthesis of $Ti_3C_2T_x$**

The synthesis of  $Ti_3C_2T_x$  with little modification [3] was carried out by using the hydrothermal method. Initially, 1g of LiF was mixed with 20 mL of 6 M HCl with constant stirring for a duration of 30 min. Thereafter, 1g of  $Ti_3AlC_2$  (MAX Phase) was gradually added to the above solution at room temperature and stirred constantly for another 30 min. Afterwards, the mixture was transferred to a 100 mL Teflon-lined stainless autoclave and heated in an oven at 180°C for 16 h. Further, the precipitate was collected by successfully washing with deionised water and centrifugation at 3500 rpm, followed by vacuum drying for 12 h at 60°C.

### **3.2.2 Electrophoretic Deposition of $Ti_3C_2T_x$ on ITO**

For the deposition process, a colloidal suspension of  $Ti_3C_2T_x$  (0.5 mg) was prepared by ultrasonically dispersing it in 15 mL of DI water. For EPD, the Pt wire served as a counter electrode and was kept 1 cm away from the working electrode (ITO glass substrate). To perform the electrophoretic deposition of  $Ti_3C_2T_x$  onto a pre-hydrolyzed ITO glass surface, different voltages were applied. It was revealed that a smooth film of  $Ti_3C_2T_x$  on the ITO substrate was produced when a 10 V DC potential was applied for 8 sec.

### **3.2.3 Fabrication of MIP-Based Electrochemical Sensor**

To construct the MIP sensor, the  $Ti_3C_2T_x$ /ITO was submerged in an electropolymerization solution of 0.1 M phosphate buffer solution (pH 7) containing 0.4 mM LEV (template molecules) and 2 mM pyrrole (functional monomer). After that, the MIP layer was electropolymerized on top of  $Ti_3C_2T_x$ /ITO using the CV technique with a potential window ranging from 0.6 to 1.6 V with ten scan segments at 50 mV/s of scan rate. Upon completion of electropolymerization, the fabricated  $Ti_3C_2T_x$ /ITO@MIP electrode was placed in a mixture

solution of 0.2 M NaOH/C<sub>2</sub>H<sub>5</sub>OH of ratio 1:1 v/v while stirring (20 min) to extract the LEV (template molecules), followed by washing with DI water and drying.

### 3.3 Results and Discussion

#### 3.3.1 Structural and Morphological Studies

**Fig. 3.2A** displays the XRD pattern of Ti<sub>3</sub>AlC<sub>2</sub> (black curve) and Ti<sub>3</sub>C<sub>2</sub>T<sub>x</sub> (red curve). The distinct peaks of Ti<sub>3</sub>AlC<sub>2</sub> were observed at  $2\theta = 9.5^\circ, 34.1^\circ, 39.0^\circ, 41.9^\circ, 48.5^\circ, 56.4^\circ, 60.3^\circ$  and  $65.3^\circ$ . The characteristic peak of Ti<sub>3</sub>AlC<sub>2</sub> at  $2\theta = 9.5^\circ$  significantly shifts towards the lower angle of  $6.1^\circ$  for Ti<sub>3</sub>C<sub>2</sub>T<sub>x</sub> after the etching process, which indicates the enlarged interlayer spacing of Ti<sub>3</sub>C<sub>2</sub>T<sub>x</sub> (13.9 Å) than that of Ti<sub>3</sub>AlC<sub>2</sub> (9.2 Å) [4]. Furthermore, the disappearance of the peak at  $2\theta = 39.0^\circ$  in the spectra of Ti<sub>3</sub>C<sub>2</sub>T<sub>x</sub> signifies the complete removal of the Al layer, confirming the successful synthesis of Ti<sub>3</sub>C<sub>2</sub>T<sub>x</sub> sheets.

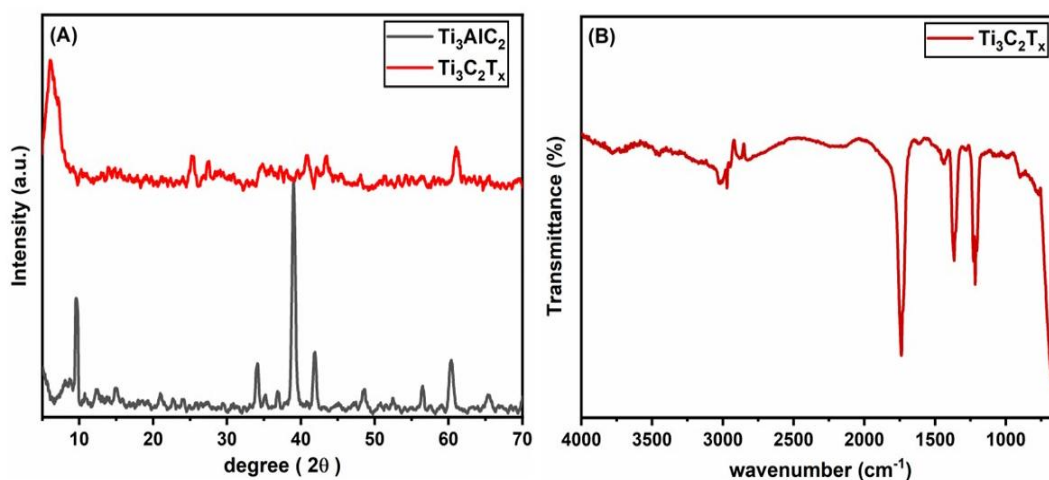


**Fig. 3.2** (A) XRD pattern of Ti<sub>3</sub>AlC<sub>2</sub> (black curve) and Ti<sub>3</sub>C<sub>2</sub>T<sub>x</sub> (red curve) (B) FTIR spectra of Ti<sub>3</sub>C<sub>2</sub>T<sub>x</sub>

The chemical structure of the synthesized Ti<sub>3</sub>C<sub>2</sub>T<sub>x</sub> has been examined using the FTIR spectroscopy. The peak observed at 670 cm<sup>-1</sup> corresponds to the stretching Ti–O bond vibration while the peaks at 1215, 1360 and 1740 cm<sup>-1</sup> are responsible for the stretching vibration of C–F, O–H and C=O bond, respectively [5] as shown in **Fig. 3.2B**.

The surface morphological behaviour and elemental composition of  $Ti_3AlC_2$ ,  $Ti_3C_2T_x$  and polymerized electrodes ( $Ti_3C_2T_x/ITO@MIP$  before elution and  $Ti_3C_2T_x/ITO@MIP$  after elution) were analyzed using FESEM and EDX techniques. As shown in **Fig. 3.3A**, the morphology of  $Ti_3AlC_2$  shows a dense-packed layered structure, while after hydrothermal etching, the SEM image of  $Ti_3C_2T_x$  exhibits a 2D-layered accordion-like structure (**Fig. 3.3B**) [6]. In comparison to  $Ti_3C_2T_x/ITO@MIP$  before elution (**Fig. 3.3C**), the morphology of  $Ti_3C_2T_x/ITO@MIP$  after elution (**Fig. 3.3D**) exhibits a rougher structure, suggesting the complete extraction of template molecules from the MIP film [7]. The EDX spectra of  $Ti_3AlC_2$  and  $Ti_3C_2T_x$  are shown in **Figs. 3.3E** and **3.3F**, respectively. In the EDX spectra of  $Ti_3C_2T_x$ , the absence of Al and the presence of Ti, C, O and F confirm the synthesis of MXene.

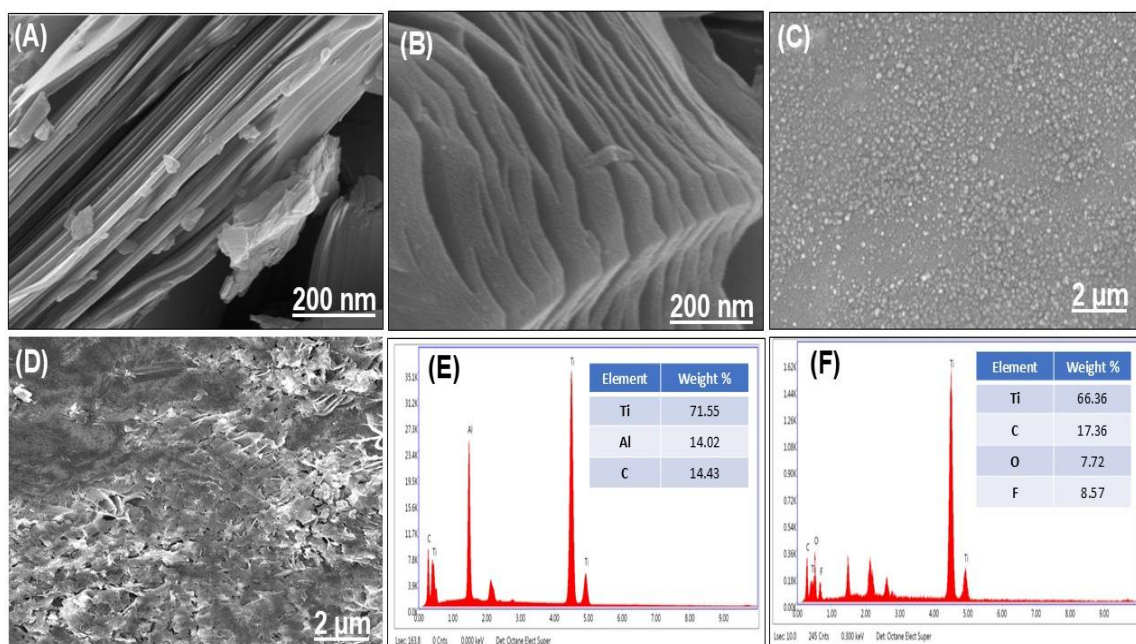


**Fig. 3.3** FESEM micrographs of (A)  $Ti_3AlC_2$  (B)  $Ti_3C_2T_x$  (C)  $Ti_3C_2T_x/ITO@MIP$  before elution (D)  $Ti_3C_2T_x/ITO@MIP$  after elution; EDX analysis of (E)  $Ti_3AlC_2$  and (F)  $Ti_3C_2T_x$

### 3.3.2 Electrochemical Characterization

Cyclic voltammetry (CV) was used to electrochemically analyze the behaviour of each modified electrode in a mixture solution of PBS (0.1 M) containing 5mM  $[\text{Fe}(\text{CN})_6]^{3-/4-}$  and NaCl (0.9%). As depicted in **Fig. 3.4A**, compared to bare ITO (0.28 mA, curve **a**), the  $\text{Ti}_3\text{C}_2\text{T}_x$  modified electrode exhibits a high redox peak current (0.56 mA, curve **b**) because of its large surface area and superior conductivity of  $\text{Ti}_3\text{C}_2\text{T}_x$  that can speed up the electron transfer. The redox peak current disappears following electropolymerization (curve **c**) because of the non-conductive MIP film, which prevents electron transmission. After elution of the template molecules, the redox peak current significantly increased (0.41 mA, curve **d**). This could be due to the resulting imprinted cavities, which served as a channel for the passage of electrons within the MIP matrix. Further, after rebinding LEV molecules, the redox peak current drops to 0.32 mA as seen in curve **e**. This may be because of the LEV molecules, which obstruct certain imprinted cavities, preventing electron flow to the electrode surface. However, due to the insufficient imprinted cavities, the  $\text{Ti}_3\text{C}_2\text{T}_x/\text{ITO}@\text{NIP}$  electrode shows no appreciable change in response current following elution (0.15 mA, curve **f**).

**Fig. 3.4B** displays the CV scan rate (10 to 300 mV/s) study of the  $\text{Ti}_3\text{C}_2\text{T}_x/\text{ITO}@\text{MIP}$  electrode. It is clearly evident from the figure that the oxidation peak shifts towards more positive values while the reduction peak shifts towards more negative values with an increase in the scan rate. The plot between the redox peak potentials ( $E_{\text{pa}}$  and  $E_{\text{pc}}$ ) and the log (scan rate) deduces a linear relationship (**Fig. 3.4C**) and follows **Eqs. 3.1 and 3.2**.

$$E_{\text{pa}} [\text{Ti}_3\text{C}_2\text{T}_x/\text{ITO}@\text{MIP}] = 0.182 \text{ (V)} + 0.087 \text{ (V)} * \log [v \text{ (mV/s)}]; R^2 = 0.982 \quad (3.1)$$

$$E_{\text{pc}} [\text{Ti}_3\text{C}_2\text{T}_x/\text{ITO}@\text{MIP}] = 0.225 \text{ (V)} - 0.087 \text{ (V)} * \log [v \text{ (mV/s)}]; R^2 = 0.989 \quad (3.2)$$

The values of  $\alpha$  and  $K_s$  representing the electron transfer coefficient and charge transfer rate constant for  $\text{Ti}_3\text{C}_2\text{T}_x/\text{ITO}@MIP$  electrode calculated by using Laviron's equation (2.3 to 2.5) are found to be 0.921 and  $0.093 \text{ s}^{-1}$ , respectively.

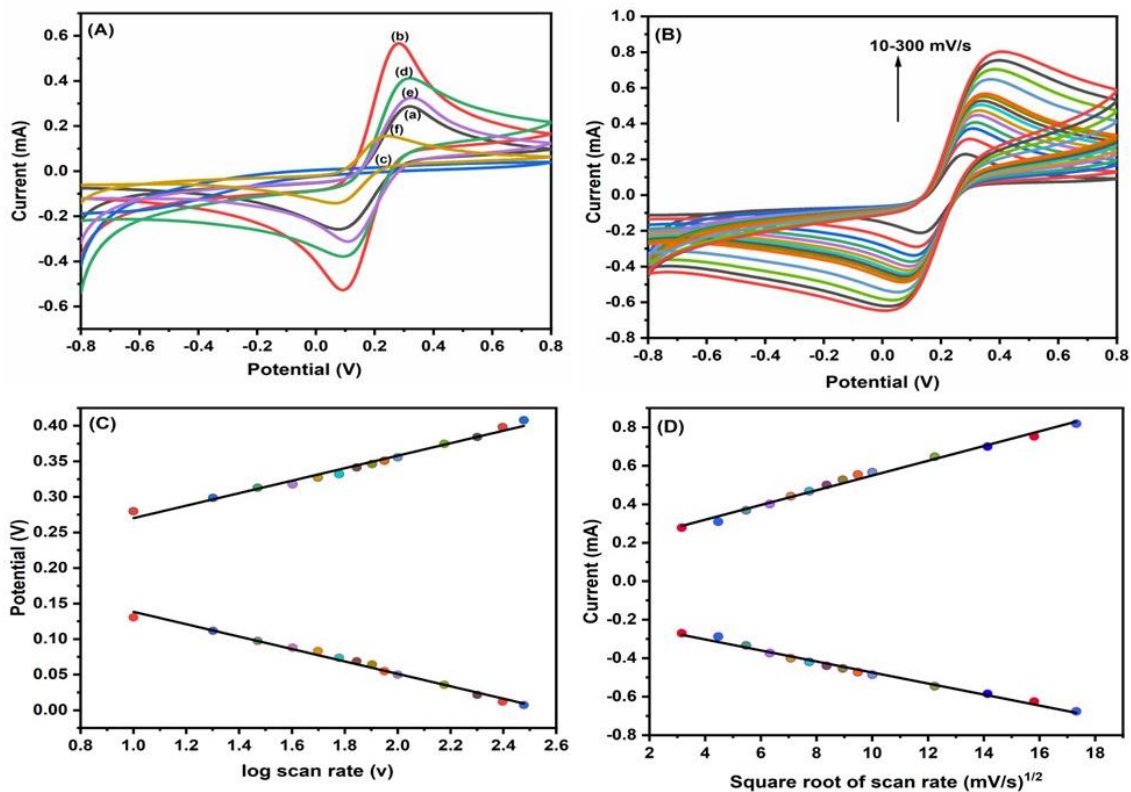


**Fig. 3.4** (A) CV plots of various modified electrodes: (a) ITO (b)  $\text{Ti}_3\text{C}_2\text{T}_x/\text{ITO}$  (c)  $\text{Ti}_3\text{C}_2\text{T}_x/\text{ITO}@MIP$  before elution (d)  $\text{Ti}_3\text{C}_2\text{T}_x/\text{ITO}@MIP$  after elution (e)  $\text{Ti}_3\text{C}_2\text{T}_x/\text{ITO}@MIP$  after rebinding and (f)  $\text{Ti}_3\text{C}_2\text{T}_x/\text{ITO}@NIP$  after elution (B) scan rate studies (10-300 mV/s) (C) linear plot of redox peak potential with log of scan rate and (D) linear curve of peak current vs. square root of scan rate for  $\text{Ti}_3\text{C}_2\text{T}_x/\text{ITO}@MIP$  electrode

Further, the anodic and cathodic peak currents in Fig. 3.4D show a linear trend with square root of corresponding scan rate. Thus, it is confirmed that the electron transport from  $\text{Ti}_3\text{C}_2\text{T}_x/\text{ITO}@MIP$  electrode follows a diffusion-controlled process as described by Eqs. 3.3 and 3.4.

$$I_{pa} [\text{Ti}_3\text{C}_2\text{T}_x/\text{ITO}@MIP] = 166.5 (\mu\text{A}) + 38.3 (\mu\text{A}) (\text{mV/s}) * (\text{mV/s})^{1/2} \text{ v}^{1/2}; R^2 = 0.990 \quad (3.3)$$

$$I_{pc} [\text{Ti}_3\text{C}_2\text{T}_x/\text{ITO}@MIP] = -188.0 (\mu\text{A}) - 28.6 (\mu\text{A}) (\text{mV/s}) * (\text{mV/s})^{1/2} v^{1/2}; R^2 = 0.988 \quad (3.4)$$

The slopes of the above equations (3.3 and 3.4) and the Randles-Sevick equation (Eq. 2.6) are utilized further to calculate the diffusion coefficient (D) and electroactive surface area (A) for the  $\text{Ti}_3\text{C}_2\text{T}_x/\text{ITO}@MIP$  electrode. The D and A values are found to be  $7.45 \times 10^{-6} \text{ cm}^2/\text{s}$  and  $0.22 \text{ cm}^2$ , respectively.

### 3.3.3 Optimization Studies

#### 3.3.3.1 Effect of pH

The structural stability of MIP film may be impacted by the pH of electrolyte solution. Hence, the effect of various pH values between 4.0 to 9.0 was tested on the development of MIP film. It is revealed that the maximum peak response was observed at pH 7, as shown in Fig. 3.5A. This effect occurs because excessively acidic or alkaline conditions can degrade the imprinted film's structural integrity, thereby lowering its sensitivity [8]. Thus, pH 7 is the ideal optimum condition for preparing the MIP film.

#### 3.3.3.2 Effect of template to functional monomer

A template (LEV) to functional monomer (py) ratio is another factor influencing the generation of recognition cavities in polymer matrix during the electropolymerization process. As illustrated in Fig. 3.5B, the peak response increases as the monomer shifts from 1:1 to 1:9 and the maximum current is achieved at 1:5. This is due to the fact that a low concentration of monomer cannot bind enough template molecules while a high concentration of monomer causes self-polymerization which restricts the template-monomer concentration and hinders the electron transfer process. As a result, a 1:5 is set to be the ideal ratio for further experimental studies.

### *3.3.3.3 Effect of electropolymerization scan cycles*

The MIP film's thickness which affects both the number of imprinted cavities and the sensor's sensitivity is determined by the number of scan cycles [9]. As depicted in **Fig. 3.5C**, the current response increases when the number of cycles increases from 4 to 10 due to the creation of more imprinting cavities. However, the current declines after 10 scan cycles as more scan cycles create a thicker MIP film that prevents the elution of template molecules. Hence, 10 scan cycles are ideal for the electropolymerization of MIP film.

### *3.3.3.4 Effect of scan rates*

The scan rate is another crucial parameter for developing the MIP film as it influences the density of MIP film. As shown in **Fig. 3.5D**, the sensor's performance was examined at the scan rates ranging from 30 to 80 mV/s. A maximum peak signal was recorded at 50 mV/s scan rate. It is clear that a low scanning rate raises the density of the MIP film due to the slow binding of template to the functional monomer [10]. However, a high scan rate results in the formation of loose MIP film due to the insufficient interaction between the template and functional monomers. Therefore, 50 mV/s is set to be the optimum scan rate.

### *3.3.3.5 Effect of elution time*

Elution time is another parameter for the sensor's optimal performance. As illustrated in **Fig. 3.5E**, the peak signal rises steadily as the elution time increases from 5 to 20 min, reaching its maximum at 20 min. This suggests that the maximum template molecules were extracted from the polymer matrix leading to the development of corresponding cavities. However, after 20 min, the current significantly drops as prolonged elution time damages the MIP film's surface. Hence, the optimal elution time for an effective elution of template molecules was chosen to be 20 min for further studies.

## 3.3.3.6 Effect of incubation time

The binding of LEV to MIP sites is also influenced by the incubation time. **Fig. 3.5F** shows that the current response decreases with an increase in incubation time and stabilizes after 10 min of adsorption indicating rebinding of LEV moieties to the generated imprinted cavities on fabricated electrode surface. This saturation represents the sensor's equilibrium binding capacity. Thus, 10 min was selected as the optimum incubation time.

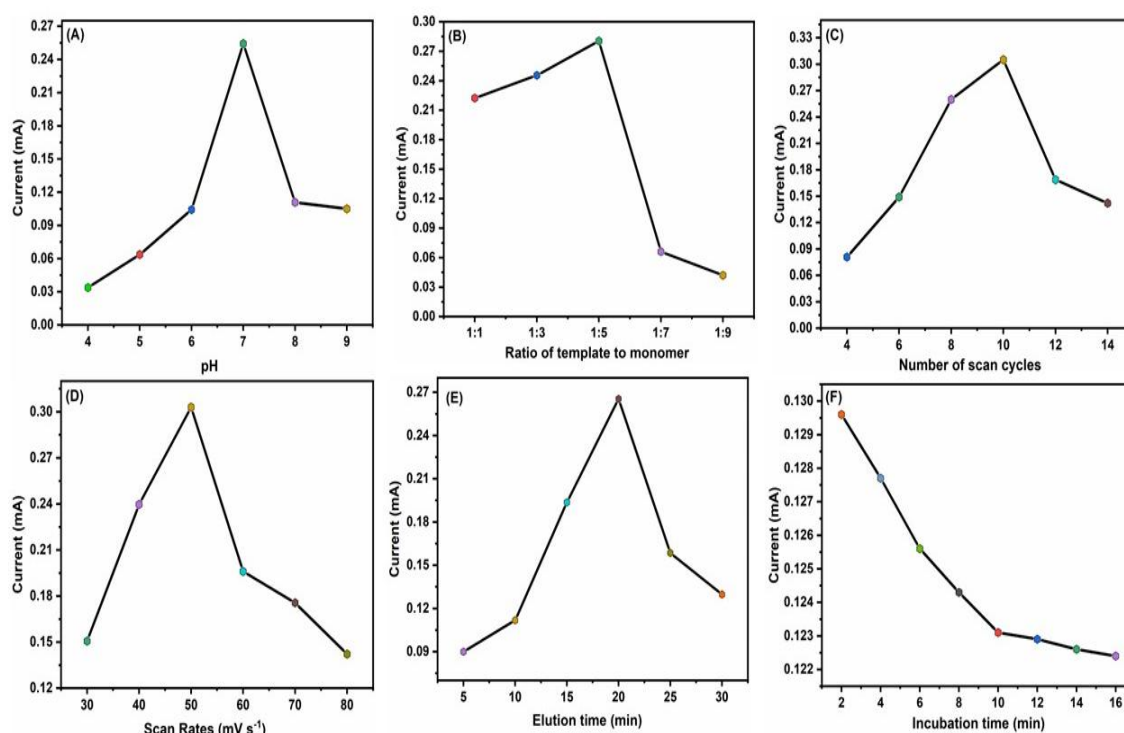


**Fig. 3.5** Optimization key parameters for (A) electropolymerization solution pH (B) template to functional monomer (LEV: Pyrrole) concentration ratio (C) number of scan cycles (D) scan rate (E) elution time and (F) adsorption time of  $\text{Ti}_3\text{C}_2\text{T}_x/\text{ITO}@MIP$  for LEV

## 3.3.4 Performance of MIP Sensor for LEV Detection

The electrochemical behaviour of the fabricated  $\text{Ti}_3\text{C}_2\text{T}_x/\text{ITO}@MIP$  electrode has been used to detect LEV using the DPV technique. As seen in **Fig. 3.6A**, an anodic peak current decreases continuously when the  $\text{Ti}_3\text{C}_2\text{T}_x/\text{ITO}@MIP$  electrode was subjected to higher

concentrations of LEV (1 pM-100 nM). This decline in peak current is observed when LEV molecules block the imprinted sites, thereby obstructing the flow of the redox probe from the electrolytic solution to the MIP electrode surface.

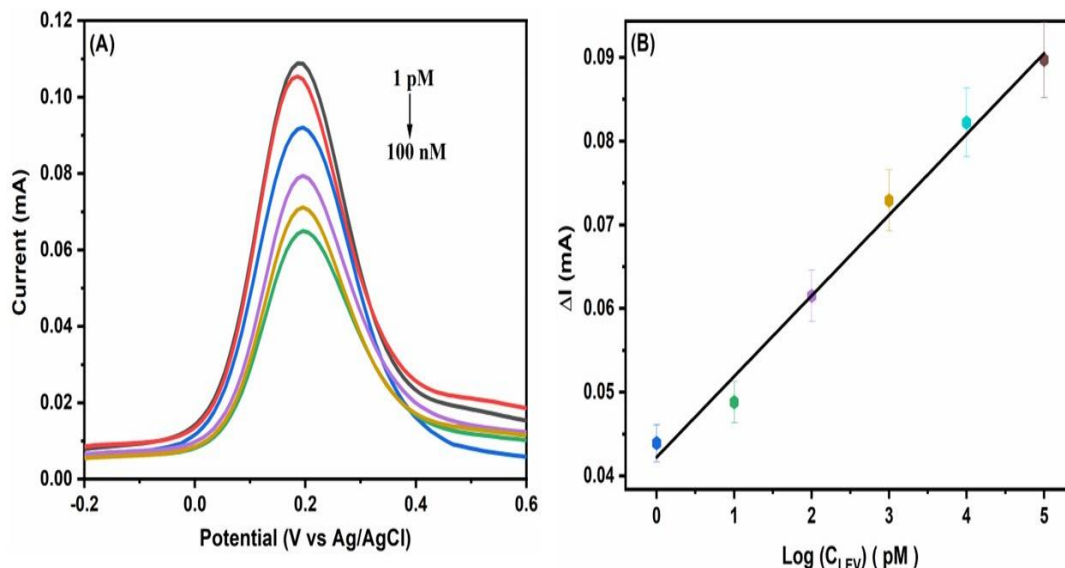


**Fig. 3.6** (A) DPV response study of  $\text{Ti}_3\text{C}_2\text{T}_x/\text{ITO}@MIP$  electrode after incubation at various concentrations (1 pM-100 nM; top to bottom) of LEV and (B) Plot depicting the linearity between  $\Delta I$  and  $\log(C_{LEV})$

A calibration plot between  $\Delta I$  with respect to the logarithm of LEV concentration depicts a linear behaviour (**Fig. 3.6B**) and follows the following regression equation:

$$\text{Current } (\mu\text{A}) = 42.23 \mu\text{A} + 9.649 \mu\text{A pM}^{-1} \times \log C_{LEV}; R^2 = 0.979$$

The detection limit (**Eq. 2.10**) and the sensitivity (**Eq. 2.11**) of the fabricated  $\text{Ti}_3\text{C}_2\text{T}_x/\text{ITO}@MIP$  electrode were calculated to be 0.76 pM and  $40.20 \mu\text{A pM}^{-1} \text{cm}^{-2}$ , respectively. As observed, the fabricated MIP sensor provides an efficient platform for detecting the low concentrations of LEV.

### 3.3.5 Selectivity, Reproducibility, and Stability Studies

The selectivity of the fabricated MIP sensor was examined in the presence of other interfering substances including antibiotics (NOR, CIP and OME) as well as organic and inorganic salts (GLU,  $\text{Na}^+$  and  $\text{CO}_3^{2-}$ ). **Fig. 3.7A** clearly shows that even with a 10 times

higher concentration of these interfering analytes (10 nM) than LEV (1 nM), the fabricated MIP sensor demonstrates a negligible change in peak current confirming its high selectivity towards LEV. Moreover, to examine the specificity, the MIP sensor was tested with a mixture of the aforementioned interfering analytes containing LEV and it exhibits a positive response for detecting LEV. This indicates that the developed MIP sensor is highly specific for detecting LEV.

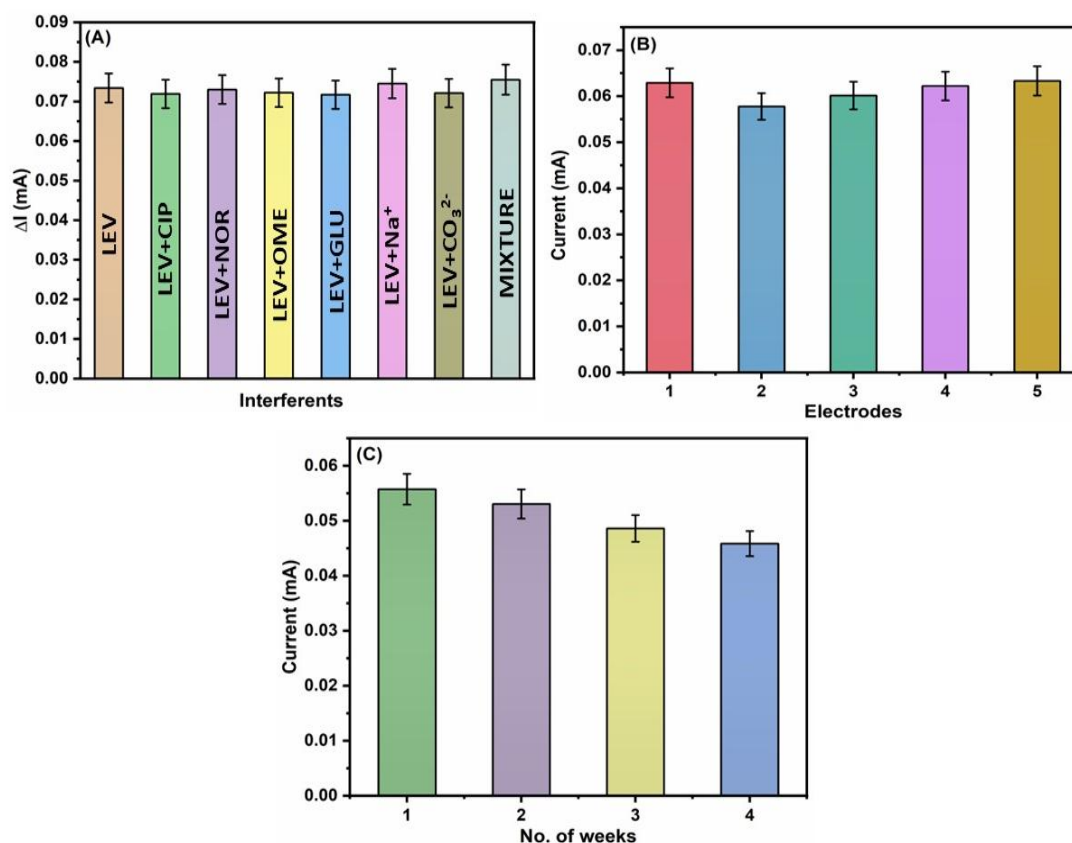


**Fig. 3.7** (A) Interference study of  $Ti_3C_2T_x/ITO@MIP$  electrode in the presence of other interfering species (10 nM) with respect to LEV (1 nM) (B) Reproducibility of the fabricated  $Ti_3C_2T_x/ITO@MIP$  sensor and (C) Stability of  $Ti_3C_2T_x/ITO@MIP$  sensor

Five independent MIP electrodes were constructed under the optimized conditions to check the reproducibility of the fabricated  $Ti_3C_2T_x/ITO@MIP$  electrode for LEV detection and shown in **Fig. 3.7B**. Our results show an RSD of 3.75% with respect to 10 nM LEV indicating a good reproducibility of fabricated MIP electrode. Furthermore, the stability of

developed sensor was evaluated by exposing it to 10 nM LEV weekly over a four-week period (**Fig. 3.7C**). The DPV current shows that the sensor retained 75.4% of its initial value after four weeks, confirming its acceptable stability.

### 3.3.6 Real Sample Analysis

The practicability of the proposed  $Ti_3C_2T_x/ITO@MIP$  sensor for determining LEV was evaluated using two real samples: tap water and a soil sample. Different concentrations of LEV (0.1, 1 and 10 nM) were spiked to diluted real samples, and the DPV response was measured. The results show a good recovery range of 93.6% to 104.5% of LEV for spiked real samples with an RSD value < 5% and the data are presented in **Table 3.1**. This suggests that the fabricated sensor has satisfactory accuracy for the electrochemical detection of antibiotics in real samples.

**Table 3.1:** Detection of LEV in spiked real samples using  $Ti_3C_2T_x/ITO@MIP$  electrode

Sample	Added (nM)	$Ti_3C_2T_x/ITO@MIP$		
		Found (nM)	Recovery (%)	RSD (%)
Soil	0	0	-	-
	0.1	0.093	93.6	4.65
	1	0.949	94.9	3.69
	10	9.69	96.9	2.19
Tap water	0	0	-	-
	0.1	0.096	96.1	2.78
	1	1.04	104.5	3.11
	10	9.36	93.6	4.61

### **3.4 Conclusion**

In this chapter, a rapid and highly sensitive electrochemical sensing platform integrated with a molecular imprinted polymer approach using  $\text{Ti}_3\text{C}_2\text{T}_x$  has been successfully constructed for the detection of LEV. This MIP sensor exhibits excellent electrochemical response with a high sensitivity ( $40.20 \mu\text{A pM}^{-1} \text{cm}^{-2}$ ), dynamic linear detection range from 1 pM-100 nM and low detection limit (0.76 pM) due to a large specific area and good electrical conductivity of  $\text{Ti}_3\text{C}_2\text{T}_x$ . Additionally, the practicability of the proposed MIP sensor was successfully validated for detecting the LEV in spiked real samples.

*The results of the present study have been published in “Journal of Materials Science”  
59, 21684-21695 (2024)*

**References**

1. X. Ma, X. Tu, F. Gao, Y. Xie, X. Huang, C. Fernandez, F. Qu, G. Liu, L. Lu, and Y. Yu, Hierarchical porous MXene/amino carbon nanotubes-based molecular imprinting sensor for highly sensitive and selective sensing of fisetin, *Sensors and Actuators B: Chemical*, 309 (2020) 127815.
2. B. Zhang, Q. Chen, D. Liu, F. Fang, M. Mu, Y. Xie, Y. Kuang, J. Wang, and G. Fang, Heterogeneous sensitization from nanoporous gold and titanium carbide (MXene) combining with molecularly imprinted polymers for highly sensitive and specific sensing detection of thiabendazole, *Sensors and Actuators B: Chemical*, 367 (2022) 132159.
3. C. Peng, P. Wei, X. Chen, Y. Zhang, F. Zhu, Y. Cao, H. Wang, H. Yu, and F. Peng, A hydrothermal etching route to synthesis of 2D MXene ( $\text{Ti}_3\text{C}_2$ ,  $\text{Nb}_2\text{C}$ ): Enhanced exfoliation and improved adsorption performance, *Ceramics International*, 44 (2018) 18886-18893.
4. Liu, Z., R. Guo, F. Li, M. Zheng, B. Wang, T. Li, Y. Luo, and L. Meng, Reduced graphene oxide bridged,  $\text{TiO}_2$  modified and  $\text{Mn}_3\text{O}_4$  intercalated  $\text{Ti}_3\text{C}_2\text{T}_x$  sandwich-like nanocomposite as a high performance anode for enhanced lithium storage applications. *Journal of Alloys and Compounds*, 762 (2018) 643-652.
5. Sweety and D. Kumar, Development of  $\text{Ti}_3\text{C}_2\text{T}_x$ -based novel immunosensor for cancer biomarker detection, *Applied Organometallic Chemistry*, 38 (2024) e7570.
6. F. Wang, Y. Zhu, L. Qian, Y. Yin, Z. Yuan, Y. Dai, T. Zhang, D. Yang, and F. Qiu, Lamellar  $\text{Ti}_3\text{C}_2$  MXene composite decorated with platinum-doped  $\text{MoS}_2$  nanosheets as electrochemical sensing functional platform for highly sensitive analysis of organophosphorus pesticides, *Food Chemistry*, 459 (2024) 140379.
7. G. Li, J. Wu, X. Qi, X. Wan, Y. Liu, Y. Chen, and L. Xu, Molecularly imprinted polypyrrole film-coated poly (3, 4-ethylenedioxythiophene): polystyrene sulfonate-functionalized black phosphorene for the selective and robust detection of norfloxacin, *Materials Today Chemistry*, 26 (2022) 101043.
8. L. Geng, J. Huang, H. Zhai, Z. Shen, J. Han, Y. Yu, H. Fang, F. Li, X. Sun, and Y. Guo, Molecularly imprinted electrochemical sensor based on multi-walled carbon nanotubes for specific recognition and determination of chloramphenicol in milk, *Microchemical Journal*, 182 (2022) 107887.
9. H. Wang, L. Cai, Y. Wang, C. Liu, G. Fang, and S. Wang, Covalent molecularly imprinted electrochemical sensor modulated by borate ester bonds for hygromycin B detection based on the synergistic signal amplification of Cu-MOF and MXene, *Food Chemistry*, 383 (2022) 132382.
10. H. Lu, M. Liu, H. Cui, Y. Huang, L. Li, and Y. Ding, An advanced molecularly imprinted electrochemical sensor based bifunctional monomers for highly sensitive detection of nitrofurazone, *Electrochimica Acta*, 427 (2022) 140858.

## Titanium Dioxide Anchored MXene-based Molecularly Imprinted Electrochemical Sensor for Antibiotic Detection

### 4.1 Introduction

This study employed the ultrasensitive determination of levofloxacin by using hydrothermally synthesized  $\text{TiO}_2\text{-Ti}_3\text{C}_2\text{T}_x$  modified MIP-based electrochemical sensor (Fig.4.1). Here,  $\text{TiO}_2$  boosts the stability of the MXene in two ways: (i) by acting as a barrier to prevent the inner structure of  $\text{Ti}_3\text{C}_2\text{T}_x$  from oxidative deterioration and (ii) by widening the interlayer spacing between the MXene sheets to prevent the aggregation [1, 2]. Thus, the synergistic effect of the  $\text{TiO}_2\text{-Ti}_3\text{C}_2\text{T}_x$  composite results in remarkable electrical conductivity, a large specific area and good electrocatalytic activity towards levofloxacin oxidation, and it has been successfully utilised for real sample analysis.

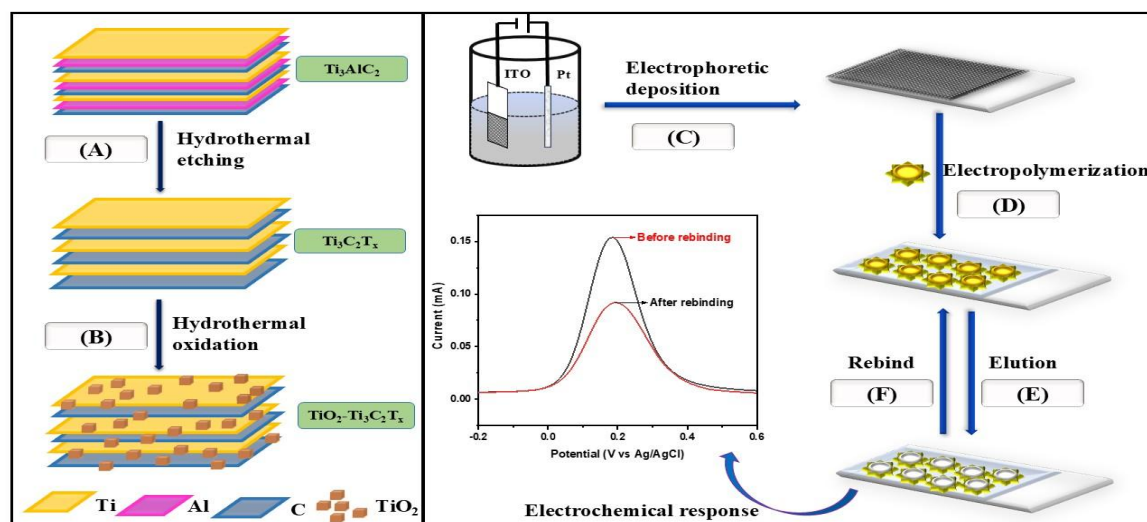


**Fig. 4.1** Diagrammatic illustration showing the fabrication of  $\text{TiO}_2\text{-Ti}_3\text{C}_2\text{T}_x$ -based MIP electrochemical sensor

## **4.2 Experimental Details**

### **4.2.1 Synthesis of $\text{Ti}_3\text{C}_2\text{T}_x$ and $\text{TiO}_2\text{-Ti}_3\text{C}_2\text{T}_x$**

Synthesis process used for the preparation of  $\text{Ti}_3\text{C}_2\text{T}_x$  has been discussed in chapter 3. To prepare the  $\text{TiO}_2\text{-Ti}_3\text{C}_2\text{T}_x$  composite, the synthesized  $\text{Ti}_3\text{C}_2\text{T}_x$  (80 mg) and  $\text{NaBF}_4$  (220 mg) were dissolved in 0.1 M HCl (20 mL) with constant stirring for 1 h. Then, the solution was placed in a Teflon-lined autoclave for hydrothermal treatment at a temperature of  $180^\circ\text{C}$  for 8 h. After that, the solution was cooled down at room temperature and the resulting grey material was centrifuged and then washed with a DI water/ethanol mixture and finally vacuum-dried at  $60^\circ\text{C}$  [3].

### **4.2.2 Electrophoretic Deposition of $\text{TiO}_2\text{-Ti}_3\text{C}_2\text{T}_x$**

The electrophoretic deposition technique was employed to deposit the prepared composite material onto a pre-hydrolyzed ITO coated glass substrate. Prior to the deposition process, a colloidal solution of  $\text{TiO}_2\text{-Ti}_3\text{C}_2\text{T}_x$  (0.8 mg) was prepared through ultrasonication in DI water (15 mL). After optimizing several potentials, a smooth and uniform film of the composite was formed after 10 sec at a DC potential of 10 V.

### **4.2.3 Fabrication of $\text{TiO}_2\text{-Ti}_3\text{C}_2\text{T}_x$ Modified MIP-based Electrochemical Sensing Platform**

Initially, the  $\text{TiO}_2\text{-Ti}_3\text{C}_2\text{T}_x$  modified ITO was submerged in a phosphate buffer solution (0.1 M) of pH 7 containing template molecules (LEV, 0.4 mM) and functional monomer (pyrrole, 1.6 mM). Afterwards, the MIP film was deposited onto the  $\text{TiO}_2\text{-Ti}_3\text{C}_2\text{T}_x/\text{ITO}$  via cyclic voltammetry with a potential range of 0.6 to 1.6 V at a scanning rate of 75 mV/s for 8 scan cycles to create  $\text{TiO}_2\text{-Ti}_3\text{C}_2\text{T}_x/\text{ITO}@\text{MIP}$ . After electropolymerization, the MIP electrode was immersed in a desorption solution of 0.2 M sodium hydroxide and an ethanol solution for 25 min and stirred it to elute the embedded LEV molecules from the MIP layer.

Finally, the fabricated electrode was washed with DI water and finally dried at room temperature. A non-imprinted electrode ( $\text{TiO}_2\text{-Ti}_3\text{C}_2\text{T}_x/\text{ITO}@NIP$ ) was developed as a control using the same approach but without the addition of template molecules during the electropolymerization process.

## 4.3 Results and Discussion

### 4.3.1 Structural Studies

**Fig. 4.2A** depicts the XRD pattern of  $\text{Ti}_3\text{AlC}_2$  (black),  $\text{Ti}_3\text{C}_2\text{T}_x$  (red) and  $\text{TiO}_2\text{-Ti}_3\text{C}_2\text{T}_x$  (blue). After hydrothermal etching, the diffraction peak of  $\text{Ti}_3\text{AlC}_2$  at  $2\theta=39.1^\circ$  disappeared from the spectra of  $\text{Ti}_3\text{C}_2\text{T}_x$  suggesting the structural destruction of the  $\text{Ti}_3\text{AlC}_2$  and a complete removal of Al layer to form the MXene. Besides, a significant shift of the peak at  $2\theta=9.4^\circ$  ( $\text{Ti}_3\text{AlC}_2$ ) towards a lower angle of  $6.4^\circ$  for  $\text{Ti}_3\text{C}_2\text{T}_x$  and  $6.1^\circ$  for  $\text{TiO}_2\text{-Ti}_3\text{C}_2\text{T}_x$ , indicating the increase in the interlayer spacing of  $\text{Ti}_3\text{C}_2\text{T}_x$  and  $\text{TiO}_2\text{-Ti}_3\text{C}_2\text{T}_x$ . The interlayer spacing of  $\text{Ti}_3\text{AlC}_2$ ,  $\text{Ti}_3\text{C}_2\text{T}_x$  and  $\text{TiO}_2\text{-Ti}_3\text{C}_2\text{T}_x$  was calculated using  $2d \sin \theta = n\lambda$  and found to be 9.7 Å, 13.7 Å and 14.4 Å, respectively. Moreover, the peaks located for  $\text{TiO}_2\text{-Ti}_3\text{C}_2\text{T}_x$  at  $2\theta= 25.3^\circ, 37.7^\circ, 48.0^\circ, 54.1^\circ, 55.0^\circ, 62.6^\circ, 68.9^\circ, 70.1^\circ$  and  $75.0^\circ$  represents the anatase form of  $\text{TiO}_2$  [4].

**Fig. 4.2B** shows the FTIR spectra of  $\text{Ti}_3\text{C}_2\text{T}_x$  (black) and  $\text{TiO}_2\text{-Ti}_3\text{C}_2\text{T}_x$  (red). The two vibrational bands at 2974 and 2859  $\text{cm}^{-1}$  for  $\text{Ti}_3\text{C}_2\text{T}_x$  and  $\text{TiO}_2\text{-Ti}_3\text{C}_2\text{T}_x$  correspond to the C–H bond stretching vibration while the functional groups present on  $\text{Ti}_3\text{C}_2\text{T}_x$  surface were confirmed by the characteristic bands occurring at 1608, 1394 and 1054  $\text{cm}^{-1}$  which denotes the stretching vibrations of C=O, O–H and C–F bonds, respectively. Additionally, a band occurring within 400-800  $\text{cm}^{-1}$  range is attributed to the stretching vibration of the Ti–O bond ( $\text{TiO}_2\text{-Ti}_3\text{C}_2\text{T}_x$ ) [3].

The structural features of the synthesized 2D materials were further characterized by using Raman spectroscopy (**Fig. 4.2C**). In the Raman spectrum of  $\text{Ti}_3\text{C}_2\text{T}_x$  (black curve), the three

characteristic peaks appeared at 207, 392 and 603  $\text{cm}^{-1}$  correspond to the  $-\text{O}$ ,  $-\text{F}$  and  $-\text{OH}$  surface terminal groups on the MXene surface [5]. Additionally, the characteristic D band at 1376  $\text{cm}^{-1}$  and G band at 1584  $\text{cm}^{-1}$  represent the disordered carbon and stretching vibration of  $\text{sp}^2$  hybridized carbon atoms, respectively [6]. The Raman spectrum of  $\text{TiO}_2\text{-Ti}_3\text{C}_2\text{T}_x$  (red curve) shows all the characteristic peaks of  $\text{Ti}_3\text{C}_2\text{T}_x$  along with a prominent peak at 155  $\text{cm}^{-1}$  corresponding to the anatase form of  $\text{TiO}_2$ .

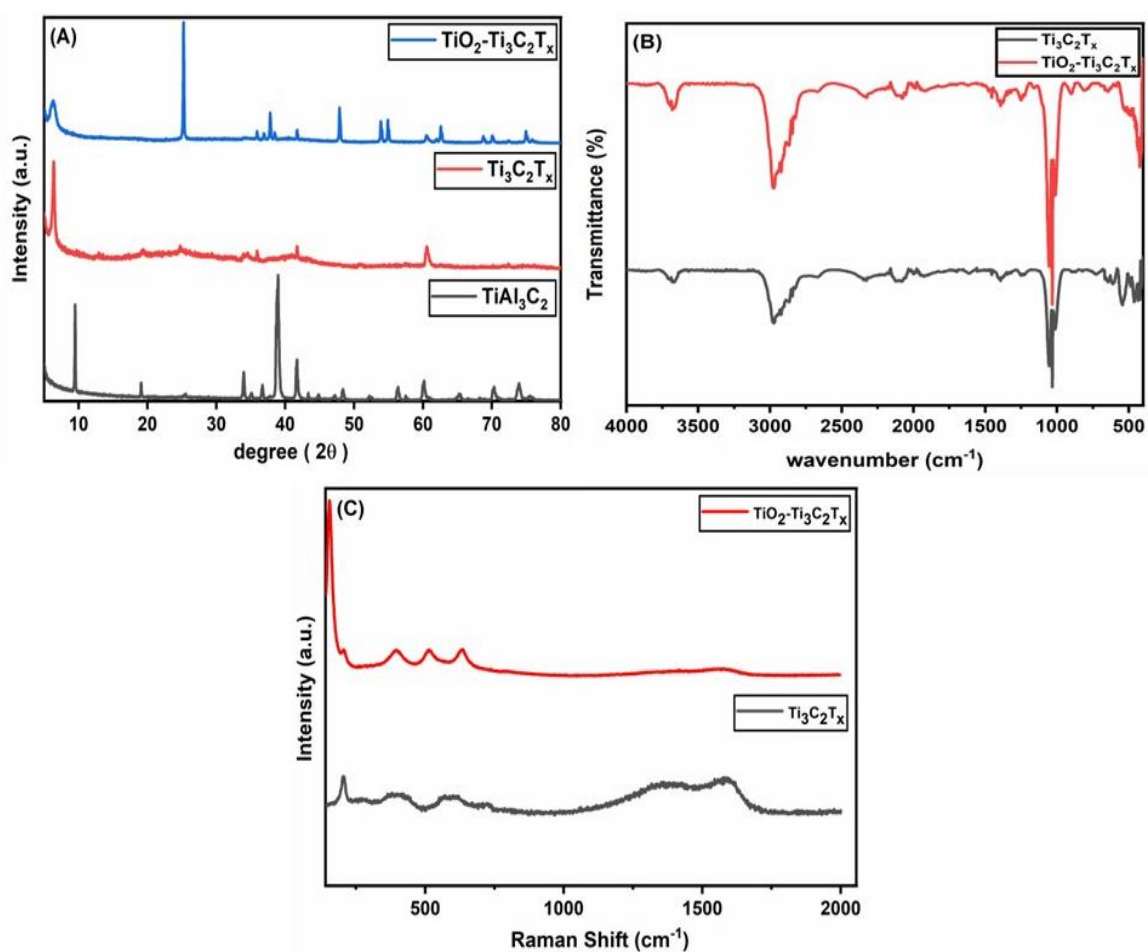


**Fig. 4.2** (A) XRD spectra of  $\text{Ti}_3\text{AlC}_2$  (black),  $\text{Ti}_3\text{C}_2\text{T}_x$  (red),  $\text{TiO}_2\text{-Ti}_3\text{C}_2\text{T}_x$  (blue) (B) FTIR and (C) Raman spectra of  $\text{Ti}_3\text{C}_2\text{T}_x$  (black) and  $\text{TiO}_2\text{-Ti}_3\text{C}_2\text{T}_x$  (red)

### 4.3.2 Morphological Studies

FESEM and EDX techniques were employed to examine the surface morphologies of the prepared 2D materials and polymerized electrodes ( $\text{TiO}_2\text{-Ti}_3\text{C}_2\text{T}_x/\text{ITO}@MIP$  before elution

and  $\text{TiO}_2\text{-Ti}_3\text{C}_2\text{T}_x/\text{ITO@MIP}$  after elution) as shown in **Fig. 4.3**. Before etching, the FESEM image of  $\text{Ti}_3\text{AlC}_2$  shows a packed layered structure (**Fig. 4.3A**), whereas after etching, the  $\text{Ti}_3\text{C}_2\text{T}_x$  represents the 2D lamellar accordion-like structure as shown in **Fig. 4.3B**. It can be clearly seen in **Fig. 4.3C** that the morphological structure of the composite ( $\text{TiO}_2\text{-Ti}_3\text{C}_2\text{T}_x$ ) depicts a uniformly sized and evenly dispersed 2D- $\text{TiO}_2$  sheet on the layered  $\text{Ti}_3\text{C}_2\text{T}_x$  surface [7]. Prior to template elution, a smooth and uniform MIP layer was seen on the  $\text{TiO}_2\text{-Ti}_3\text{C}_2\text{T}_x/\text{ITO}$  surface (**Fig. 4.3D**). After template elution, the surface of the MIP-modified electrode ( $\text{TiO}_2\text{-Ti}_3\text{C}_2\text{T}_x/\text{ITO@MIP}$ ) becomes rougher suggesting that the cavities are imprinted upon exposure to the template molecules [8] as illustrated in **Fig. 4.3E**. Furthermore, the EDX of the  $\text{TiO}_2\text{-Ti}_3\text{C}_2\text{T}_x$  composite shows the presence of Ti, O, C and F indicating the purity of the synthesized material (**Fig. 4.3F**).

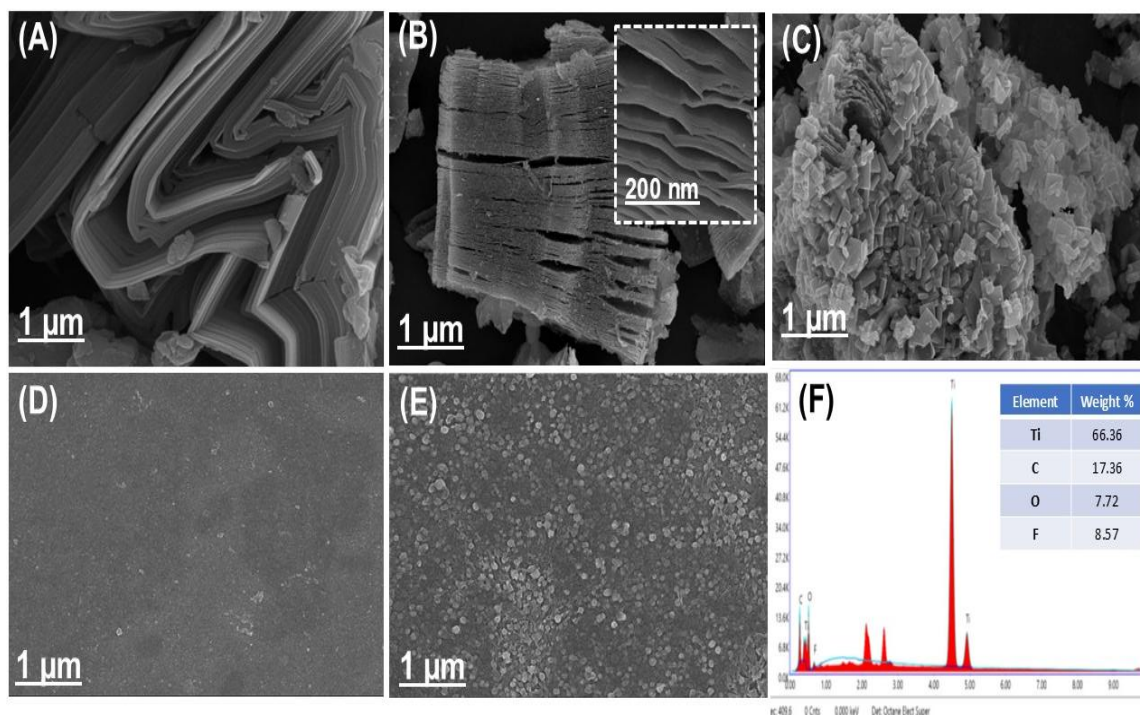


**Fig. 4.3** FESEM images of (A)  $\text{Ti}_3\text{AlC}_2$  (B)  $\text{Ti}_3\text{C}_2\text{T}_x$  (C)  $\text{TiO}_2\text{-Ti}_3\text{C}_2\text{T}_x$  (D)  $\text{TiO}_2\text{-Ti}_3\text{C}_2\text{T}_x/\text{ITO@MIP}$  before elution (E)  $\text{TiO}_2\text{-Ti}_3\text{C}_2\text{T}_x/\text{ITO@MIP}$  after elution and (F) EDX spectra of  $\text{TiO}_2\text{-Ti}_3\text{C}_2\text{T}_x$

### 4.3.3 Electrochemical Studies

To investigate the electrochemical characteristics and interfacial charge kinetics of each modified electrode, cyclic voltammetry (CV) and electrochemical impedance spectroscopy (EIS) measurements were conducted in a mixture of 5mM  $[\text{Fe}(\text{CN})_6]^{3-/4-}$  and NaCl (0.9%).

**Fig.4.4A** shows that the  $\text{TiO}_2\text{-Ti}_3\text{C}_2\text{T}_x/\text{ITO}$  has the maximum peak response (0.75 mA, curve **c**) when compared to bare ITO (0.29 mA, curve **a**) and  $\text{Ti}_3\text{C}_2\text{T}_x/\text{ITO}$  (0.51 mA, curve **b**). This is due to the high conductivity of  $\text{Ti}_3\text{C}_2\text{T}_x$  and the chemical functionalities of  $\text{TiO}_2$ , which may accelerate electron transfer. After electropolymerization of Ppy-LEV at the electrode surface, the redox peak nearly vanishes (curve **d**), which is attributed to the non-conductive nature of the MIP film, which prevents electron transmission. Following the extraction of the bound LEV molecules from the polymer matrix, the redox peak current significantly increased (0.60 mA, curve **e**). This indicates that the formation of imprinted cavities facilitates the conduit for the transmission of electrons within the MIP film. Additionally, the redox peak current drops (0.47 mA, curve **f**), indicating that the LEV molecules are blocking some imprinted sites and impeding electron transfer to the electrode surface. On the other hand, the  $\text{TiO}_2\text{-Ti}_3\text{C}_2\text{T}_x/\text{ITO}@NIP$  electrode did not exhibit a substantial change in peak current upon elution (curve **g**) due to the inadequate imprinted cavity development.

EIS was used to analyze each modified electrode's charge transfer resistance ( $R_{ct}$ ) at a fixed potential of 0.01 V and a frequency range of 0.01 to  $10^5$  Hz. The Nyquist plot in the EIS spectrum consists of a linear part that represents the diffusion-controlled process at lower frequencies and a semicircular part that represents the limited electron transfer mechanism at higher frequencies. As shown in **Fig. 4.4B**, the  $R_{ct}$  of  $\text{TiO}_2\text{-Ti}_3\text{C}_2\text{T}_x/\text{ITO}$  drops to 240  $\Omega$  (curve **c**) in contrast to bare ITO (1560  $\Omega$ , curve **(a)**) and  $\text{Ti}_3\text{C}_2\text{T}_x/\text{ITO}$  (581  $\Omega$ , curve **(b)**). This suggests that the synergistic effect of the synthesized composite enhances the electron

transfer at the electrode/electrolyte interface. When Ppy-LEV film is assembled on  $\text{TiO}_2\text{-Ti}_3\text{C}_2\text{T}_x/\text{ITO}$ , the non-conductive MIP layer inhibits electron transfer causing  $R_{ct}$  to rise sharply to 6370  $\Omega$  (curve **d**). After template elution, the  $R_{ct}$  further drops to 439  $\Omega$  (curve **e**), confirming the formation of imprinted cavities that offer an electron transfer channel between the electrode and electrolyte interface. The  $R_{ct}$  rises to 705  $\Omega$  (curve **f**) after the LEV molecules rebound, suggesting the LEV reduces the electron transfer of redox probe by occupying some cavities. Notably, upon elution, the  $R_{ct}$  value for  $\text{TiO}_2\text{-Ti}_3\text{C}_2\text{T}_x/\text{ITO}@NIP$  electrode was found to be 1650  $\Omega$  (curve **g**) demonstrating the lack of formation of imprinted sites. These results are consistent with the earlier CV findings.

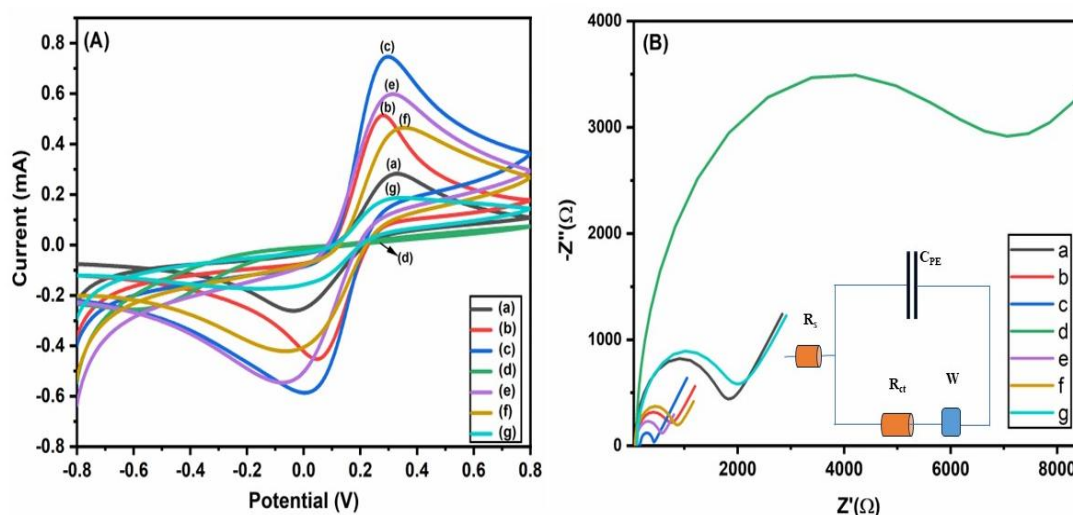


**Fig. 4.4** (A) CV plots and (B) EIS curves of various modified electrodes: (a) ITO (b)  $\text{Ti}_3\text{C}_2\text{T}_x/\text{ITO}$  (c)  $\text{TiO}_2\text{-Ti}_3\text{C}_2\text{T}_x/\text{ITO}$  (d)  $\text{TiO}_2\text{-Ti}_3\text{C}_2\text{T}_x/\text{ITO}@MIP$  before elution (e)  $\text{TiO}_2\text{-Ti}_3\text{C}_2\text{T}_x/\text{ITO}@MIP$  after elution (f)  $\text{TiO}_2\text{-Ti}_3\text{C}_2\text{T}_x/\text{ITO}@MIP$  after rebinding and (g)  $\text{TiO}_2\text{-Ti}_3\text{C}_2\text{T}_x/\text{ITO}@NIP$  after elution

Furthermore, the interfacial kinetics of the  $\text{TiO}_2\text{-Ti}_3\text{C}_2\text{T}_x/\text{ITO}@MIP$  electrode were examined at various scan rates (10-300 mV/s) by using the CV technique (**Fig. 4.5A**). As shown in **Fig. 4.5B**, plotting the redox potentials ( $E_{pa}$  and  $E_{pc}$ ) with the log of scan rate reveals a linear behaviour that corresponds to **Eqs. 4.1 and 4.2**.

$$E_{pa} [\text{TiO}_2\text{-Ti}_3\text{C}_2\text{T}_x/\text{ITO@MIP}] = 0.146 \text{ (V)} + 0.098 \text{ (V)} * \log [v \text{ (mV/s)}]; R^2 = 0.996 \quad (4.1)$$

$$E_{pc} [\text{TiO}_2\text{-Ti}_3\text{C}_2\text{T}_x/\text{ITO@MIP}] = 0.215 \text{ (V)} - 0.164 \text{ (V)} * \log [v \text{ (mV/s)}]; R^2 = 0.995 \quad (4.2)$$

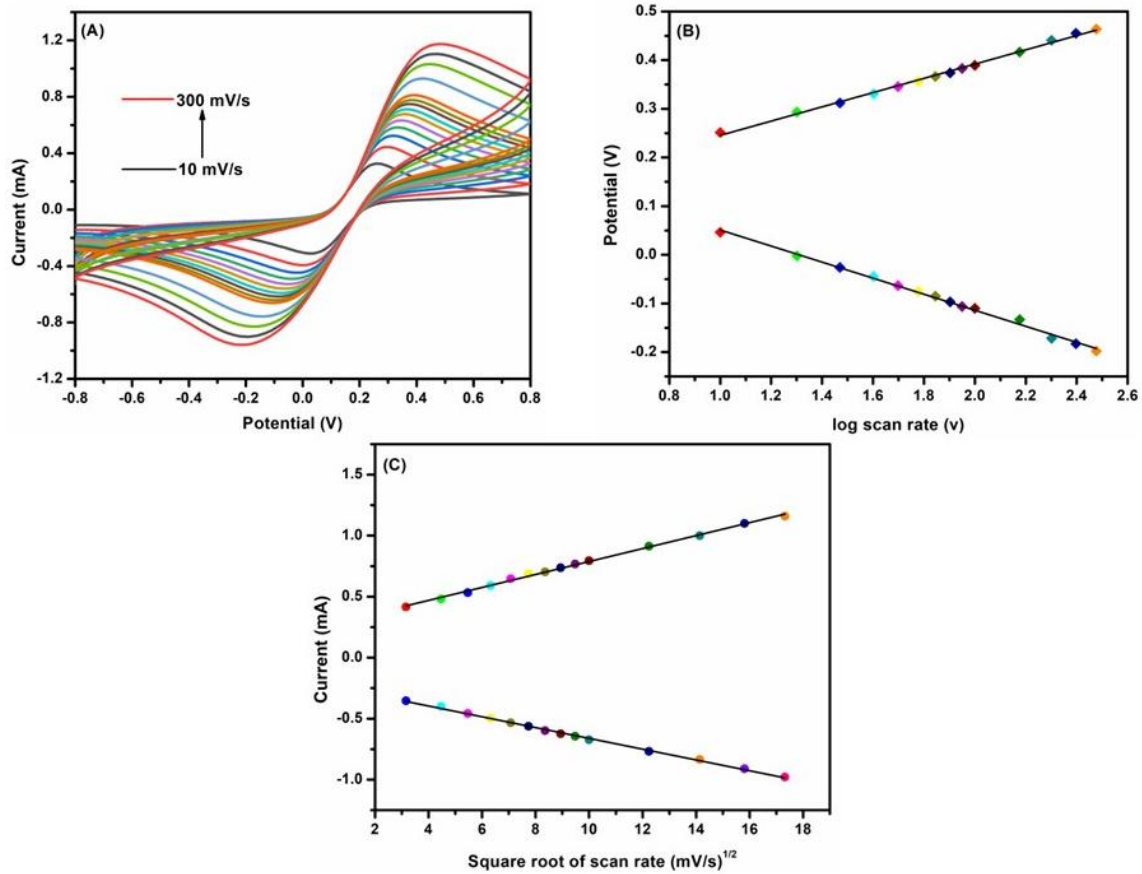


**Fig. 4.5 (A)** CV curves of scan rate studies (10-300 mV/s) **(B)** linear curves of redox peak potential with log of scan rate, and **(C)** linear curves of peak current vs. square root of scan rate for  $\text{TiO}_2\text{-Ti}_3\text{C}_2\text{T}_x/\text{ITO@MIP}$  electrode

Similarly, the peak currents ( $I_{pa}$  and  $I_{pc}$ ) when plotted with respect to the square root of the corresponding scan rate show a linear pattern (**Fig. 4.5C**) and suggests that the electron transfer process is diffusion-controlled and follows Eqs. 4.3 and 4.4.

$$I_{pa} [\text{TiO}_2\text{-Ti}_3\text{C}_2\text{T}_x/\text{ITO@MIP}] = 256.7 \text{ (}\mu\text{A)} + 53.1 \text{ (}\mu\text{A)} (\text{mV/s}) * (\text{mV/s})^{1/2} v^{1/2}; R^2 = 0.997 \quad (4.3)$$

$$I_{pc} [\text{TiO}_2\text{-Ti}_3\text{C}_2\text{T}_x/\text{ITO@MIP}] = -218.9 \text{ (}\mu\text{A)} - 44.2 \text{ (}\mu\text{A)} (\text{mV/s}) * (\text{mV/s})^{1/2} v^{1/2}; R^2 = 0.997 \quad (4.4)$$

Moreover, the quantitative parameters such as the diffusion coefficient ( $D$ ), surface coverage area ( $\tau$ ) and electroactive surface area ( $A$ ) of the developed electrode have been

calculated using the slope of the above equations and the Randles-Sevick equation (Eqs. 2.6 and 2.7). The values of  $D$ ,  $\tau$  and  $A$  are calculated to be  $10.94 \times 10^{-6} \text{ cm}^2/\text{s}$ ,  $3.45 \times 10^{-8} \text{ mol}/\text{cm}^2$  and  $0.24 \text{ cm}^2$ , respectively.

### **4.3.4 Optimization Parameters**

#### *4.3.4.1 Effect of pH of electropolymerization solution*

The pH of electrolyte might affect the MIP film's structural stability. As illustrated in **Fig. 4.6A**, the electrolyte's pH was examined between 4.0 and 9.0 and it was discovered that the maximum current signal was attained at pH 7. The reason for this phenomenon is that an excessively acidic or alkaline environment can weaken the structural integrity of the imprinted film thereby reducing its sensitivity. Therefore, the optimum pH for fabricating the MIP film was determined to be 7.0.

#### *4.3.4.2 Effect of template on functional monomer ratio*

The generation of recognition sites within the polymer matrix is influenced by the variations in template-to-monomer ratio. As seen in **Fig. 4.6B**, the peak response rises as the monomer ratio shifts from 1:1 to 1:4. This is because a higher concentration of monomer produces more recognition cavities for the template molecules. On the other hand, an excessive concentration of monomer causes self-polymerization which limits the template-monomer interactions and impedes the electron transfer process. As a result, 1:4 was determined to be the ideal molar ratio.

#### *4.3.4.3 Effect of scan cycles*

The scan cycle numbers determine its thickness which impacts both the number of imprinted cavities and the sensor's sensitivity. As shown in **Fig. 4.6C**, the maximum peak current was reached during 8 scan cycles. This is due to the fact that more scan cycles result in a thicker MIP film which hinders the elution of the template molecule whereas fewer

scan cycles lead to a thinner membrane resulting in fewer imprinted sites. Therefore, 8 scan cycles were determined to be the optimal conditions.

#### *4.3.4.4 Effect of scan rate*

During the electropolymerization process, the scan rate affects the density of the MIP film. As shown in **Fig. 4.6D**, the sensor's performance was evaluated at different scan rates ranging from 25 to 125 mV/s. According to DPV analysis, the maximum peak current was observed at a scan rate of 75 mV/s. This is due to the fact that at a low scanning rate, the density of the MIP film increases which further inhibits template elution and reduces the number of recognition binding sites. The current decreases when the scanning speed is too high leading to the formation of a loose MIP film due to inadequate interaction between the template molecule and the monomer. Hence, a scan rate of 75 mV/s was selected as the optimal condition.

#### *4.3.4.5 Effect of elution time*

Elution time is a crucial parameter for the sensor's excellent performance. As depicted in **Fig. 4.6E**, the highest response current was achieved at 25 min of elution time suggesting the elution of the template molecules from the polymer matrix. However, a longer elution time damages the structure of the MIP film resulting in a decrease in current response. Thus, 25 min was the ideal elution time for efficient removal of template molecules.

#### *4.3.4.6 Effect of incubation time*

Incubation time is another parameter which influences the LEV binding to the MIP sites. **Fig. 4.6F** demonstrates that the peak current decreases and stabilizes beyond 10 min after adsorption indicating the binding of the LEV moiety to the imprinted cavities. Therefore, 10 min was chosen as the ideal adsorption time.

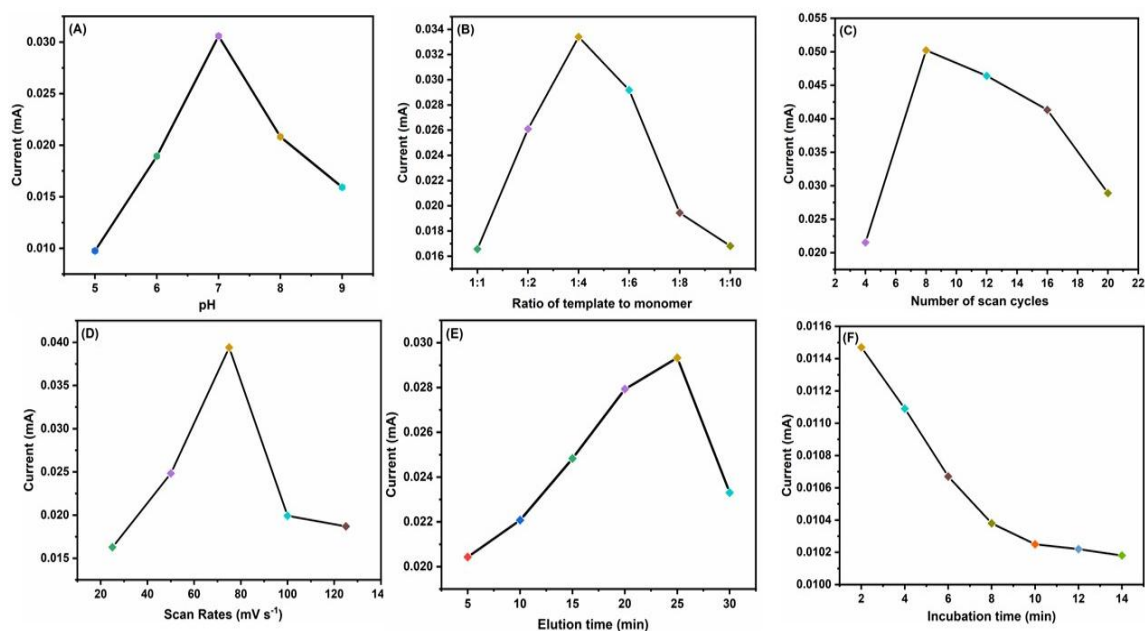


**Fig. 4.6** Optimization key parameters for preparing  $\text{TiO}_2\text{-Ti}_3\text{C}_2\text{T}_x/\text{ITO@MIP}$  electrode: (A) Effect of electrolytic solution pH (B) concentration ratio of template to monomer (C) scan cycles (D) scan rate (E) elution time and (F) incubation time

### 4.3.5 Analytical Performance of $\text{TiO}_2\text{-Ti}_3\text{C}_2\text{T}_x/\text{ITO@MIP}$

Using the DPV method, the electrochemical performance of the  $\text{TiO}_2\text{-Ti}_3\text{C}_2\text{T}_x/\text{ITO@MIP}$  electrode was studied at various LEV concentrations ranging from 1 pM to 100 nM. It is found that the peak current declines continuously with an increase in LEV concentration, as shown in **Fig. 4.7A**. This decline in anodic peak current occurs due to the occupation of the imprinted cavities by the LEV molecules, which hampers the electron transfer process of the redox probe from the electrolytic solution to the electrode surface. **Fig. 4.7B** shows a calibration plot between the inhibition current ( $\Delta I$ ) and the logarithm of LEV concentration ( $C_{\text{LEV}}$ ), which depicts a linear behaviour with the following equation:

$$\text{Current } (\mu\text{A}) = 42.63 \mu\text{A} + 12.73 \mu\text{A pM}^{-1} \times \log C_{\text{LEV}}; R^2 = 0.985$$

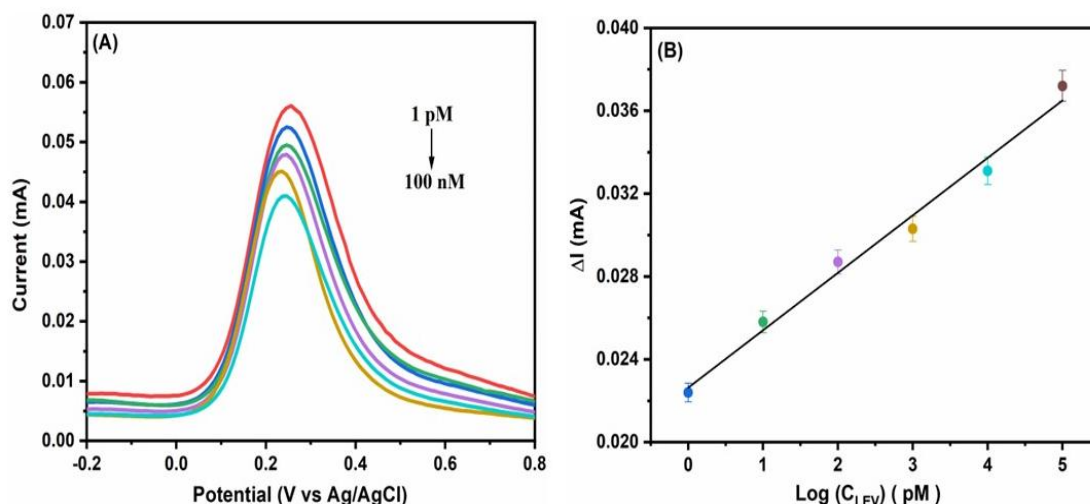


**Fig. 4.7 (A)** DPV response study of fabricated  $\text{TiO}_2\text{-Ti}_3\text{C}_2\text{T}_x/\text{ITO@MIP}$  electrode at various LEV concentrations (1 pM-100 nM) and **(B)** calibration plot depicting a linear behaviour between the  $\Delta I$  and  $\log(C_{\text{LEV}})$

By using the slope of the above calibration plot and  $\text{TiO}_2\text{-Ti}_3\text{C}_2\text{T}_x/\text{ITO@MIP}$  electrode's effective surface area, the sensitivity was calculated to be  $58.04 \mu\text{A} (\text{pM}^{-1}) \text{cm}^{-2}$ . Additionally, the LOD for the fabricated sensor was found to be 0.41 pM which is calculated by using the equation, i.e.,  $3\sigma/\text{sensitivity}$  where  $\sigma$  represents the standard deviation of MIP sensor. Due to the large surface area, the superior electrochemical properties and precise MIP recognition of the synthesized composite, the developed MIP sensor outperforms in terms of high sensitivity, low LOD and wider detection range.

#### 4.3.6 Interference, Reproducibility, Repeatability and Stability Analysis

The anti-interference ability of the developed MIP sensor was investigated by incubating the  $\text{TiO}_2\text{-Ti}_3\text{C}_2\text{T}_x/\text{ITO@MIP}$  electrode with 10 nM of different interfering analytes including several antibiotics (NOR, CIP, OME, AZY and AMP) as well as some organic and inorganic analytes such as glucose (GLU), uric acid,  $\text{NO}_3^-$ , KCl and  $\text{SO}_4^{2-}$  with a coexistence of 0.1 nM LEV. It is clearly observed from **Fig. 4.8(A)** that even with a 100 times higher concentration of these interfering species, the proposed  $\text{TiO}_2\text{-}$

Ti<sub>3</sub>C<sub>2</sub>T<sub>x</sub>/ITO@MIP sensor shows no significant change in peak current suggesting high selectivity for LEV detection. Furthermore, the specificity of the MIP sensor was examined with a mixture of all interfering analytes, in addition to LEV. The MIP sensor exhibits a positive response towards LEV confirming the high specificity of the sensor.

To examine the reproducibility of the TiO<sub>2</sub>-Ti<sub>3</sub>C<sub>2</sub>T<sub>x</sub>/ITO@MIP sensor under the optimal conditions, 5 independent MIP electrodes were prepared for LEV detection. The prepared electrodes were then subjected to a 0.1 nM LEV concentration and then DPV current response was recorded. The results reveal an RSD value of 2.10% (**Fig. 4.8B**) suggesting good reproducibility of this fabricated sensor.

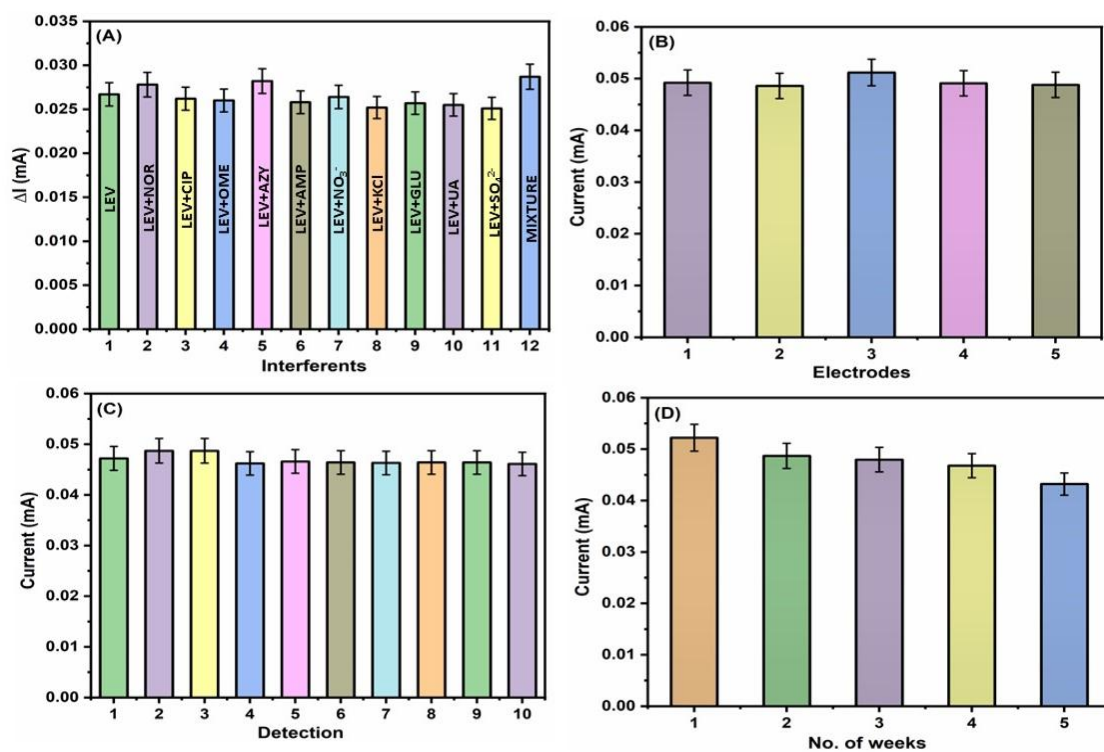


**Fig. 4.8** (A) Interference study of TiO<sub>2</sub>-Ti<sub>3</sub>C<sub>2</sub>T<sub>x</sub>/ITO@MIP electrode in presence of other interfering species (10 nM) along with 0.1 nM LEV (B) Reproducibility of the fabricated TiO<sub>2</sub>-Ti<sub>3</sub>C<sub>2</sub>T<sub>x</sub>/ITO@MIP sensor (C) Repeatability of the fabricated TiO<sub>2</sub>-Ti<sub>3</sub>C<sub>2</sub>T<sub>x</sub>/ITO@MIP sensor and (D) Shelf-life study of the TiO<sub>2</sub>-Ti<sub>3</sub>C<sub>2</sub>T<sub>x</sub>/ITO@MIP sensor

The repeatability of this fabricated  $\text{TiO}_2\text{-Ti}_3\text{C}_2\text{T}_x/\text{ITO@MIP}$  sensor was evaluated using ten consecutive measurements in the presence of 0.1 nM LEV yielding an RSD of 2.12% (**Fig. 4.8C**) which suggests an excellent repeatability of the MIP sensor. Furthermore, to assess the shelf life of the fabricated MIP sensor, the DPV response of the  $\text{TiO}_2\text{-Ti}_3\text{C}_2\text{T}_x/\text{ITO@MIP}$  electrode was measured with 0.1 nM LEV weekly over a period of five weeks (**Fig. 4.8D**). It is observed that the sensor retains 82.8% of its initial value after 5 weeks confirming the acceptable stability for LEV detection.

### 4.3.7 Real Sample Analysis

**Table 4.1:** Detection of LEV in spiked real samples using  $\text{TiO}_2\text{-Ti}_3\text{C}_2\text{T}_x/\text{ITO@MIP}$  electrode

Sample	Added (nM)	$\text{TiO}_2\text{-Ti}_3\text{C}_2\text{T}_x/\text{ITO@MIP}$		
		Found (nM)	Recovery (%)	RSD (%)
Urine	0	0	-	-
	0.001	0.0009	92.6	5.38
	0.01	0.009	90.0	7.38
	0.1	0.102	102.9	2.05
Human serum	0	0	-	-
	0.001	0.0009	95.2	3.41
	0.01	0.009	96.3	2.64
	0.1	0.099	99.0	0.67
Soil	0	0	-	-
	0.001	0.0009	93.6	4.65
	0.01	0.009	92.4	5.57
	0.1	0.09	96.3	2.66
River water	0	0	-	-
	0.001	0.0009	95.7	3.09
	0.01	0.009	99.4	0.40
	0.1	0.097	97.4	1.83

To assess the practical utility of this fabricated MIP sensor, the  $\text{TiO}_2\text{-Ti}_3\text{C}_2\text{T}_x/\text{ITO@MIP}$  electrode was analyzed to detect LEV in spiked biological samples (urine and human serum) and environmental samples (river water and soil). Before analysis, these real samples were diluted 50 times by using 0.1 M PBS of pH 7 and then spiked with varying LEV concentrations (0.001, 0.01 and 0.1 nM) to assess the recovery. The recovered percentage of LEV ranging from 90.0 to 102.9 % with an RSD <10 % and the data have been presented in **Table 4.1**. As a result, the proposed MIP sensor has a great potential for detecting LEV residues in biological and environmental samples.

#### **4.4 Conclusion**

This chapter reports the development of an efficient and simple  $\text{TiO}_2\text{-Ti}_3\text{C}_2\text{T}_x$  functionalized MIP electrochemical sensor for the selective detection of LEV. The hydrothermally synthesized 2D/2D  $\text{TiO}_2\text{-Ti}_3\text{C}_2\text{T}_x$  composite possesses large surface area and better electrical conductivity enhances the electrochemical response of MIP sensor by providing abundant imprinted sites for binding LEV molecules. The incorporation of  $\text{TiO}_2$  into  $\text{Ti}_3\text{C}_2\text{T}_x$  improves charge-transfer efficiency and prevents restacking which results in the improvement in the overall stability and sensitivity of the fabricated sensor. Under optimal experimental conditions, the  $\text{TiO}_2\text{-Ti}_3\text{C}_2\text{T}_x/\text{ITO@MIP}$  sensor exhibits good linearity in the concentration range of 1 pM to 100 nM, with a low detection limit of 0.41 pM. This sensor also shows the superior selectivity, good reproducibility and acceptable stability. Moreover, satisfactory detection of LEV in spiked real samples, with a recovery range of 90.0 to 102.9%, indicates the accuracy and reliability of the proposed MIP sensor for its potential application in various fields.

*The results of the present study have been published in “Journal of Solid State Electrochemistry” 29, 5283-5295 (2025).*

**References**

1. N. Liu, L. Yu, B. Liu, F. Yu, L. Li, Y. Xiao, J. Yang, and J. Ma,  $\text{Ti}_3\text{C}_2$ -MXene partially derived hierarchical 1D/2D  $\text{TiO}_2/\text{Ti}_3\text{C}_2$  heterostructure electrode for high-performance capacitive deionization, *Advanced Science*, 10 (2023) 2204041.
2. Li, L., G. Jiang, C. An, Z. Xie, Y. Wang, L. Jiao, and H. Yuan, Hierarchical  $\text{Ti}_3\text{C}_2@\text{TiO}_2$  MXene hybrids with tunable interlayer distance for highly durable lithium-ion batteries, *Nanoscale*, 12 (2020) 10369-10379.
3. C. Peng, T. Zhou, P. Wei, X. Yan, Y. Kong, W. Xu, H. Wang, H. Yu, J. Jia, K. Zhang, B. Zhou, and H. Pan, Steering interfacial charge kinetics: Synergizing cocatalyst roles of  $\text{Ti}_3\text{C}_2\text{M}_x$  (MXene) and NCDs for superior photocatalytic performance over  $\text{TiO}_2$ , *Applied Surface Science*, 599 (2022) 154001.
4. Sweetey, and D. Kumar, Electrochemical immunosensor based on titanium dioxide grafted MXene for EpCAM antigen detection, *Journal of Colloid and Interface Science*, 652 (2023) 549-556.
5. N. Murugan, R. Jerome, M. Preethika, A. Sundaramurthy, and A.K. Sundramoorthy, 2D-titanium carbide (MXene) based selective electrochemical sensor for simultaneous detection of ascorbic acid, dopamine and uric acid, *Journal of Materials Science & Technology*, 72 (2021) 122-131.
6. J. Yu, M. Zeng, J. Zhou, H. Chen, G. Cong, H. Liu, M. Ji, C. Zhu, and J. Xu, A one-pot synthesis of nitrogen doped porous MXene/ $\text{TiO}_2$  heterogeneous film for high-performance flexible energy storage, *Chemical Engineering Journal*, 426 (2021) 130765.
7. W. Lv, J. Zhu, F. Wang, and Y. Fang, Facile synthesis and electrochemical performance of  $\text{TiO}_2$  nanowires/ $\text{Ti}_3\text{C}_2$  composite, *Journal of Materials Science: Materials in Electronics*, 29 (2018) 4881-4887.
8. G. Li, X. Qi, J. Wu, X. Wan, T. Wang, Y. Liu, Y. Chen, and Y. Xia, Highly stable electrochemical sensing platform for the selective determination of pefloxacin in food samples based on a molecularly imprinted-polymer-coated gold nanoparticle/black phosphorus nanocomposite, *Food Chemistry*, 436 (2024) 137753.

## CuS Embedded $\text{Ti}_3\text{C}_2\text{T}_x$ -based Molecularly Imprinted Impedimetric Sensor for Levofloxacin Detection

### 5.1 Introduction

Herein, we have developed an MIP-based impedimetric sensor for levofloxacin detection by synergistically integrating CuS with 2D- $\text{Ti}_3\text{C}_2\text{T}_x$  (Fig. 5.1). The incorporation of CuS with  $\text{Ti}_3\text{C}_2\text{T}_x$  provides an increased surface area and abundant active sites, which facilitate LEV adsorption and further amplify the electrochemical signal response by enhancing electron transfer kinetics [1, 2]. The fabricated sensor exhibits good selectivity and a low detection limit for the detection of LEV. The details of the synthesis, characterisation, optimisation and electrochemical parameters of MIP sensor are being described in the following sections.

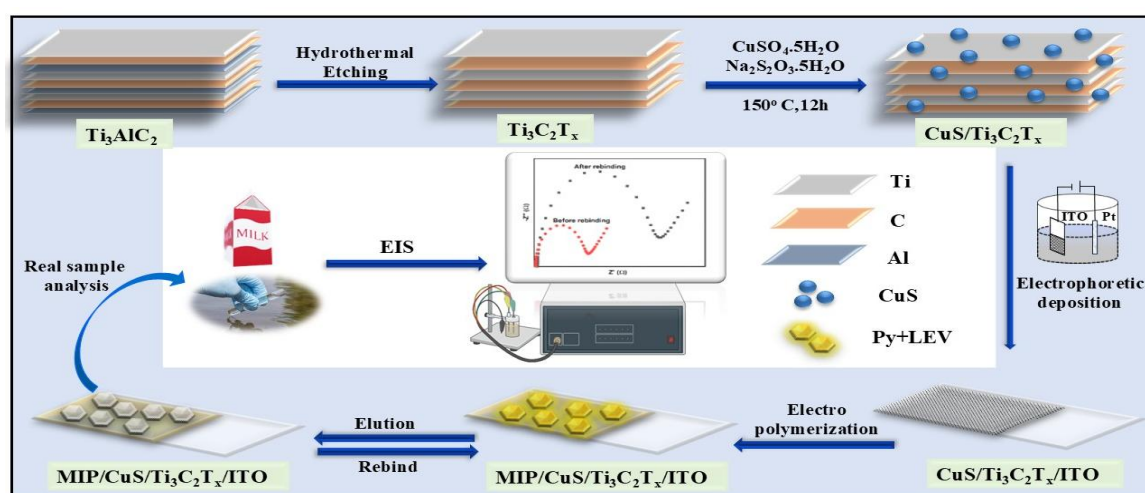


**Fig. 5.1** Scheme representing the CuS/Ti<sub>3</sub>C<sub>2</sub>T<sub>x</sub> modified MIP impedimetric sensor for LEV detection

## **5.2 Experimental Details**

### **5.2.1 Synthesis of CuS and CuS/Ti<sub>3</sub>C<sub>2</sub>T<sub>x</sub>**

CuS was synthesized in a similar manner as described earlier with slight modifications [3]. Firstly, 0.31 g each of copper sulfate and sodium thiosulfate was added to 20 mL of deionised water separately and agitated for 15 min. Afterwards, both solutions were mixed together while stirring for 30 min to obtain a homogeneous solution and then placed in an autoclave and treated at 150°C for a duration of 12 h. As the reactor reached to room temperature, the obtained dark-coloured precipitate was centrifuged and cleaned using a DI water/ethanol mixture. Then, the obtained product was vacuum-dried at 60°C.

CuS/Ti<sub>3</sub>C<sub>2</sub>T<sub>x</sub> composite was obtained by using one-pot hydrothermal method [4]. Initially, the prepared Ti<sub>3</sub>C<sub>2</sub>T<sub>x</sub> (120 mg), copper sulfate (156 mg) and sodium thiosulfate (155 mg) were dissolved thoroughly in 20 mL deionised water separately. After mixing all the solutions under constant stirring, the homogeneous mixture solution was transferred to autoclave (100 mL) and heated the same at 150°C for 12 h. Further, as it cooled down to room temperature, the resulting material was washed multiple times with DI water/ethanol mixture under centrifugation followed by vacuum drying at 60°C for 12 h.

### **5.2.2 Electrophoretic Deposition of CuS/Ti<sub>3</sub>C<sub>2</sub>T<sub>x</sub>**

To fabricate the sensor, the synthesized CuS/Ti<sub>3</sub>C<sub>2</sub>T<sub>x</sub> composite was deposited onto a pre-hydrolyzed conducting glass substrate coated with indium tin oxide (ITO) by utilizing the electrophoretic deposition technique. To achieve this goal, the synthesized composite (0.8 mg) was dispersed in 20 mL of DI water by an ultrasonification process. A two-electrode setup was employed for the EPD process consisting of a Pt wire and ITO which act as the reference and working electrode, respectively by keeping them 1cm apart. A thin and uniform film of CuS/Ti<sub>3</sub>C<sub>2</sub>T<sub>x</sub> was deposited onto the ITO surface after exposure to an optimized DC potential of 12 V for 8 sec.

### **5.2.3 Fabrication of CuS/Ti<sub>3</sub>C<sub>2</sub>T<sub>x</sub>/ITO@MIP Sensing Platform**

For sensor fabrication, the CuS/Ti<sub>3</sub>C<sub>2</sub>T<sub>x</sub> modified ITO was first immersed in an electrolytic solution of 0.1 M phosphate buffer (pH 7) containing LEV as template molecules (2 mM) and pyrrole as the functional monomer (8 mM). The cyclic voltammetry (CV) was employed at a potential window between 0.6 V to 1.6 V for ten consecutive scan segments at a scanning rate of 75 mV/s for the electropolymerization of LEV-imprinted Ppy film. Subsequently, to extract the template molecules, the constructed MIP electrode was placed in a mixture of sodium hydroxide (0.2 M) and ethanol (1:1 v/v) under stirring conditions for 25 min, followed by gently rinsing with DI water and drying at room temperature. Similarly, a non-imprinted electrode (CuS/Ti<sub>3</sub>C<sub>2</sub>T<sub>x</sub>/ITO@NIP), serving as a control, has been fabricated using the same process without the inclusion of template molecules.

## **5.3 Results and Discussion**

### **5.3.1 Structural Characterization**

The XRD spectra of Ti<sub>3</sub>AlC<sub>2</sub>, Ti<sub>3</sub>C<sub>2</sub>T<sub>x</sub> (black curve), CuS (red curve) and CuS/Ti<sub>3</sub>C<sub>2</sub>T<sub>x</sub> (blue curve) are shown in **Fig. 5.2(A)**. Ti<sub>3</sub>AlC<sub>2</sub> (MAX Phase) shows diffraction peaks at  $2\theta = 9.6^\circ, 19.0^\circ, 34.1^\circ, 36.8^\circ, 39.0^\circ, 41.5^\circ, 48.3^\circ, 56.2^\circ, 60.1^\circ$  and  $65.3^\circ$ . After hydrothermal etching, the XRD spectra of Ti<sub>3</sub>C<sub>2</sub>T<sub>x</sub> exhibit a broad peak at  $6.5^\circ$  and the absence of the  $39.0^\circ$  peak confirms the complete elimination of the Al layer indicating the successful synthesis of Ti<sub>3</sub>C<sub>2</sub>T<sub>x</sub> sheets [5]. For CuS, distinct peaks were observed at  $2\theta = 27.8^\circ, 29.2^\circ, 31.6^\circ, 32.7^\circ, 48.0^\circ, 52.7^\circ$  and  $60.7^\circ$ , which confirms the formation of a pure structure of CuS without any impurities [6]. On the other hand, the composite (CuS/Ti<sub>3</sub>C<sub>2</sub>T<sub>x</sub>) exhibits both the peaks of Ti<sub>3</sub>C<sub>2</sub>T<sub>x</sub> and CuS, further indicating the successful integration of CuS onto the MXene sheets without altering their crystal structures. The functional groups of Ti<sub>3</sub>C<sub>2</sub>T<sub>x</sub> (black), CuS (red) and CuS/Ti<sub>3</sub>C<sub>2</sub>T<sub>x</sub> (blue) were analyzed with the help of FTIR spectroscopy as illustrated in **Fig. 5.2(B)**.

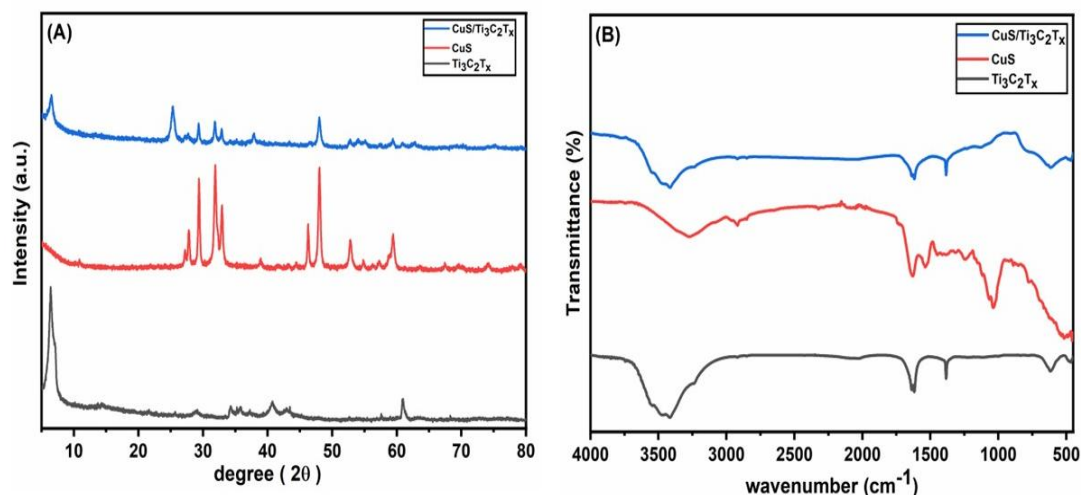


**Fig. 5.2** (A) XRD pattern and (B) FTIR spectra of Ti<sub>3</sub>C<sub>2</sub>T<sub>x</sub> (black), CuS (red) and CuS/Ti<sub>3</sub>C<sub>2</sub>T<sub>x</sub> (blue)

The FTIR spectra of Ti<sub>3</sub>C<sub>2</sub>T<sub>x</sub> show peaks at 623, 1390, 1628 and 2911 cm<sup>-1</sup> correspond to the stretching vibrations of Ti–O, O–H, C=O and C–H bonds, respectively. For CuS, a peak at 519 cm<sup>-1</sup> represents the stretching vibrations of Cu–S while the peaks at 857 and 1039 cm<sup>-1</sup> represent the C–H bending vibrations and C–O stretching vibrations of absorbed alcohol, respectively [7]. FTIR spectra of CuS/Ti<sub>3</sub>C<sub>2</sub>T<sub>x</sub> exhibit all the characteristic peaks of CuS and Ti<sub>3</sub>C<sub>2</sub>T<sub>x</sub>.

### 5.3.2 Morphological Characterization

FESEM was used to analyze the surface morphologies of prepared materials and fabricated electrodes as shown in **Fig. 5.3**. According to **Fig. 5.3A**, the morphology of Ti<sub>3</sub>AlC<sub>2</sub> exhibits a stacked layered structure before LiF etching. After etching, the resulting MXene gives a 2D lamellar structure that resembles an accordion shape as displayed in **Fig. 5.3B**. It is clearly seen in **Fig. 5.3C** that the spherical-shaped CuS is anchored on layered surface of MXene. The morphology of CuS/Ti<sub>3</sub>C<sub>2</sub>T<sub>x</sub>/ITO@MIP before template elution exhibits a smooth and uniform surface as depicted in **Fig. 5.3D**. After elution, the MIP film structure collapses and resulting in a rougher and porous surface of the CuS/Ti<sub>3</sub>C<sub>2</sub>T<sub>x</sub>/ITO@MIP

electrode as seen in **Fig. 5.3E**. The EDX spectrum of CuS/Ti<sub>3</sub>C<sub>2</sub>T<sub>x</sub> (**Fig. 5.3F**) reveals the presence of Ti, C, O, F, Cu and S which indicates that CuS is loaded onto the Ti<sub>3</sub>C<sub>2</sub>T<sub>x</sub> sheets.

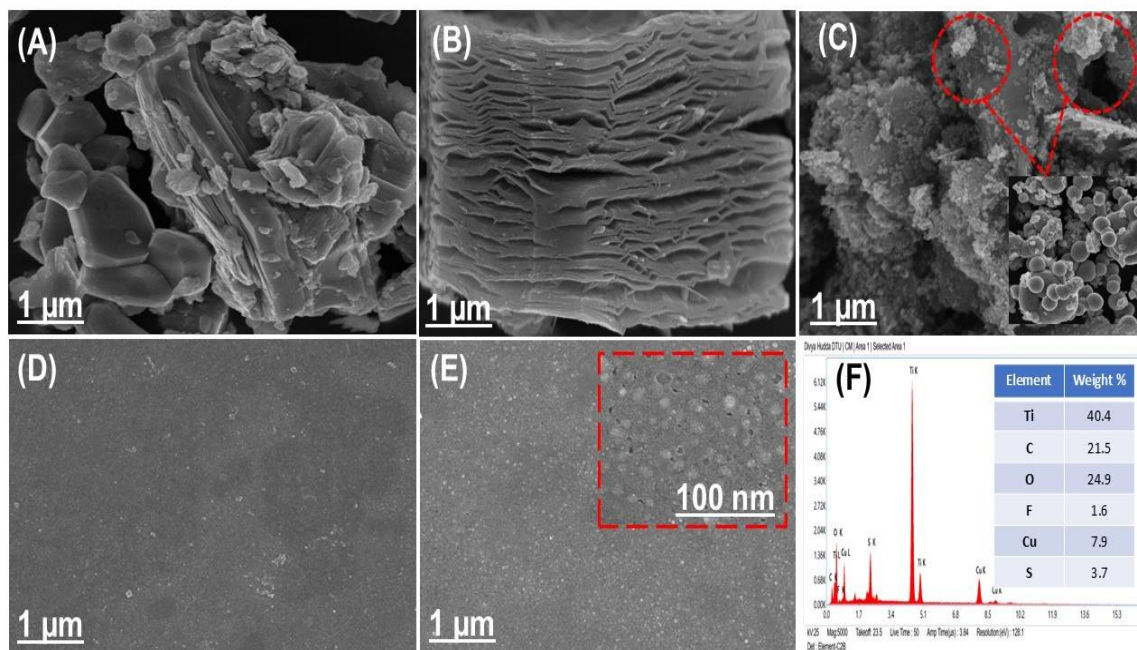


**Fig. 5.3** FESEM micrographs of (A) Ti<sub>3</sub>AlC<sub>2</sub> (B) Ti<sub>3</sub>C<sub>2</sub>T<sub>x</sub> (C) CuS/Ti<sub>3</sub>C<sub>2</sub>T<sub>x</sub> (D) CuS/Ti<sub>3</sub>C<sub>2</sub>T<sub>x</sub>/ITO@MIP before elution (E) CuS/Ti<sub>3</sub>C<sub>2</sub>T<sub>x</sub>/ITO@MIP after elution and (F) EDX analysis of CuS/Ti<sub>3</sub>C<sub>2</sub>T<sub>x</sub>

### 5.3.3 Electrochemical Characterization

The CV and EIS measurements of each modified electrode were conducted to study the electrochemical properties and interfacial charge kinetics in a mixture of PBS (0.1 M) containing 0.9% NaCl and 5 mM [Fe(CN)<sub>6</sub>]<sup>3-/4-</sup>. **Fig. 5.4A** shows that the redox peak current of CuS/Ti<sub>3</sub>C<sub>2</sub>T<sub>x</sub>/ITO (curve **c**) is significantly higher than bare ITO (curve **a**) and Ti<sub>3</sub>C<sub>2</sub>T<sub>x</sub>/ITO (curve **b**), owing to the synergistic effect of different components of the composite, which could accelerate the electron transfer process. Following Ppy-LEV electropolymerization at the CuS/Ti<sub>3</sub>C<sub>2</sub>T<sub>x</sub>/ITO electrode surface resulted in the disappearance of the redox peak current (curve **d**) because of the poor electron transferability of the MIP layer. Notably, the redox peak current increases significantly after

the extraction of embedded LEV molecules from the polymer matrix (curve **e**), indicating that the formed imprinted cavities provide a channel for electronic transmission. Furthermore, the redox peak current decreases (curve **f**) after LEV rebinding, confirming that the target analyte reoccupies the binding cavities, which hinders the electron transfer of the redox probe. Meanwhile, CuS/Ti<sub>3</sub>C<sub>2</sub>T<sub>x</sub>/ITO@NIP electrode upon elution shows no significant change in peak current intensity, as there is no doping of template molecules (curve **g**).

EIS is a practical tool for identifying changes in electrode properties at the electrode surface, enabling an understanding of the chemical reactions and processes that have occurred there. An EIS study was performed to determine the charge transfer resistance ( $R_{ct}$ ) of each modified electrode in a 0.01-10<sup>5</sup> Hz frequency range with a set potential of 0.01 V [8]. The Nyquist plot consists of a semicircle representing an electron transfer-limited process at higher frequencies and a linear line representing diffusion-controlled process at low frequencies. As displayed in **Fig. 5.4B**, the  $R_{ct}$  of CuS/Ti<sub>3</sub>C<sub>2</sub>T<sub>x</sub>/ITO decreases to 38.2  $\Omega$  (inset curve **c**) in comparison to bare ITO (67.1  $\Omega$ , inset curve **a**) and Ti<sub>3</sub>C<sub>2</sub>T<sub>x</sub>/ITO (57.0  $\Omega$ , inset curve **b**) indicating the fastest electron transfer at the electrode/electrolyte sensing interface due to the synergistic effect of material. After assembling Ppy-LEV on CuS/Ti<sub>3</sub>C<sub>2</sub>T<sub>x</sub>/ITO electrode, the  $R_{ct}$  significantly increases to 1.77 k $\Omega$  (curve **d**) due to the obstruction of electrons by non-conductive MIP layer. After template elution, the  $R_{ct}$  further decreases to 144  $\Omega$  (inset curve **e**) as the formed imprinted cavities transfer the electron between the electrode and electrolyte interface.  $R_{ct}$  further increases to 152  $\Omega$  (inset curve **f**) after rebinding the LEV molecules. It is because of the reason that some cavities are occupied by the LEV which reduces the electron transfer process. Notably, the  $R_{ct}$  value for CuS/Ti<sub>3</sub>C<sub>2</sub>T<sub>x</sub>/ITO@NIP electrode was found to be 1.22 k $\Omega$  (curve **g**) upon elution, demonstrating the lack of formation of imprinted sites. These findings align with the earlier CV results.

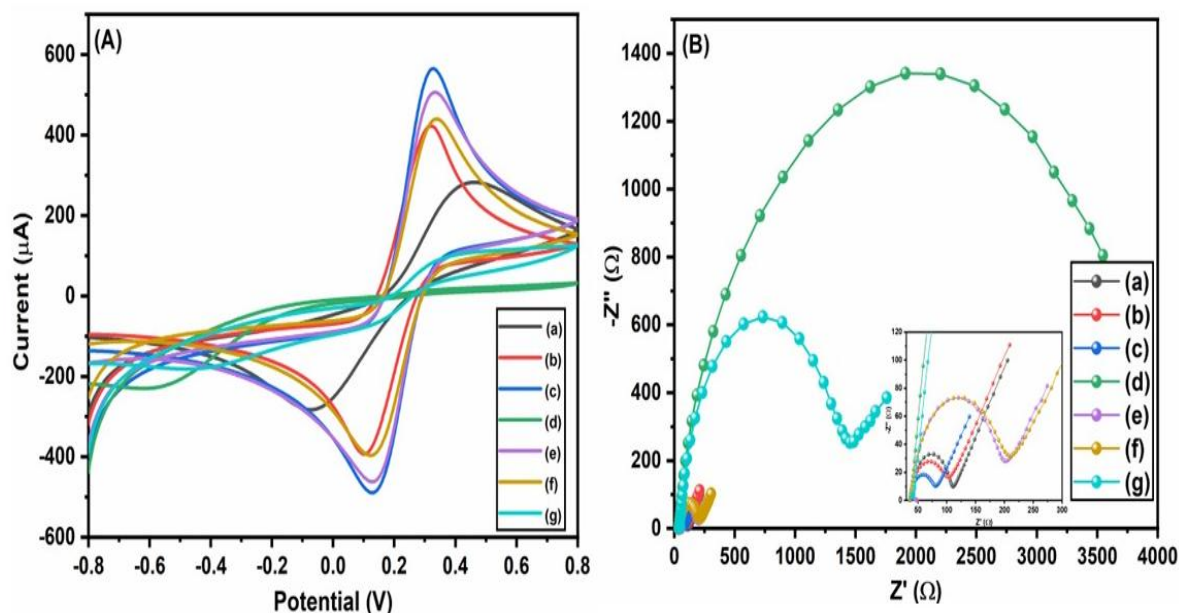


**Fig. 5.4** (A) CV plots and (B) EIS curves of various modified electrodes: (a) ITO (b)  $\text{Ti}_3\text{C}_2\text{T}_x/\text{ITO}$  (c)  $\text{CuS}/\text{Ti}_3\text{C}_2\text{T}_x/\text{ITO}$  (d)  $\text{CuS}/\text{Ti}_3\text{C}_2\text{T}_x/\text{ITO}@MIP$  before elution (e)  $\text{CuS}/\text{Ti}_3\text{C}_2\text{T}_x/\text{ITO}@MIP$  after elution (f)  $\text{CuS}/\text{Ti}_3\text{C}_2\text{T}_x/\text{ITO}@MIP$  after rebinding and (g)  $\text{CuS}/\text{Ti}_3\text{C}_2\text{T}_x/\text{ITO}@NIP$  after elution

Further, the scan rate study (10-300 mV/s) has been performed for  $\text{CuS}/\text{Ti}_3\text{C}_2\text{T}_x/\text{ITO}@MIP$  electrode using the CV technique which is depicted in **Fig. 5.5A**. A linear behaviour has been observed in **Fig. 5.5B** when plotting the redox potential against log scan rate for the modified electrode which follows **Eqs. 5.1 and 5.2**.

$$E_{pa}[\text{CuS}/\text{Ti}_3\text{C}_2\text{T}_x/\text{ITO}@MIP] = 0.194 \text{ (V)} + 0.087 \text{ (V)} * \log [v \text{ (mV/s)}]; R^2 = 0.977 \quad (5.1)$$

$$E_{pc}[\text{CuS}/\text{Ti}_3\text{C}_2\text{T}_x/\text{ITO}@MIP] = 0.239 \text{ (V)} - 0.065 \text{ (V)} * \log [v \text{ (mV/s)}]; R^2 = 0.984 \quad (5.2)$$

Based on Laviron's theory (Eqs. 2.3 to 2.5),  $\alpha$  and  $K_s$  for  $\text{CuS}/\text{Ti}_3\text{C}_2\text{T}_x/\text{ITO}@MIP$  electrode are being calculated and found to be 0.92 and  $0.1 \text{ s}^{-1}$ , respectively.

Similarly, a plot of anodic and cathodic peak currents vs. square root of scan rate shows a linear dependency indicates a surface-controlled process as depicted in **Fig. 5.5C** which follows **Eqs. 5.3 and 5.4**.

$$I_{pa} [\text{CuS}/\text{Ti}_3\text{C}_2\text{T}_x/\text{ITO}@\text{MIP}] = 147 (\mu\text{A}) + 53 (\mu\text{A}) (\text{mV}/\text{s}) * (\text{mV}/\text{s})^{1/2} v^{1/2}; R^2 = 0.993 \quad (5.3)$$

$$I_{pc} [\text{CuS}/\text{Ti}_3\text{C}_2\text{T}_x/\text{ITO}@\text{MIP}] = -190 (\mu\text{A}) - 38.7 (\mu\text{A}) (\text{mV}/\text{s}) * (\text{mV}/\text{s})^{1/2} v^{1/2}; R^2 = 0.988 \quad (5.4)$$

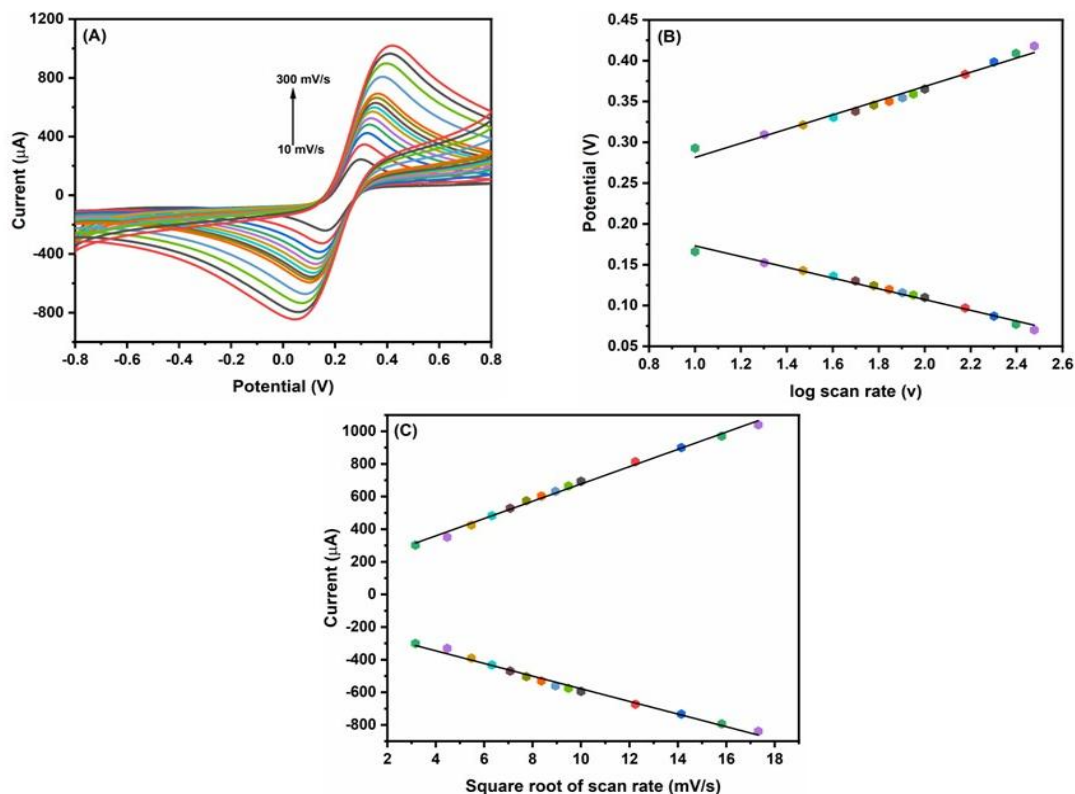


**Fig. 5.5** (A) Cyclic voltammograms at various scan rates (10-300 mV/s) (B) linear curves of redox peak potential with log of scan rate and (C) linear curves of peak current against square root of scan rate for CuS/Ti<sub>3</sub>C<sub>2</sub>T<sub>x</sub>/ITO@MIP electrode

Based on the above equations and Randles-Sevick equation (**Eqs. 2.6**), the electrochemical interface characteristics including diffusion coefficient (D) and effective surface area (A) were calculated. The values of D and A for the CuS/Ti<sub>3</sub>C<sub>2</sub>T<sub>x</sub>/ITO@MIP electrode were determined to be  $18.07 \times 10^{-6} \text{ cm}^2/\text{s}$  and  $0.29 \text{ cm}^2$ , respectively. Moreover, the average surface area ( $\tau$ ) of MIP modified electrode was calculated using  $I_p = n^2 F^2 A \tau v / 4RT$  and found to be  $2.68 \times 10^{-8} \text{ mol}/\text{cm}^2$ .

### **5.3.4 Optimization of Experimental Conditions**

For achieving the best performance of fabricated MIP sensor, numerous factors including the pH of electrolytic solution, template-to-monomer ratio, number of electropolymerization cycles, scan rate effect, elution time and incubation time were optimized in an orderly manner by using the EIS approach. The optimal parameters were selected based on the lowest  $R_{ct}$  value obtained from the EIS data. However, the highest  $R_{ct}$  value was chosen for the incubation time, which shows the maximum attachment of the LEV molecules into the imprinted cavities. The electrolytic solution pH may influence the structural stability and imprinting film of the sensor. The pH effect between 5.0 to 9.0 is presented in **Fig. 5.6A** which shows that the lowest  $R_{ct}$  value was obtained at pH 7. The reason behind this phenomenon is that an excessively acidic or alkaline environment can reduce the sensor's sensitivity by weakening the MIP's film structural integrity. Therefore, the optimal pH was set to be 7 for subsequent measurements.

The ratio of template molecule to functional monomer can influence the generation of the imprinted cavities thereby affecting the sensor efficacy. Therefore, to optimize the molar ratio, monomer concentration (pyrrole) was varied while keeping the template molecule (LEV) concentration constant. As depicted in **Fig. 5.6B**, the lowest  $R_{ct}$  value was achieved at a molar ratio of 1:4. This behavior can be attributed to the fact that the low monomer concentration leads to fewer recognition sites while excessive monomer concentration causes self-polymerisation. Hence, the optimized molar ratio is 1:4.

The number of electropolymerization cycles was precisely controlled which in turn affects the thickness of MIP film thereby influencing the sensor's performance. As shown in **Fig. 5.6C**, the lowest  $R_{ct}$  value was observed for 10 scan cycles. This is due to the fact that a low number of scan cycles results in a thinner membrane which in turn causes fewer recognition sites on the surface of MIP sensor. In contrast, exceeding scan cycles beyond

10 produces a thicker Ppy film making it challenging to completely elute LEV molecules. Thus, 10 scan cycles were selected for further experimentation.

The sensor's performance is influenced by the effect of scan rate which precisely controls the density of MIP film. As illustrated in **Fig. 5.6D**, the effect of scan rate was analysed within the range of 25 to 125 mV/s and the lowest  $R_{ct}$  value was achieved at a scan rate of 75 mV/s. This phenomenon may be attributed to the fact that a low scan rate resulted in a dense MIP film which prevents template elution and hinders the charge transfer at the electrode surface interface. However, a fast scan rate led to the development of loose film with insufficient binding cavities and poor stability. Therefore, a scan rate of 75 mV/s has been selected as the optimal condition for the preparation of MIP film.

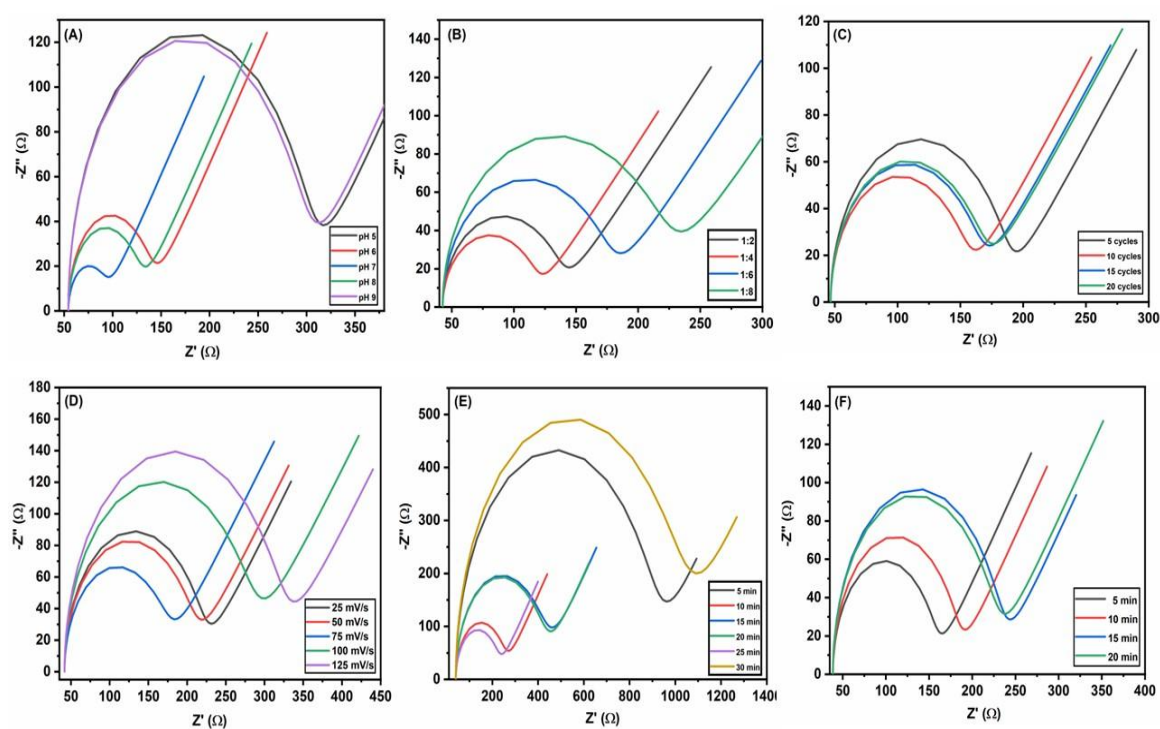


**Fig. 5.6** Optimization of the MIP fabrication conditions: Effect of (A) electropolymerization pH value (B) template to functional monomer concentration ratio (C) MIP scan cycles (D) scan rate (E) elution time and (F) incubation time of CuS/Ti<sub>3</sub>C<sub>2</sub>T<sub>x</sub>/ITO@MIP for LEV

Elution time and incubation time are considered to be the crucial parameters that directly impact the recognition kinetics of MIP sensor. As shown in **Fig. 5.6E**, the lowest  $R_{ct}$  value was observed after 25 min of elution time suggesting the complete extraction of template molecules from the Ppy matrix. **Fig. 5.6F** illustrates the effect of incubation time on the charge transfer resistance analyzed over a time period of 5 to 20 min. The  $R_{ct}$  value increases as the LEV molecules reoccupy the binding sites after absorption hindering charge transfer at the electron-solution interface. The maximum charge resistance was achieved at 15 min which was chosen as the optimum condition for further studies.

### 5.3.5 Electrochemical Response Studies for LEV Determination

Under optimal experimental conditions, EIS measurements were conducted to investigate the analytical performance of the proposed CuS/Ti<sub>3</sub>C<sub>2</sub>T<sub>x</sub>/ITO@MIP sensor for LEV detection. As illustrated in **Fig. 5.7A**, the EIS Nyquist curves exhibit a higher impedimetric response with increasing LEV concentrations, which ranged from 0.01 to 1000 pM.

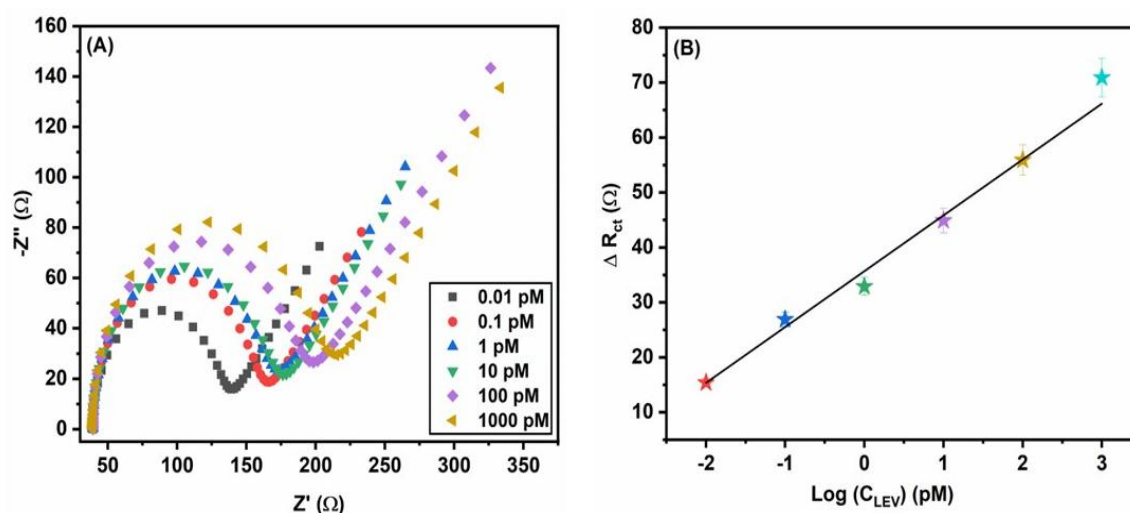


**Fig. 5.7 (A)** Electrochemical response of the fabricated CuS/Ti<sub>3</sub>C<sub>2</sub>T<sub>x</sub>/ITO@MIP sensor against various LEV concentrations (0.01-1000 pM) using the EIS method and **(B)** Linear fit curve between the logarithm of different LEV concentrations and  $\Delta R_{ct}$

This indicates that a larger number of imprinted sites are occupied by the LEV molecules which in turn obstructs the charge transfer transition for the redox probe. As described in **Fig. 5.7B**, a linear behaviour is found between the  $\Delta R_{ct}$  and logarithm of LEV concentration with a linear regression equation of  $R_{ct} = 10.16 \Omega \text{ pM}^{-1} \times \log C_{LEV} + 35.67 \Omega$ ;  $R^2=0.986$ . Additionally, the LOD was found to be 10 fM ( $\text{LOD} = 3\sigma/\text{sensitivity}$ , where  $\sigma$  depicts the standard deviation of the intercept). Moreover, the sensitivity of sensor was found to be  $65.03 \Omega \text{ pM}^{-1} \text{ cm}^{-2}$  which was estimated by employing the calibration plot between slope and the effective surface area of developed CuS/Ti<sub>3</sub>C<sub>2</sub>T<sub>x</sub>/ITO@MIP sensor.

### **5.3.6 Selectivity, Reproducibility and Stability Studies**

To assess the selectivity of the proposed MIP sensor, the EIS responses of CuS/Ti<sub>3</sub>C<sub>2</sub>T<sub>x</sub>/ITO@MIP electrode to other potential interfering analytes such as ciprofloxacin (CIP), norfloxacin (NOR), omeprazole (OME), azithromycin (AZY), ampicillin (AMP), glucose (GLU), ascorbic acid (AA) and nitrate salt ( $\text{NO}_3^{2-}$ ) that might affect the electrochemical response of LEV were investigated. As shown in **Fig. 5.8(A)**, the  $\Delta R_{ct}$  for LEV (1 pM) is much higher than other interfering species (100 pM) suggesting the excellent selectivity of CuS/Ti<sub>3</sub>C<sub>2</sub>T<sub>x</sub>/ITO@MIP sensor. These results demonstrated that the imprinted cavities resemble the shape, size and functionalities of LEV molecules. To investigate the reproducibility of the CuS/Ti<sub>3</sub>C<sub>2</sub>T<sub>x</sub>/ITO@MIP sensor, 5 different electrodes were prepared under the same protocols (**Fig. 5.8B**). The RSD was calculated to be 1.93% indicating the good reproducibility of the fabricated sensor for the detection of LEV. Finally, the stability of the fabricated sensor has been examined by storing the systematically prepared MIP-modified electrodes in a refrigerator at 4°C for six weeks (**Fig. 5.8C**). The signal response was measured every week in the presence of LEV, and it was found that the signal retained 88.2% of its initial value, confirming the satisfactory stability of the sensor.

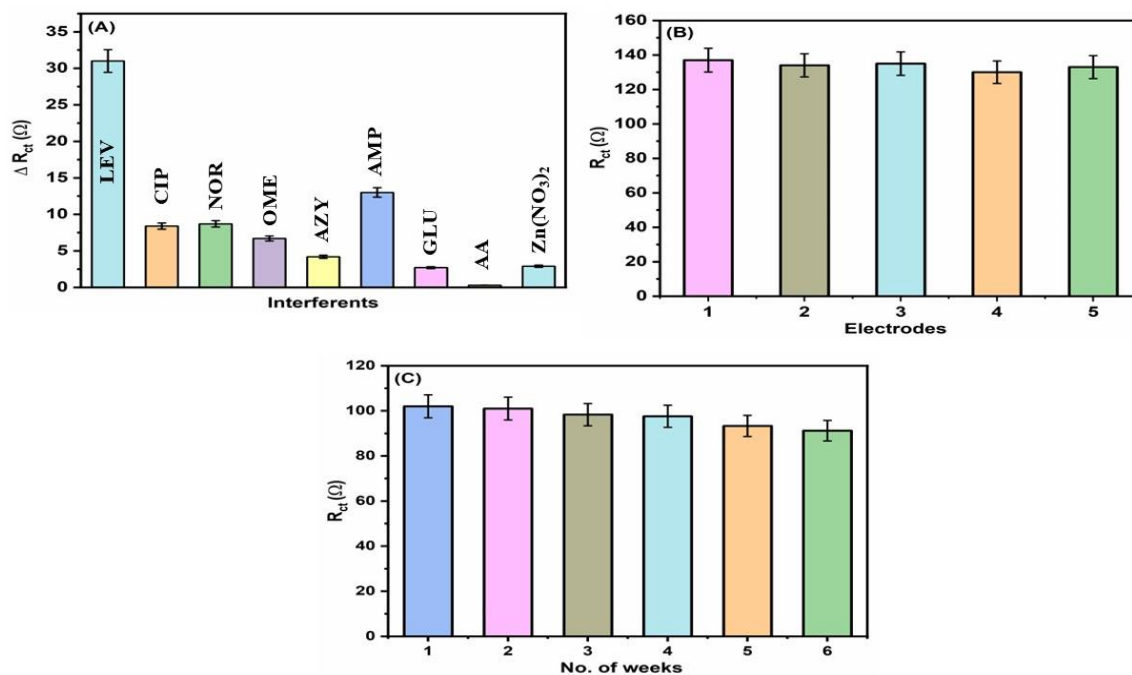


**Fig. 5.8** (A) Selectivity study of CuS/Ti<sub>3</sub>C<sub>2</sub>T<sub>x</sub>/ITO@MIP sensor towards LEV and other interfering species (B) Reproducibility study of CuS/Ti<sub>3</sub>C<sub>2</sub>T<sub>x</sub>/ITO@MIP sensor towards LEV using five different electrodes and (C) Stability of CuS/Ti<sub>3</sub>C<sub>2</sub>T<sub>x</sub>/ITO@MIP sensor over a period of 6 weeks

### 5.3.7 Real Sample Analysis

The practical applicability of CuS/Ti<sub>3</sub>C<sub>2</sub>T<sub>x</sub>/ITO@MIP sensor for quantifying LEV in two real sample matrices like milk and river water was evaluated by employing the standard addition method. Before analysis, the samples were diluted 20-fold with 0.1 M PBS (pH 7) and then subjected to varying concentrations of LEV (0.1, 1 and 10 pM). As given in **Table 5.1**, the recovery rates for the spiked milk sample ranged from 93.1 to 96.4% with RSD% of 2.59-5.03% and for the spiked river water, the recovery rates ranged from 92.8 to 98.5% with RSD% of 1.04-5.28%. These results demonstrate the sensor's reliability and accuracy in analysing LEV residues in environmental and food samples.

**Table 5.1:** Data of LEV in spiked real samples using CuS/Ti<sub>3</sub>C<sub>2</sub>T<sub>x</sub>/ITO@MIP electrode

Sample	Added (pM)	CuS/Ti <sub>3</sub> C <sub>2</sub> T <sub>x</sub> /ITO@MIP		
		Found (pM)	Recovery (%)	RSD (%)
Milk	0	0	-	-
	0.1	0.093	93.5	4.71
	1	0.93	93.1	5.03
	10	9.64	96.4	2.59
River water	0	0	-	-
	0.1	0.092	92.8	5.28
	1	0.94	94.5	3.94
	10	9.85	98.5	1.04

## 5.4 Conclusion

In the present work, a novel CuS/Ti<sub>3</sub>C<sub>2</sub>T<sub>x</sub> modified MIP electrochemical sensing interface was fabricated for LEV detection. The hydrothermally synthesized composite synergistically enhances the electrical conductivity and electrochemical activity while providing stable molecular recognition sites. The fabricated sensor demonstrated good analytical performance for the determination of LEV with a wide range of 0.01-1000 pM and LOD of 10 fM. Additionally, this proposed sensor offers an excellent anti-interference capability, reproducibility and stability in the presence of LEV. Furthermore, the practical validation of the constructed sensor towards spiked real samples shows a good recovery range from 92.8 to 98.5% confirming its reliability for the trace detection of LEV in complex real matrices.

**References**

1. Y. Sun, H. Gao, L. Xu, G.I. Waterhouse, H. Zhang, X. Qiao, and Z. Xu, Ultrasensitive determination of sulfathiazole using a molecularly imprinted electrochemical sensor with CuS microflowers as an electron transfer probe and Au@COF for signal amplification, *Food Chemistry*, 332 (2020) 127376.
2. Z. Pan, F. Cao, X. Hu, and X. Ji, A facile method for synthesizing CuS decorated Ti<sub>3</sub>C<sub>2</sub> MXene with enhanced performance for asymmetric supercapacitors, *Journal of Materials Chemistry A*, 7 (2019) 8984-8992.
3. J. Fang, P. Zhang, H. Chang, and X. Wang, Hydrothermal synthesis of nanostructured CuS for broadband efficient optical absorption and high-performance photo-thermal conversion, *Solar Energy Materials and Solar Cells*, 185 (2018) 456-463.
4. Sweety, S. Paneru, and D. Kumar, A Copper Sulfide Doped 2D-MXene-Based Ultrasensitive Label-Free Electrochemical Immunosensor for EpCAM Antigen Detection, *Applied Organometallic Chemistry*, 39 (2025) e7975.
5. D. Hudda, and D. Kumar, Molecularly imprinted polypyrrole decorated Ti<sub>3</sub>C<sub>2</sub>T<sub>x</sub> electrochemical sensor for highly selective and sensitive detection of levofloxacin, *Journal of Materials Science*, 59 (2024) 21684-21695.
6. Z. Li, L. Mi, W. Chen, H. Hou, C. Liu, H. Wang, Z. Zheng, and C. Shen, Three-dimensional CuS hierarchical architectures as recyclable catalysts for dye decolorization, *CrystEngComm*, 14 (2012) 3965-3971.
7. S. Riyaz, A. Parveen, and A. Azam, Microstructural and optical properties of CuS nanoparticles prepared by sol-gel route, *Perspectives in Science*, 8 (2016) 632-635.
8. S. Chatterjee, H. Singh, D. Hudda, Sweety, and D. Kumar, A Novel Acetylcholinesterase-Based Electrochemical Biosensor Using g-C<sub>3</sub>N<sub>4</sub>@MoS<sub>2</sub> Nanohybrid for the Detection of Trichlorfon, *Applied Organometallic Chemistry*, 38 (2024) e7721.



## Ag/TiO<sub>2</sub>-Ti<sub>3</sub>C<sub>2</sub>T<sub>x</sub> Modified Molecularly Imprinted Electrochemical Sensor for Levofloxacin Detection

### 6.1 Introduction

In this chapter, a novel ternary composite composed of Ag/TiO<sub>2</sub>-Ti<sub>3</sub>C<sub>2</sub>T<sub>x</sub> was successfully synthesized for the fabrication of highly sensitive MIP-based electrochemical sensor for LEV detection. The synergistic interactions between the components imparted an excellent electrical conductivity and good electrocatalytic activity thus enhancing its electrochemical response towards LEV oxidation [1, 2]. Moreover, the experimental results demonstrate that the fabricated MIP sensor achieved an outstanding LOD of 0.1 fM and a wide linear range of 0.1 fM-1000 nM for LEV. All the characterizations and electrochemical response studies have been analyzed and reported in the following sections.

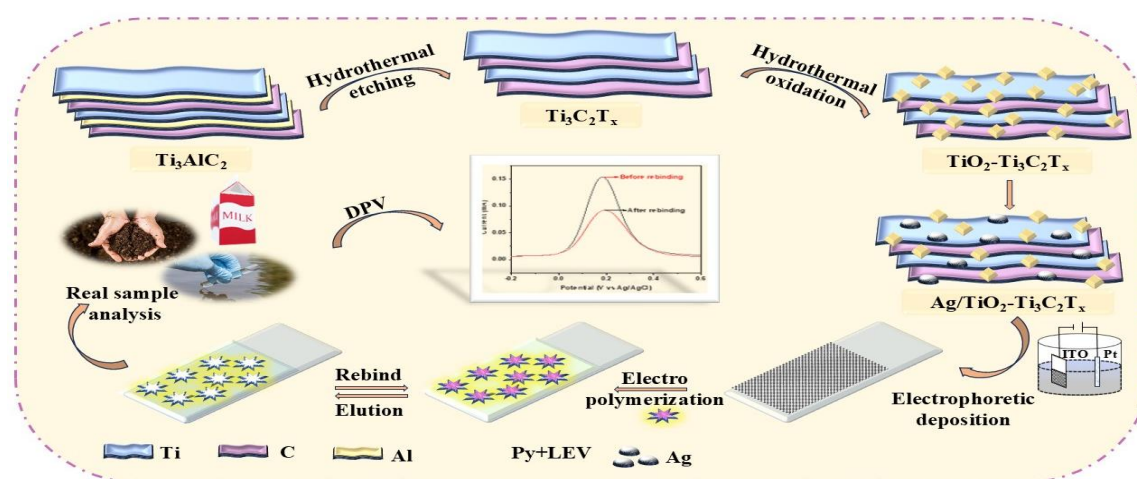


**Fig. 6.1** Scheme depicting the fabrication of Ag/TiO<sub>2</sub>-Ti<sub>3</sub>C<sub>2</sub>T<sub>x</sub> modified MIP electrochemical sensor

## **6.2 Experimental Details**

### **6.2.1 Synthesis of TiO<sub>2</sub>-Ti<sub>3</sub>C<sub>2</sub>T<sub>x</sub> and Ag/TiO<sub>2</sub>-Ti<sub>3</sub>C<sub>2</sub>T<sub>x</sub>**

TiO<sub>2</sub>-Ti<sub>3</sub>C<sub>2</sub>T<sub>x</sub> composite synthesis method has already been reported in chapter 4. To prepare Ag/TiO<sub>2</sub>-Ti<sub>3</sub>C<sub>2</sub>T<sub>x</sub> composite, 50 mg of the prepared TiO<sub>2</sub>-Ti<sub>3</sub>C<sub>2</sub>T<sub>x</sub> was dissolved in deionised water (20 mL) and stirred for 1 h to form a homogeneous solution. Afterwards, 2.5 mg/mL of AgNO<sub>3</sub> solution was dropwise supplemented to the above solution under constant stirring for 3 h [3]. After centrifuging and washing the resulting precipitate several times with DI water and an ethanol mixture to remove impurities, it was vacuum-dried at 60°C.

### **6.2.2 Electrophoretic Deposition of Ag/TiO<sub>2</sub>-Ti<sub>3</sub>C<sub>2</sub>T<sub>x</sub> Composite**

The EPD technique was employed for the deposition of synthesised composite (Ag/TiO<sub>2</sub>-Ti<sub>3</sub>C<sub>2</sub>T<sub>x</sub>) onto the pre-hydrolysed ITO-coated conducting glass substrate. Prior to the deposition, a colloidal solution was prepared containing 1 mg of Ag/TiO<sub>2</sub>-Ti<sub>3</sub>C<sub>2</sub>T<sub>x</sub> in 20 mL of DI water by an ultrasonification process. A smooth and thin layer of Ag/TiO<sub>2</sub>-Ti<sub>3</sub>C<sub>2</sub>T<sub>x</sub> was deposited on ITO surface following 10 sec of exposure to an optimum DC potential of 10 V using a two-electrode setup with a reference electrode (platinum wire) and the working electrode (ITO).

### **6.2.3 Preparation of Ag/TiO<sub>2</sub>-Ti<sub>3</sub>C<sub>2</sub>T<sub>x</sub>/ITO@MIP Sensor**

To prepare the MIP on Ag/TiO<sub>2</sub>-Ti<sub>3</sub>C<sub>2</sub>T<sub>x</sub>/ITO, the modified electrode (Ag/TiO<sub>2</sub>-Ti<sub>3</sub>C<sub>2</sub>T<sub>x</sub>/ITO) was first immersed in a 0.1 M phosphate buffer (pH 7) which contains 12.0 mM pyrrole (functional monomer) and 2.0 mM LEV (template molecules). Then, CV electropolymerization was conducted at a potential window between -0.6 to 1.6 V with ten scan cycles at 75 mV/s of scan rate. After that, to extract the template molecules from the embedded MIP film, the electrode was submerged in the mixture of NaOH/ethanol (0.2 M; 1:1 v/v) for 10 min under mild stirring conditions followed by washing with DI water to

remove the absorbed LEV molecules from electrode surface. For comparison, a non-imprinted electrode (Ag/TiO<sub>2</sub>-Ti<sub>3</sub>C<sub>2</sub>T<sub>x</sub>/ITO@NIP) was also fabricated under the same conditions without the addition of LEV molecules to serve as a control.

## **6.3 Results and Discussion**

### **6.3.1 Structural and Morphological Studies**

XRD analysis was performed to investigate the crystalline structure of Ti<sub>3</sub>AlC<sub>2</sub> (black curve), Ti<sub>3</sub>C<sub>2</sub>T<sub>x</sub> (red curve), TiO<sub>2</sub>-Ti<sub>3</sub>C<sub>2</sub>T<sub>x</sub> (blue curve) and Ag/TiO<sub>2</sub>-Ti<sub>3</sub>C<sub>2</sub>T<sub>x</sub> (green curve) and displayed in **Fig. 6.2A**. By comparing the XRD patterns of Ti<sub>3</sub>AlC<sub>2</sub> and Ti<sub>3</sub>C<sub>2</sub>T<sub>x</sub>, it is found that the peak of Ti<sub>3</sub>AlC<sub>2</sub> at  $2\theta = 9.52^\circ$  has been moved towards a lower angle of  $2\theta = 6.38^\circ$  suggesting an increase in the interplanar spacing from 9.28 to 13.85 Å. Moreover, disappearance of Ti<sub>3</sub>AlC<sub>2</sub> peak at  $2\theta = 38.9^\circ$  in Ti<sub>3</sub>C<sub>2</sub>T<sub>x</sub> spectra indicates the successful etching of Al layer and formation of multilayered MXene. In case of TiO<sub>2</sub>-Ti<sub>3</sub>C<sub>2</sub>T<sub>x</sub> composite, XRD peaks at  $2\theta = 25.2^\circ, 37.7^\circ, 47.8^\circ, 53.8^\circ, 54.8^\circ, 62.6^\circ, 68.8^\circ, 70.2^\circ$  and  $74.9^\circ$  represents the anatase phase of TiO<sub>2</sub> [4]. Additionally, a characteristic peak of Ti<sub>3</sub>C<sub>2</sub>T<sub>x</sub> shifts from  $6.38^\circ$  to  $5.90^\circ$  indicating the enlarged interlayer spacing of 14.96 Å. Furthermore, the deposition of Ag particles on TiO<sub>2</sub>-Ti<sub>3</sub>C<sub>2</sub>T<sub>x</sub> composite resulting in the modification of XRD spectra. The diffraction peak of TiO<sub>2</sub>-Ti<sub>3</sub>C<sub>2</sub>T<sub>x</sub> composite was augmented by additional peaks at  $2\theta = 38.0^\circ, 44.3^\circ, 64.5^\circ$  and  $77.2^\circ$  that correspond to the metallic Ag [5]. The integration of Ag within the TiO<sub>2</sub>-Ti<sub>3</sub>C<sub>2</sub>T<sub>x</sub> matrix further results in a shift of Ti<sub>3</sub>C<sub>2</sub>T<sub>x</sub> peak from  $5.90^\circ$  to  $5.80^\circ$  which in turn leads to a large interlayer spacing of 15.23 Å. These findings confirm the successful synthesis of the ternary Ag/TiO<sub>2</sub>-Ti<sub>3</sub>C<sub>2</sub>T<sub>x</sub> composite.

The bond analysis of the prepared Ti<sub>3</sub>C<sub>2</sub>T<sub>x</sub> (black curve) and Ag/TiO<sub>2</sub>-Ti<sub>3</sub>C<sub>2</sub>T<sub>x</sub> (green curve) was conducted through the utilization of FTIR technique in a range of 500-4000 cm<sup>-1</sup> (**Fig. 6.2B**). FTIR spectra of Ti<sub>3</sub>C<sub>2</sub>T<sub>x</sub> display the stretching vibrations of C-H bonds at 2922 and 2846 cm<sup>-1</sup>. The peaks observed at 1624 and 1381 cm<sup>-1</sup> are attribute to stretching vibrations of

C=O and O–H bonds, respectively [6]. Additionally, the observed peaks at 614 and 471 cm<sup>-1</sup> correspond to the stretching vibrations of Ti–O and Ti–C bonds, respectively. In Ag/TiO<sub>2</sub>-Ti<sub>3</sub>C<sub>2</sub>T<sub>x</sub> spectra, the integration of Ag particles results in a decrease in the intensity of Ti–O and Ti–C peaks.

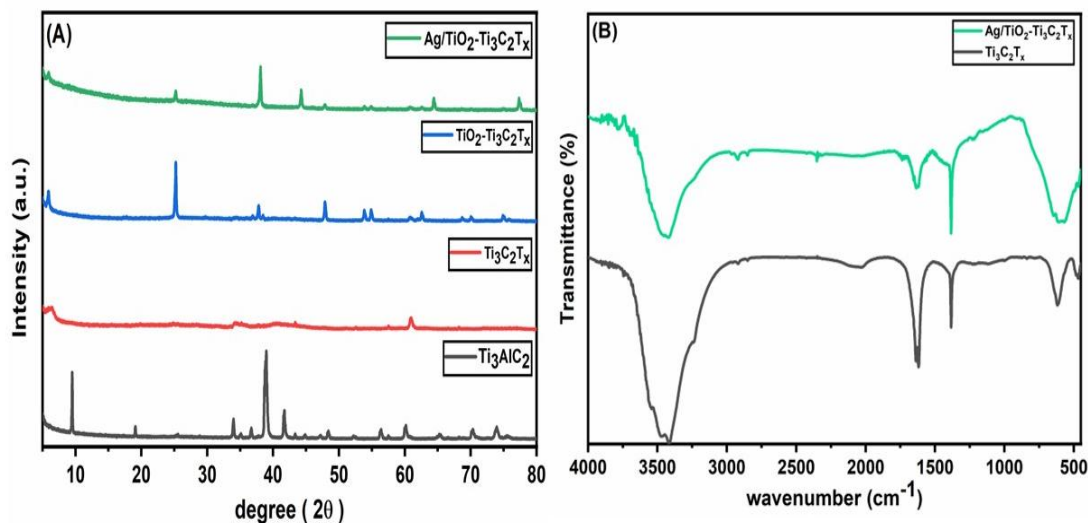


**Fig. 6.2** (A) XRD spectra of Ti<sub>3</sub>AlC<sub>2</sub> (black curve), Ti<sub>3</sub>C<sub>2</sub>T<sub>x</sub> (red curve), TiO<sub>2</sub>-Ti<sub>3</sub>C<sub>2</sub>T<sub>x</sub> (blue curve) and Ag/TiO<sub>2</sub>-Ti<sub>3</sub>C<sub>2</sub>T<sub>x</sub> (green curve) (B) FTIR spectra of Ti<sub>3</sub>C<sub>2</sub>T<sub>x</sub> (black curve) and Ag/TiO<sub>2</sub>-Ti<sub>3</sub>C<sub>2</sub>T<sub>x</sub> (green curve)

The vital information regarding the surface morphology of the synthesized materials and electrodes is provided by field-emission scanning electron microscopy (FESEM) as illustrated in **Fig. 6.3**. **Fig. 6.3A** displays the FESEM image of Ti<sub>3</sub>C<sub>2</sub>T<sub>x</sub> after the etching process which exhibits an accordion-like morphology. The FESEM image of TiO<sub>2</sub>-Ti<sub>3</sub>C<sub>2</sub>T<sub>x</sub> (**Fig. 6.3B**) reveals the even distribution of 2D TiO<sub>2</sub> sheets on the Ti<sub>3</sub>C<sub>2</sub>T<sub>x</sub> substrate. For Ag/TiO<sub>2</sub>-Ti<sub>3</sub>C<sub>2</sub>T<sub>x</sub> (**Fig. 6.3C**), it can be observed that Ag particles are uniformly loaded on the TiO<sub>2</sub>-Ti<sub>3</sub>C<sub>2</sub>T<sub>x</sub> surface obtained via a self-reduction process [7]. Prior to the template elution, Ag/TiO<sub>2</sub>-Ti<sub>3</sub>C<sub>2</sub>T<sub>x</sub>/ITO@MIP exhibited a smooth and homogeneous surface morphology as shown in **Fig. 6.3D**. When the MIP film structure collapses after the elution process, the Ag/TiO<sub>2</sub>-Ti<sub>3</sub>C<sub>2</sub>T<sub>x</sub>/ITO@MIP electrode's surface becomes rougher and more

porous (**Fig. 6.3E**). By EDX analysis, the presence of Ti, C, O, F and Ag confirms the successful synthesis of Ag/TiO<sub>2</sub>-Ti<sub>3</sub>C<sub>2</sub>T<sub>x</sub> composite (**Fig. 6.3F**).

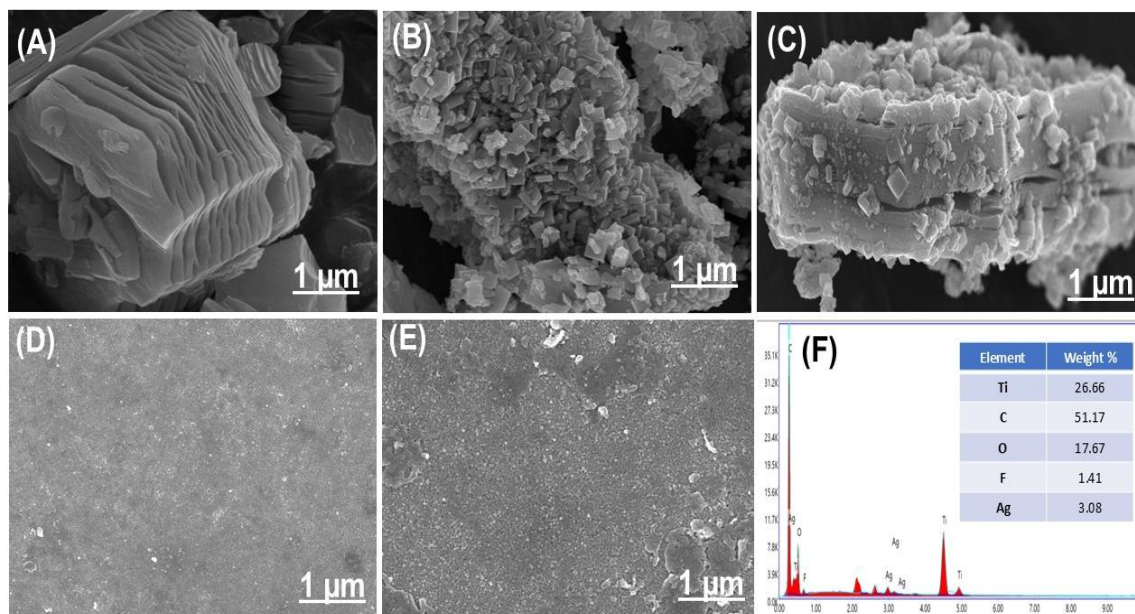


**Fig. 6.3** FESEM images of (A) Ti<sub>3</sub>C<sub>2</sub>T<sub>x</sub> (B) TiO<sub>2</sub>-Ti<sub>3</sub>C<sub>2</sub>T<sub>x</sub> (C) Ag/TiO<sub>2</sub>-Ti<sub>3</sub>C<sub>2</sub>T<sub>x</sub> (D) Ag/TiO<sub>2</sub>-Ti<sub>3</sub>C<sub>2</sub>T<sub>x</sub>/ITO@MIP before template elution (E) Ag/TiO<sub>2</sub>-Ti<sub>3</sub>C<sub>2</sub>T<sub>x</sub>/ITO@MIP after template elution and (F) EDX spectra of Ag/TiO<sub>2</sub>-Ti<sub>3</sub>C<sub>2</sub>T<sub>x</sub>

### 6.3.2 Electrochemical Characterization

Firstly, CV and EIS studies were employed to examine the electrochemical behaviour and charge transfer parameters of each modified electrode in a mixture of PBS (0.1 M) containing 5mM [Fe(CN)<sub>6</sub>]<sup>3-/4-</sup> as a redox probe. In **Fig. 6.4A**, a comparison with bare ITO (curve **a**), Ti<sub>3</sub>C<sub>2</sub>T<sub>x</sub>/ITO (curve **b**), TiO<sub>2</sub>-Ti<sub>3</sub>C<sub>2</sub>T<sub>x</sub>/ITO (curve **c**), the Ag/TiO<sub>2</sub>-Ti<sub>3</sub>C<sub>2</sub>T<sub>x</sub> modified ITO exhibits a high redox peak current (curve **d**) owing to high electrical conductivity and redox activity of Ag which on which when combined with TiO<sub>2</sub>-Ti<sub>3</sub>C<sub>2</sub>T<sub>x</sub> provides the robust synergistic effect between the materials which improves the electron kinetics of the electrode. **Fig. 6.4B** displays the CV curves of different polymerised electrodes. The electropolymerization of Ppy-LEV film on the surface of Ag/TiO<sub>2</sub>-

Ti<sub>3</sub>C<sub>2</sub>T<sub>x</sub>/ITO (curve **a**) results in the disappearance of redox peak current due to the non-conductive nature of MIP film that impedes the electron transfer process across the electrode-electrolyte interface. After template removal, the redox peak current of Ag/TiO<sub>2</sub>-Ti<sub>3</sub>C<sub>2</sub>T<sub>x</sub>/ITO@MIP electrode significantly increases (curve **b**), as the formed cavities within the MIP matrix enhance the electron transport efficiency across the electrode-electrolyte interface. Meanwhile, after rebinding of LEV molecules, the redox peak current of Ag/TiO<sub>2</sub>-Ti<sub>3</sub>C<sub>2</sub>T<sub>x</sub>/ITO@MIP electrode decreases (curve **c**) which suggests that the LEV molecules successfully recaptured inside the imprinted cavities and obstruct the charge transfer. Moreover, Ag/TiO<sub>2</sub>-Ti<sub>3</sub>C<sub>2</sub>T<sub>x</sub>/ITO@NIP electrode after elution was monitored and a CV curve (curve **d**) shows no significant change in the redox peak current due to insufficient formation of imprinted cavities.

The charge resistance behaviour ( $R_{ct}$ ) of each modified electrode was evaluated using EIS in 0.01-10<sup>5</sup> Hz frequency range with a set potential of 0.01 V. The Nyquist plot consists of a semicircle corresponding to electron transfer-limited process with higher frequencies and a linear line corresponding to a diffusion-controlled process with lower frequencies, respectively. **Fig. 6.4C** displays the EIS spectra of bare ITO (curve **a**), Ti<sub>3</sub>C<sub>2</sub>T<sub>x</sub>/ITO (curve **b**), TiO<sub>2</sub>-Ti<sub>3</sub>C<sub>2</sub>T<sub>x</sub>/ITO (curve **c**) and Ag/TiO<sub>2</sub>-Ti<sub>3</sub>C<sub>2</sub>T<sub>x</sub>/ITO (curve **d**) with  $R_{ct}$  values of 67.1, 57.0, 46.1 and 38.0  $\Omega$ , respectively. The results show that the Ag/TiO<sub>2</sub>-Ti<sub>3</sub>C<sub>2</sub>T<sub>x</sub>-modified ITO exhibits low charge transfer resistance which indicates that the synergistic effect of the composite has improved the electron kinetics. Furthermore, the EIS spectra of all the fabricated electrodes are shown in Fig. 6.4D. After modifying Ag/TiO<sub>2</sub>-Ti<sub>3</sub>C<sub>2</sub>T<sub>x</sub>/ITO with Ppy-LEV MIP layer, the  $R_{ct}$  significantly increases to 1.66 k $\Omega$  (curve **a**) as the electrode surface is coated with a non-conductive polymeric film hindering the electron transfer process. After the removal of LEV molecules, the  $R_{ct}$  dropped to 156  $\Omega$  (curve **b**) as the exposed imprinted cavities provide a channel for electron transfer between the electrode

and electrolyte interface. After incubation in LEV solution, the  $R_{ct}$  further increases to 223  $\Omega$  (curve c) due to the blockage of imprinted sites which hinders the electronic transmission. Meanwhile, after elution, the Ag/TiO<sub>2</sub>-Ti<sub>3</sub>C<sub>2</sub>T<sub>x</sub>/ITO@NIP electrode exhibits an  $R_{ct}$  of 1.01 k $\Omega$ , indicating the absence of imprinted cavity formation. These findings are consistent with the earlier CV analysis.

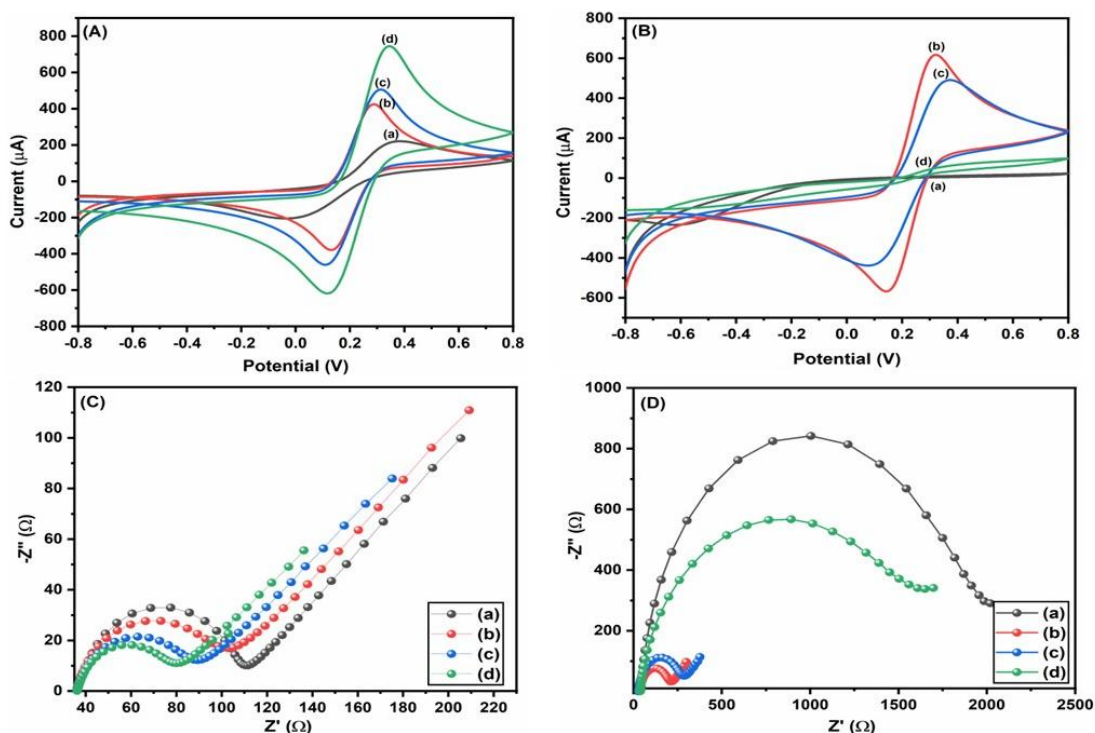


**Fig. 6.4** (A) CV plots and (C) EIS curves of (a) ITO (b) Ti<sub>3</sub>C<sub>2</sub>T<sub>x</sub>/ITO (c) TiO<sub>2</sub>-Ti<sub>3</sub>C<sub>2</sub>T<sub>x</sub>/ITO and (d) Ag/TiO<sub>2</sub>-Ti<sub>3</sub>C<sub>2</sub>T<sub>x</sub>/ITO (B) CV plots and (D) EIS curves of (a) Ag/TiO<sub>2</sub>-Ti<sub>3</sub>C<sub>2</sub>T<sub>x</sub>/ITO@MIP before elution (b) Ag/TiO<sub>2</sub>-Ti<sub>3</sub>C<sub>2</sub>T<sub>x</sub>/ITO@MIP after elution (c) Ag/TiO<sub>2</sub>-Ti<sub>3</sub>C<sub>2</sub>T<sub>x</sub>/ITO@MIP after rebinding and (d) Ag/TiO<sub>2</sub>-Ti<sub>3</sub>C<sub>2</sub>T<sub>x</sub>/ITO@NIP after elution

The scan rate investigations (10 to 300 mV/s) for Ag/TiO<sub>2</sub>-Ti<sub>3</sub>C<sub>2</sub>T<sub>x</sub>/ITO@MIP electrode have been carried out by using the CV method (Fig. 6.5A). A linear correlation has been observed between peak potentials ( $E_{pa}$  and  $E_{pc}$ ) and log of the scan rate ( $v$ ) (Fig. 6.5B) for the fabricated electrode as described by the Eqs. 6.1 and 6.2.

$$E_{pa}[\text{Ag/TiO}_2\text{-Ti}_3\text{C}_2\text{T}_x/\text{ITO@MIP}] = 0.222 \text{ (V)} + 0.064 \text{ (V)} * \log [v \text{ (mV/s)}]; R^2 = 0.979 \quad (6.1)$$

$$E_{pc}[\text{Ag/TiO}_2\text{-Ti}_3\text{C}_2\text{T}_x/\text{ITO@MIP}] = 0.245 \text{ (V)} - 0.067 \text{ (V)} * \log [v \text{ (mV/s)}]; R^2 = 0.980 \quad (6.2)$$

On the basis of Laviron's equation (Eqs. 2.3 to 2.5) and slopes of the aforementioned equations, the values of  $\alpha$  and  $K_s$  are found to be 0.92 and 0.105 s<sup>-1</sup> for Ag/TiO<sub>2</sub>-Ti<sub>3</sub>C<sub>2</sub>T<sub>x</sub>/ITO@MIP electrode, respectively.

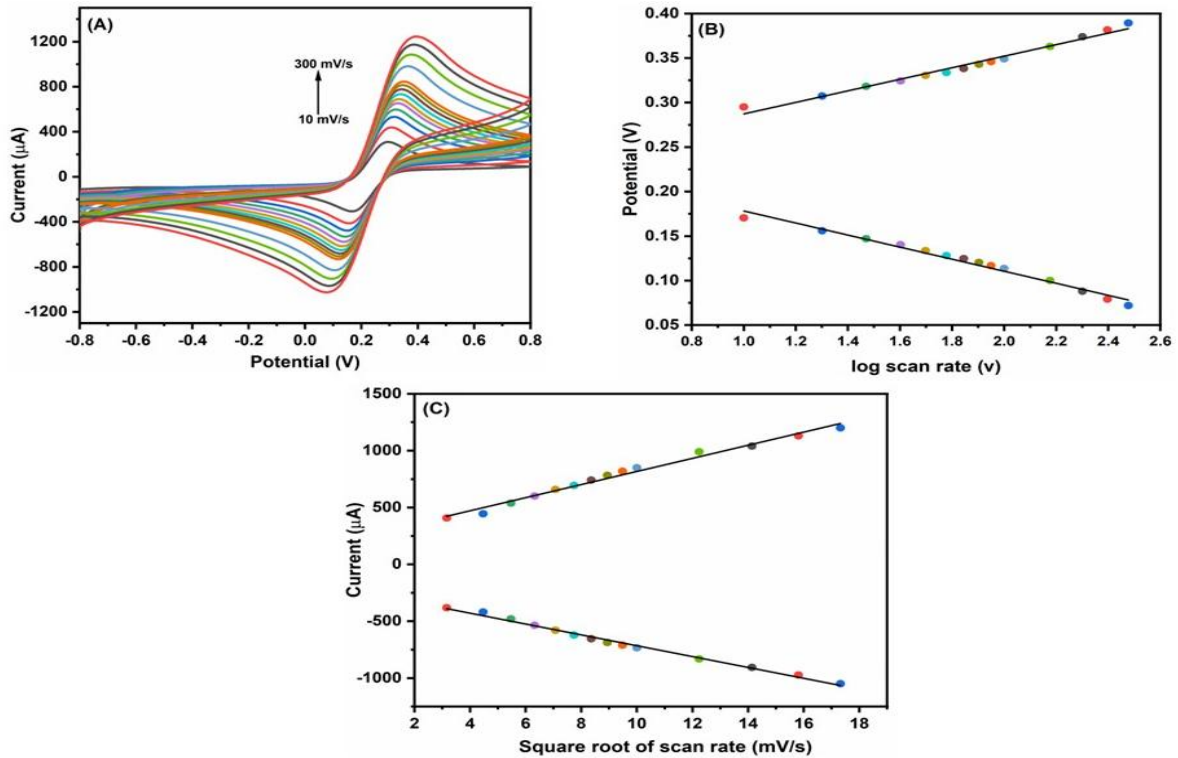


**Fig. 6.5** (A) CV curves of scan rate studies (10-300 mV/s) (B) linear curves of redox peak potential with log of scan rate and (C) linear curves of peak current vs. square root of scan rate for Ag/TiO<sub>2</sub>-Ti<sub>3</sub>C<sub>2</sub>T<sub>x</sub>/ITO@MIP electrode

Furthermore, **Fig. 6.5C** illustrates a linear relationship between the peak currents (anodic and cathodic) and square root of the corresponding scan rate for developed electrode. It makes evident that the transfer of electrons across these sensing platforms is a surface-controlled process and it obeys the Eqs. 6.3 and 6.4

$$I_{pa}[\text{Ag/TiO}_2\text{-Ti}_3\text{C}_2\text{T}_x/\text{ITO@MIP}] = 240.9 \text{ (}\mu\text{A)} + 57.6 \text{ (}\mu\text{A)} \text{ (mV/s)} * \text{(mV/s)}^{1/2} v^{1/2}; R^2 = 0.985 \quad (6.3)$$

$$I_{pc} [\text{Ag/TiO}_2\text{-Ti}_3\text{C}_2\text{T}_x\text{/ITO@MIP}] = -238.1 (\mu\text{A}) - 47.7 (\mu\text{A}) (\text{mV/s}) * (\text{mV/s})^{1/2} v^{1/2}; R^2 = 0.992 \quad (6.4)$$

Based on the above equations including Randles-Sevcik equation (Eqs. 2.6 and 2.7), the electrochemical kinetic parameters, i.e., diffusion coefficient (D), electroactive surface area (A) and average surface area ( $\tau$ ) for Ag/TiO<sub>2</sub>-Ti<sub>3</sub>C<sub>2</sub>T<sub>x</sub>/ITO@MIP electrode were calculated to be  $20.57 \times 10^{-6} \text{ cm}^2/\text{s}$ ,  $0.40 \text{ cm}^2$  and  $2.68 \times 10^{-8} \text{ mol/cm}^2$ , respectively.

### 6.3.3 Optimization of Experimental Parameters

The formation of a polymeric film on electrode surface depends on numerous factors such as the pH of electrolytic solution, the template-to-monomer ratio, number of electropolymerization cycles, effect of scan rate, elution time and incubation time. To achieve the best MIP sensor performance, these key factors were optimized by using the DPV method.

Firstly, the electrolyte's pH might affect the structural stability and molecular recognition imprinted film of the sensor. Therefore, the pH of electrolyte was optimized within the range of 5.0 to 9.0. The response peak current increases with a rise in pH from 5.0 to 7.0 as shown in **Fig. 6.6A** attaining a maximum current signal at pH 7.0 and then declines gradually with further increase in pH. This phenomenon can be attributed to the acidic or alkaline conditions which can adversely affect the structural integrity of MIP film and thus lowers the sensor's sensitivity. Hence, the pH 7.0 was selected as an optimal pH for preparing the MIP film.

Secondly, the ratio of template to functional monomers was precisely controlled which in turn affects the generation of imprinted cavities within the polymer matrix thereby influencing both the selectivity and sensitivity of MIP electrochemical sensor. Therefore, an optimization of molar ratio was conducted by varying the functional monomer (Py) concentration while keeping the template (LEV) concentration constant. As shown in **Fig.**

**6.6B**, the maximum peak current was obtained at a molar ratio of 1:6. Beyond this optimal point, the peak current significantly decreases with further increase in pyrrole concentration. This behaviour can be attributed to the limited availability of functional monomer which leads to fewer recognition sites. In contrast, an excessive monomer concentration leads to self-polymerisation thereby restricting template-monomer interactions and hindering the electron transfer process. Therefore, 1:6 was chosen as the optimum ratio for subsequent experiments.

Thirdly, electropolymerization scan cycles significantly influence the MIP film's thickness which in turn has a critical impact on sensor efficacy. **Fig. 6.6C** reveals that the maximum peak current was achieved at 10 scan cycles. The fewer scan cycles result in a thinner MIP membrane causing fewer imprinted cavities while a greater scan cycle promotes the thickness of MIP film leading to the incomplete removal of template molecules. Therefore, 10 scan cycles were determined to be the optimal conditions for MIP film growth and template accessibility.

The density of MIP film is influenced by the scan rate during the electropolymerization process. As depicted in **Fig. 6.6D**, the effect of scan rates ranging from 25 to 125 mV/s was analysed. DPV analysis reveals that the maximum current response was observed at a scan rate of 75 mV/s. Because, a lower scan rate creates a denser film that prevents template elution and reduces the number of recognition binding sites. However, a fast scan rate results in the formation of loose film with inadequate recognition cavities and poor stability. Hence, a scan rate of 75 mV/s was selected as an optimal condition.

Elution time and incubation time are the crucial steps for the fabrication of an efficient MIP sensor. As shown in **Fig. 6.6E**, the maximum current response was obtained at 10 min of elution time indicating the complete extraction of template molecules from the Ppy film and then declined further with elapsed time. This is because of the excessive prolonged

elution time can damage the polymer film structure. Thus, the ideal elution time for efficient template removal was determined to be 10 min. Furthermore, the incubation time has a direct impact on the extent of analyte binding into the MIP recognition cavities. **Fig. 6.6F** demonstrates that the peak response declines with an increase in incubation time from 5 to 25 min and the current stabilizes beyond 15 min of incubation. Therefore, 15 min was chosen as an optimized incubation time for further studies.

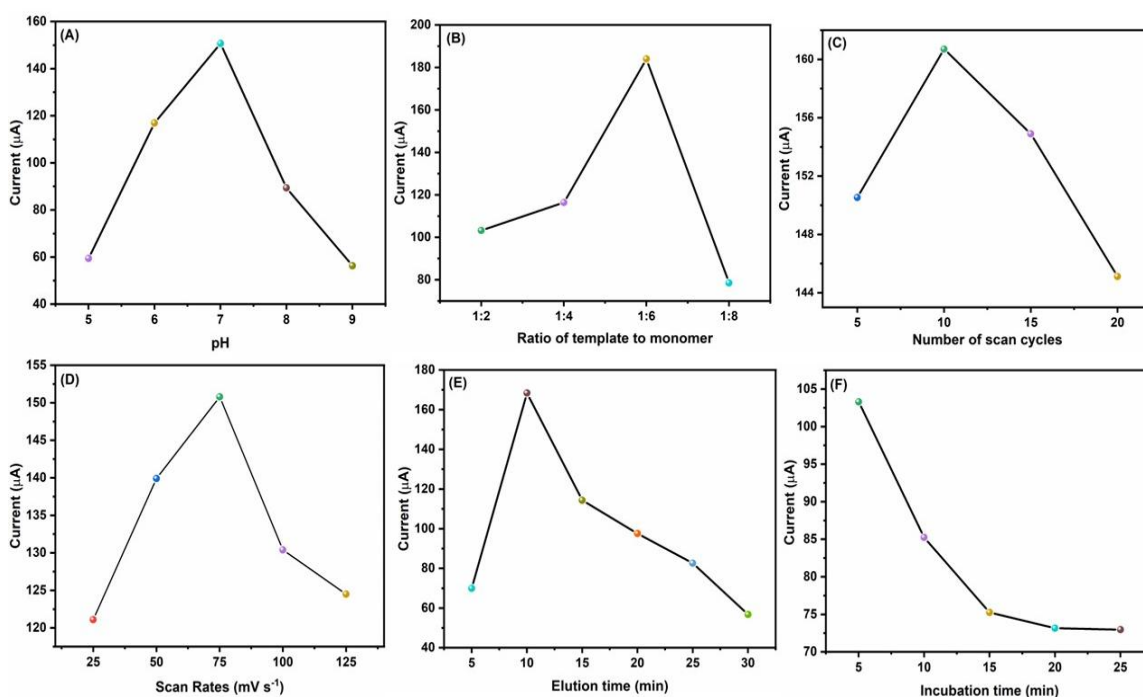


**Fig. 6.6** Optimization experimental conditions for (A) impact of pH of the electropolymerization solution (B) concentration of LEV: Pyrrole (C) electropolymerization scan cycles (D) scan rate (E) elution time and (F) incubation time

### 6.3.4 Analytical Performance of the Fabricated MIP Sensor for LEV Detection

Under the optimized experimental conditions, the DPV method was used to analyze the electrochemical behaviour of Ag/TiO<sub>2</sub>-Ti<sub>3</sub>C<sub>2</sub>T<sub>x</sub>/ITO@MIP sensor toward varying LEV concentrations (0.1 fM to 1000 nM). As depicted in **Fig. 6.7A**, the peak current declines consistently with increasing LEV concentration attributes to the occupation of imprinted

cavities by LEV molecules which hinders electron transfer at the electrode surface. A linear relation was noticed between the log of LEV concentration and the change in current response (**Fig. 6.7B**) with a linear regression equation:  $I = 15.17 \mu\text{A fM}^{-1} \times \log C_{\text{LEV}} + 29.21 \mu\text{A}$ ;  $R^2 = 0.989$ .

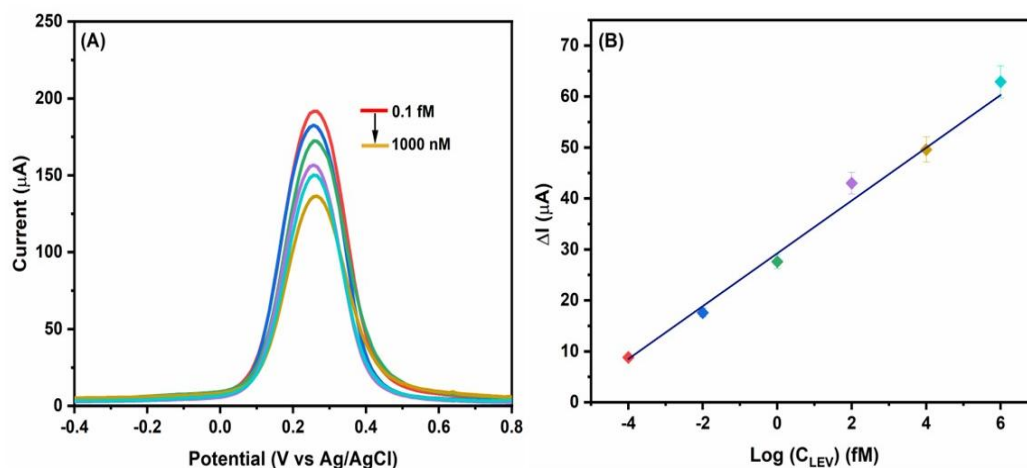


**Fig. 6.7 (A)** DPV method showing the electrochemical response of Ag/TiO<sub>2</sub>-Ti<sub>3</sub>C<sub>2</sub>T<sub>x</sub>/ITO@MIP electrode against varying concentration of LEV (0.1 fM to 1000 nM) and **(B)** Linear curve between  $\Delta I$  and the logarithm of different LEV concentrations

By employing the calibration plot slope and the effective surface area of the developed Ag/TiO<sub>2</sub>-Ti<sub>3</sub>C<sub>2</sub>T<sub>x</sub>/ITO@MIP sensor, the sensitivity was calculated to be  $43.34 \mu\text{A fM}^{-1} \text{cm}^{-2}$ . Subsequently, the low detection limit (LOD) has been calculated by using the formula  $3\sigma/\text{sensitivity}$  ( $\sigma$  is the standard deviation of intercept). The LOD is found to be 0.1 fM.

### 6.3.5 Selectivity, Reproducibility, Repeatability and Stability Analysis

The specific recognition ability of Ag/TiO<sub>2</sub>-Ti<sub>3</sub>C<sub>2</sub>T<sub>x</sub>/ITO@MIP sensor was evaluated with other interfering species that might affect the electrochemical response of LEV. Various interfering substances including ciprofloxacin (CIP), norfloxacin (NOR), omeprazole (OME), azithromycin (AZY), ampicillin (AMP), glucose (GLU), NaCl and Na<sub>2</sub>CO<sub>3</sub> at concentrations of 1 pM, were added with the coexistence of 100 pM LEV and DPV

measurements were carried out. As depicted in **Fig. 6.8A**, a 100-fold high concentration of these substances did not interfere with LEV detection. These findings demonstrate an excellent selectivity of proposed MIP sensor that is attributed to the imprinted cavities within a polymer matrix which precisely resemble the shape, size and functional groups of LEV molecules. The reproducibility of the developed sensor was examined by testing the ability of five different electrodes prepared under the same protocols to detect 1 pM of LEV using DPV (**Fig. 6.8B**).

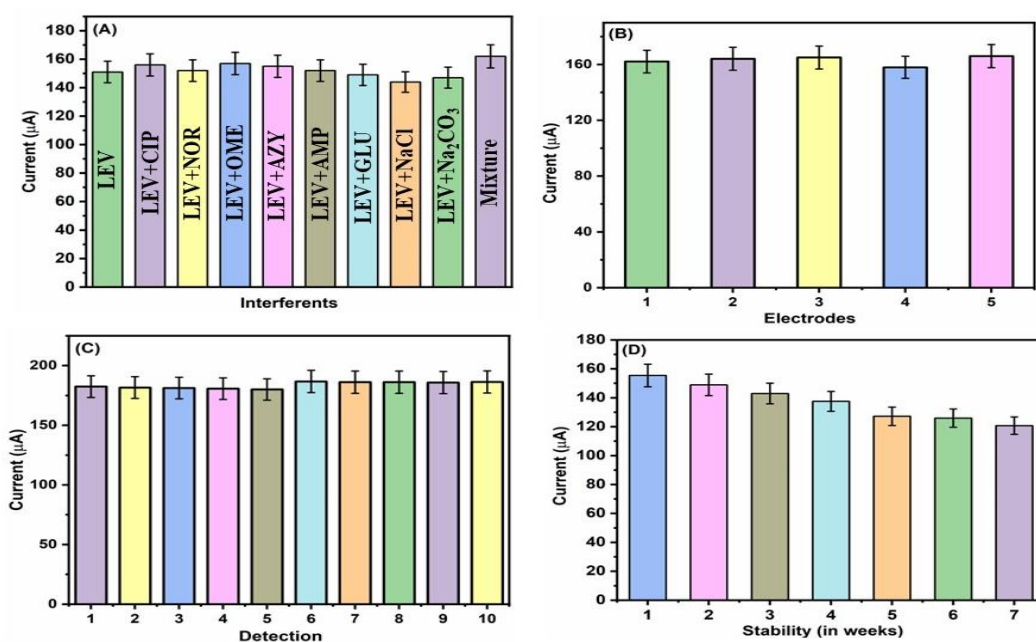


**Fig. 6.8** (A) Selectivity study of Ag/TiO<sub>2</sub>-Ti<sub>3</sub>C<sub>2</sub>T<sub>x</sub>/ITO@MIP sensor towards LEV and other interfering species (B) Reproducibility study of Ag/TiO<sub>2</sub>-Ti<sub>3</sub>C<sub>2</sub>T<sub>x</sub>/ITO@MIP sensor towards LEV using five different electrodes (C) Repeatability of Ag/TiO<sub>2</sub>-Ti<sub>3</sub>C<sub>2</sub>T<sub>x</sub>/ITO@MIP sensor for ten successive determinations of LEV on same electrode and (D) Stability of Ag/TiO<sub>2</sub>-Ti<sub>3</sub>C<sub>2</sub>T<sub>x</sub>/ITO@MIP sensor over a period of 7 weeks

The calculated relative standard deviation (RSD%) is found to be 1.94% indicating the good reproducibility of sensor for LEV sensing. To assess the repeatability of proposed sensor, ten successive measurements were performed on the same Ag/TiO<sub>2</sub>-

Ti<sub>3</sub>C<sub>2</sub>T<sub>x</sub>/ITO@MIP electrode in the presence of 1 pM LEV via DPV. As illustrated in **Fig. 6.8C**, the calculated RSD% is 1.48% verifying its good repeatability. Moreover, a long-term stability of fabricated sensor was checked over a period of 7 weeks (**Fig. 6.8D**). The DPV response of as-prepared MIP sensor for LEV was measured weekly and the results reveal that the sensor retained 87.6% of its original signal response demonstrating an acceptable stability.

### 6.3.6 Real Sample Analysis

The potential feasibility of developed Ag/TiO<sub>2</sub>-Ti<sub>3</sub>C<sub>2</sub>T<sub>x</sub>/ITO@MIP sensor for detecting LEV in milk, river water and soil samples was assessed by a standard addition method. Before measurements, the real samples were diluted 20 times with 0.1 M PBS (pH 7) and then these samples were spiked with the standard concentrations of LEV (0.1, 10 and 1000 fM) to check the sensor's performance in complex matrices.

**Table 6.1:** Data of LEV in spiked real samples using Ag/TiO<sub>2</sub>-Ti<sub>3</sub>C<sub>2</sub>T<sub>x</sub>/ITO@MIP electrode

Sample	Added (fM)	Ag/TiO <sub>2</sub> -Ti <sub>3</sub> C <sub>2</sub> T <sub>x</sub> /ITO@MIP		
		Found (fM)	Recovery (%)	RSD (%)
Milk	0	0	-	-
	0.1	0.105	92.6	3.62
	10	9.34	93.4	4.77
	1000	998	99.8	0.12
River water	0	0	-	-
	0.1	0.094	94.7	3.83
	10	9.44	94.4	4.01
	1000	964	96.4	2.52
Soil	0	0	-	-
	0.1	0.097	97.8	1.56
	10	9.91	99.1	0.61
	1000	945	94.5	3.97

As shown in **Table 6.1**, the recovery rates for the proposed MIP sensor of LEV in spiked real samples ranged from 93.4 to 105.2% with RSD% < 5%. These results validate the sensor's accuracy and applicability for monitoring LEV in diverse real samples.

## **6.4 Conclusion**

A novel and ultrasensitive Ag/TiO<sub>2</sub>-Ti<sub>3</sub>C<sub>2</sub>T<sub>x</sub> decorated MIP electrochemical sensing platform was developed for the detection of LEV. The Ag/TiO<sub>2</sub>-Ti<sub>3</sub>C<sub>2</sub>T<sub>x</sub> composite exhibits a favourable synergistic action for LEV detection owing to its high electrical conductivity, good electrocatalytic activity, large surface area and abundant binding sites for LEV adsorption. Ti<sub>3</sub>C<sub>2</sub>T<sub>x</sub>'s high conductivity, TiO<sub>2</sub>'s rich surface chemistry, and Ag's high catalytic activity provide a strong synergistic effect, thereby improving the overall sensitivity of the developed sensor. Under optimized conditions, the sensor shows an extremely low detection limit (0.1 fM) and a wide linear range (0.1 fM-1000 nM). Performance evaluation of the fabricated Ag/TiO<sub>2</sub>-Ti<sub>3</sub>C<sub>2</sub>T<sub>x</sub>/ITO@MIP sensor shows robust anti-interference ability, excellent reproducibility, good repeatability and long-term stability. Additionally, the practical applicability of the sensor was assessed by using three spiked real samples. The recovery rate is found to be in the range of 93.4 to 105.2% demonstrating the sensor's excellent potential for real-world applications.

**References**

1. B. Shobana, K. Renugadevi, and P. Prakash, Transformative microbe (E. Coli O157: H7) detection: Advancing microbial surveillance in food matrices with a photosensor of silver doped titanium dioxide/MXene nanocomposite, *Microchemical Journal*, 206 (2024) 111461.
2. E. Hou, Z. Kong, J. Wu, H. Wang, P. Nie, M. Lu, and L.Chang, Preparation of Ag–TiO<sub>2</sub>/MXene composite material for electrochemical detection of paraquat, *Journal of Materials Science: Materials in Electronics*, 34 (2023) 1177.
3. Y. Jiang, X. Zhang, L. Pei, S. Yue, L. Ma, L. Zhou, Z. Huang, Y. He, and J. Gao, Silver nanoparticles modified two-dimensional transition metal carbides as nanocarriers to fabricate acetylcholinesterase-based electrochemical biosensor, *Chemical Engineering Journal*, 339 (2018) 547-556.
4. D. Hudda, and D. Kumar, Titanium dioxide grafted MXene-based molecularly imprinted electrochemical sensor for the ultrasensitive determination of levofloxacin, *Journal of Solid State Electrochemistry*, 29 (2025) 5283-5295.
5. Sweety, D. Hudda, and D. Kumar, Ultrasensitive Electrochemical Detection of EpCAM Antigen Based on Anti-EpCAM Conjugated With Highly Flexible Ag@Ti<sub>3</sub>C<sub>2</sub>T<sub>x</sub> Modified Conducting Paper Platform, *Applied Organometallic Chemistry*, 39 (2025) e70264.
6. Sweety and D. Kumar, Development of Ti<sub>3</sub>C<sub>2</sub>T<sub>x</sub>-based novel immunosensor for cancer biomarker detection, *Applied Organometallic Chemistry*, 38 (2024) e7570.
7. D.-E. Lee, S. Moru, W.-K. Jo, and S.Tonda, Dual-cocatalyst-promoted photocatalytic treatment of persistent waterborne pollutants via in situ MXene-derived TiO<sub>2</sub>/Ti<sub>3</sub>C<sub>2</sub> hybrids with plasmonic Ag nanoparticles, *Separation and Purification Technology*, 352 (2025) 128261.

## Conclusion, Future Scope and Social Impact

---

### 7.1 Conclusion

This chapter presents the general findings of the research outcomes and discusses the potential implications for advancing current technologies towards smart applications. The work focuses on the fabrication of an efficient electrochemical sensing platform using  $\text{Ti}_3\text{C}_2\text{T}_x$  and its composites ( $\text{TiO}_2$ ,  $\text{CuS}$ , and  $\text{Ag}$  particles) using the MIP approach for the quantitative detection of an antibiotic (Levofloxacin). The synthesis, characterization and electrochemical properties of  $\text{Ti}_3\text{C}_2\text{T}_x$  and its composites as well as their potential applications in sensing have been discussed. To enhance the sensing performance, efforts have been made to adopt eco-friendly and economical approaches for synthesizing various composite materials. The fabrication of an electrochemical sensor involves the process of electrophoretic deposition of synthesized materials onto the ITO glass surface followed by the growth of MIP films on the substrate via electropolymerization technique. The fabricated MIP sensors exhibit high selectivity and sensitivity.

Firstly, a  $\text{Ti}_3\text{C}_2\text{T}_x/\text{ITO}@\text{MIP}$ -based efficient electrochemical sensing platform has been developed for the detection of antibiotic. The 2D layered structure of hydrothermally synthesised  $\text{Ti}_3\text{C}_2\text{T}_x$  exhibits superior electrical conductivity and a high surface area providing abundant binding sites for precise LEV adsorption. Under optimized experimental conditions, the fabricated sensor exhibits a low detection limit (0.76 pM) with a wide dynamic linear range (1 pM-100 nM) along with high sensitivity ( $40.20 \mu\text{A pM}^{-1} \text{cm}^{-2}$ ) for

LEV detection. Furthermore, the sensor demonstrated a good recovery rate (93.6 to 104.5%) for detecting the LEV in spiked soil and tap water samples.

To further enhance the electrochemical characteristics of  $\text{Ti}_3\text{C}_2\text{T}_x$  including surface area, stability and binding affinity towards LEV,  $\text{TiO}_2$  has been incorporated into the layers of  $\text{Ti}_3\text{C}_2\text{T}_x$ . The in-situ generated  $\text{TiO}_2$  on the  $\text{Ti}_3\text{C}_2\text{T}_x$  surface enhances the stability of the  $\text{Ti}_3\text{C}_2\text{T}_x$  by increasing the interlayer spacing thereby preventing aggregation and acting as a barrier to prevent oxidative deterioration of  $\text{Ti}_3\text{C}_2\text{T}_x$  internal structure. The electrochemical studies suggest better electron transfer ability and a high surface area for  $\text{TiO}_2$ - $\text{Ti}_3\text{C}_2\text{T}_x$  which further provides abundant imprinted cavities for the effective adsorption of LEV. The fabricated sensor under optimized analytical conditions shows a linear analytical response in linear range of 1 pM-100 nM, with a LOD of 0.41 pM. Moreover, the sensor is highly sensitive and selective towards LEV and shows acceptable stability and reproducibility. The developed sensor detected LEV in spiked biological and environmental samples with a good recovery rate.

In the next chapter, a stable  $\text{CuS}/\text{Ti}_3\text{C}_2\text{T}_x$  modified MIP-based impedimetric sensor has been developed for LEV detection. The incorporation of  $\text{CuS}$  into  $\text{Ti}_3\text{C}_2\text{T}_x$  results in a larger surface area and more active sites which promote LEV adsorption and further enhance the electrochemical signal response by improving the electron transfer kinetics. Electrochemical investigations indicate that the  $\text{MIP}/\text{CuS}/\text{Ti}_3\text{C}_2\text{T}_x$  sensor exhibits linearity over a concentration range of 0.01 pM to 1000 nM, with a detection limit of 10 fM. Moreover, the sensor has been proven to be highly specific and stable and successfully tested for LEV measurements in spiked milk and river water samples.

A novel electrochemical sensing platform has been developed using a ternary composite like  $\text{Ag}/\text{TiO}_2$ - $\text{Ti}_3\text{C}_2\text{T}_x$  for the detection of LEV. The remarkable analytical performance of sensor can be attributed to the excellent conducting and electrocatalytic properties of  $\text{Ag}/\text{TiO}_2$ -

Ti<sub>3</sub>C<sub>2</sub>T<sub>x</sub> which provide suitable imprinted sites for LEV adsorption. As a result, the developed sensor exhibits linearity over a concentration range of 0.1 fM to 1000 nM, with an extremely low detection limit of 0.1 fM. The sensor was found to be highly specific, sensitive and stable. Furthermore, the sensor's remarkable recovery rate (93.4-105.2%) for LEV detection in spiked milk, soil and river water samples validates the effectiveness of the fabricated electrode.

## **7.2 Future Scope**

Although, the levofloxacin antibiotic has been effectively detected in real samples however further research can be conducted on multiplexed detection which allows for the simultaneous measurement of multiple antibiotics. Further, the choice of functional monomers which should be determined by the structure and possible interactions of the target molecule is a crucial step in the synthesis of MIPs. Optimizing monomer selection, enhancing characteristics such as hydrophilicity and reducing nonspecific binding sites can all be achieved with the aid of computational modelling techniques. Furthermore, the incorporation of advanced nanomaterials and surface modification of MXene can significantly enhance electron transfer, sensitivity and amplify signal response thereby enabling better antibiotic recognition. Future developments could focus on integrating MIP-based sensors with microfluidic devices to fabricate a lab-on-chip platform for on-site analysis. Real-time data access through remote monitoring and the Internet of Things (IoT) can also be explored. Additionally, MIP-modified flexible and environmentally friendly paper analytical devices can be explored for the development of cost-effective and eco-friendly point-of-care devices for monitoring antibiotic residues in various complex matrices.

### 7.3 Social Impact

- ❖ Remote monitoring with these electrochemical sensors in food sources and clinical samples protects human health by lowering the misuse of antibiotics and preventing bacterial resistance.
- ❖ Use of these sensors in agricultural fields for monitoring antibiotic residues prevents pollution and protects the ecosystem.
- ❖ Diagnostics employing portable and in-situ technologies can expand accessibility in resource-limited areas.

---

## List of Publications

---

- ❖ **Divya Hudda**, Devendra Kumar, Molecularly imprinted polypyrrole decorated  $Ti_3C_2T_x$  electrochemical sensor for highly selective and sensitive detection of levofloxacin, *Journal of Materials Science*, 59 (2024) 21684-21695.
- ❖ **Divya Hudda**, Devendra Kumar, Titanium dioxide grafted MXene-based molecularly imprinted electrochemical sensor for the ultrasensitive determination of levofloxacin, *Journal of Solid State Electrochemistry*, 29 (2025) 5283-5295.
- ❖ Srijita Chatterjee, Harshita Singh, **Divya Hudda**, Sweety, Devendra Kumar, A novel acetylcholinesterase-based electrochemical biosensor using  $gC_3N_4@MoS_2$  nanohybrid for the detection of trichlorfon, *Applied Organometallic Chemistry*, 38(12) (2024) e7721.
- ❖ Poornima Bohra, Priya, Sweety, **Divya Hudda**, Devendra Kumar,  $CuS@rGO$  grafted PEDOT:PSS paper based electrochemical biosensor for fenitrothion detection, *Applied Organometallic Chemistry*, 39(2) (2025) e70002.
- ❖ Sweety, **Divya Hudda**, Devendra Kumar, A novel conducting paper-based immunosensor grafted by using  $Ag@Ti_3C_2T_x/PEDOT:PSS$  for EpCAM antigen detection, *Applied Organometallic Chemistry*, 39(7) (2025), e70264.
- ❖ Yashaswini, Sweety, **Divya Hudda**, Devendra Kumar, Non-enzymatic  $CeO_2$  grafted  $Ti_3C_2T_x$ -based electrochemical sensor for fenitrothion detection, 61(2026) 5860-5876.
- ❖ Diksha, Nishul Khanna, **Divya Hudda**, Sweety, Ritu Sharma, Devendra Kumar, MXene decorated graphitic carbon nitride-based electrochemical biosensor for the ultrasensitive determination of trichlorfon (Under revision).
- ❖ Sweety, **Divya Hudda**, Devendra Kumar, Green one-pot synthesized  $CeO_2@MXene$  coupled with molecularly imprinted polymer for the selective analysis of EpCAM as a cancer biomarker (Communicated).

- ❖ **Divya Hudda**, Sweety, Devendra Kumar, Fabrication of highly sensitive CuS@Ti<sub>3</sub>C<sub>2</sub>T<sub>x</sub> supported molecularly imprinted impedimetric sensing platform for the ultra-trace detection of levofloxacin (Communicated).
- ❖ **Divya Hudda**, Sweety, Devendra Kumar, A highly stable molecularly imprinted polymer-coated Ag/TiO<sub>2</sub>-Ti<sub>3</sub>C<sub>2</sub>T<sub>x</sub> nanohybrid electrochemical sensing platform for the selective analysis of levofloxacin determination (Communicated).
- ❖ Ritu Sharma, **Divya Hudda**, Sania Sangwan, Sanjit Nayyar, Rajinder K. Gupta, Phytochemicals, antioxidant, and antimicrobial activity of Neolamarckia cadamba Fruit (Communicated)
- ❖ **Divya Hudda**, Tanushee, Devendra Kumar, Development of highly sensitive and selective detection of levofloxacin using molecularly imprinted polymer modified Ag@Ti<sub>3</sub>C<sub>2</sub>T<sub>x</sub> (Under Preparation)

## Book Chapter

- ❖ Deeksha Thakur, **Divya Hudda**, Devendra Kumar, Yi-Ting Lai, Prateek Sharma, Quantum-Dots Based Nanocomposites as Biosensors, Quantum Dots Based Nanocomposites: Design, Fabrication and Emerging Applications, Springer, (2024) 231-255.

## Research Work Presented at Conferences

---

- ❖ Poster presentation at International Conference on Surface Chemistry, Annamalai University, Annamalainagar, India (February 2022).
- ❖ Oral presentation at International Conference on Chemical & Allied Science and their Applications, Delhi Technological University, New Delhi, India (January 2023).
- ❖ Poster presentation at 10th International Conference on Recent Advances in Agriculture, Engineering, Applied & Life Sciences for Environmental Sustainability, Uttarakhand University, Dehradun, Uttarakhand, India (October 2024).
- ❖ Poster presentation at 11th International Conference on Recent Advances in Agriculture, Biological & Applied Sciences for Eco-Friendly Development, Maya Devi University, Dehradun, Uttarakhand, India (July 2025).
- ❖ Poster presentation at International Conference on Recent Advancements in Materials and Chemical Sciences, SRM University, Sonipat, India (September 2025).



*J Mater Sci* (2024) 59:21684–21695

## Chemical routes to materials

**Molecularly imprinted polypyrrole decorated Ti<sub>3</sub>C<sub>2</sub>T<sub>x</sub> electrochemical sensor for highly selective and sensitive detection of levofloxacin**Divya Hudda<sup>1</sup> and Devendra Kumar<sup>1,\*</sup> <sup>1</sup> Department of Applied Chemistry, Delhi Technological University, Delhi 110042, India

Received: 18 April 2024

Accepted: 31 October 2024

Published online:  
27 November 2024© The Author(s), under  
exclusive licence to Springer  
Science+Business Media, LLC,  
part of Springer Nature, 2024**ABSTRACT**

Herein, a rapid and efficient molecular imprinted polymer (MIP) modified Ti<sub>3</sub>C<sub>2</sub>T<sub>x</sub>-based electrochemical sensing platform was developed for levofloxacin detection (LEV). The MIP sensor was designed by depositing the synthesized Ti<sub>3</sub>C<sub>2</sub>T<sub>x</sub> electrophoretically onto the indium tin oxide (ITO) glass surface, followed by electropolymerization of pyrrole as a monomer and LEV as a template molecule. Ti<sub>3</sub>C<sub>2</sub>T<sub>x</sub> significantly enhances the electron transfer rate and offers a larger surface area to increase the number of imprinted sites for precise recognition of LEV. The fabricated sensor (MIP/Ti<sub>3</sub>C<sub>2</sub>T<sub>x</sub>/ITO), under all optimized parameters, demonstrated superior selectivity with a low detection limit (LOD) of 0.76 pM and a linear relationship with LEV concentration ranging (1 pM–100 nM). Additionally, this newly developed sensor exhibited robust stability and sensitivity and successfully detected LEV in actual samples with satisfactory outcomes.

**Introduction**

Levofloxacin (LEV) belongs to the third generation of fluoroquinolones that exhibits high antibacterial properties and is widely utilized in both human and veterinary medicine to treat pneumonia, gastroenteritis, infections in the urinary and respiratory tract, skin, and soft tissues [1–3]. However, long-term use of LEV often increases the risk of certain health problems, including tendon damage, heart diseases, immune suppression, muscle atrophy, and abdominal discomfort. Hence, there is a need to develop a highly sensitive and reliable method for monitoring the presence

of LEV in medical, food, and environmental samples [4–6].

At present, various analytical techniques are used for LEV detection, including fluorimetry [7], flow-injection spectrophotometry [8], capillary electrophoresis [9], nuclear magnetic resonance [10], chemiluminescence [11] and high-performance liquid chromatography [12, 13]. Although these methods possess satisfactory results, even some demerits are associated with these techniques, such as costly equipment, extended analysis periods, low sensitivity, and complex sample preparation [14, 15]. In contrast, electrochemical sensors (ECS) have gained much interest due to their high sensitivity, fast response, easy operation, and low

Handling Editor: Pedro Camargo.

Address correspondence to E-mail: dkumar@dce.ac.in





# Titanium dioxide grafted MXene-based molecularly imprinted electrochemical sensor for the ultrasensitive determination of levofloxacin

Divya Hudda<sup>1</sup> · Devendra Kumar<sup>1</sup> Received: 26 March 2025 / Revised: 26 June 2025 / Accepted: 26 June 2025 / Published online: 8 July 2025  
© The Author(s), under exclusive licence to Springer-Verlag GmbH Germany, part of Springer Nature 2025

## Abstract

Levofloxacin (LEV) is widely used to treat human and animal infections. However, overuse of this antibiotic poses a risk to the ecosystem and food safety. Therefore, developing a robust analytical method to monitor LEV residues is of great importance. Herein, an efficient and highly stable molecularly imprinted polymer (MIP)-based electrochemical sensing interface has been designed by using TiO<sub>2</sub>-functionalized titanium carbide (TC) for the selective determination of LEV. The TiO<sub>2</sub>/TC hybrid was synthesized by the in situ growth of TiO<sub>2</sub> on the surface of TC sheets via a facile one-pot hydrothermal route. Subsequently, MIP films were grown on the substrate via the electropolymerization technique. The morphological, spectroscopic, and structural properties of the proposed MIP sensor were investigated using several analytical and electrochemical methods. The 2D/2D TiO<sub>2</sub>/TC hybrid improves the electrocatalytic activity and facilitates a large number of binding sites for the specific detection of LEV. Under all the optimized parameters, the fabricated sensor, i.e., MIP@TiO<sub>2</sub>/TC/ITO, exhibits high binding affinity towards LEV with a broad linear range (1 pM–100 nM), an extremely low detection limit (0.41 pM), and high sensitivity. Moreover, this sensor shows good reproducibility and long-term stability, resulting in a useful sensing platform to determine the LEV in spiked real samples with satisfactory outcomes.

**Keywords** Titanium dioxide · MXene · Levofloxacin · Polypyrrole · Molecular imprinted polymer · Electrochemical sensor

## Introduction

Antibiotics are considered to be life-saving drugs as they prevent many bacterial infections in humans and livestock [1, 2]. However, the uncontrolled use of antibiotics leads to antibacterial resistance, which has a negative impact on humans, animals, and the surrounding environment [3]. Due to the rising prevalence and incidence of antibacterial resistance globally, the precise and early identification of antibiotics has drawn considerable attention [4]. Levofloxacin (LEV;  $-(S)-9$ -fluoro-2,3-dihydro-3-methyl-10-(4-methyl-1-piperazinyl)-7-oxo-7H-pyrido[1,2,3-de]-1,4-benzoxazine-6-carboxylic acid) is a broad-spectrum third-generation fluoroquinolone antibiotic with a high bactericidal effect against both gram-positive and gram-negative bacteria [5]. It is

widely utilized in humans and veterinary to cure respiratory and urinary tract infections, pneumonia, gastroenteritis, and sinusitis [6]. Nevertheless, an overdose of LEV medication causes severe side effects, including heart problems, tendon damage, Stevens-Johnson syndrome, immune suppression, and muscle atrophy [7, 8]. Therefore, the development of a technique to monitor LEV residues in food, biological, and environmental samples is necessary for human health safety [9].

A variety of analytical methods, such as nuclear magnetic resonance [10], chemiluminescence [11], high-performance liquid chromatography [12], capillary electrophoresis [13], flow-injection spectrophotometry [14], and fluorimetry [15], have been used to determine LEV residues. Although these techniques are reliable and susceptible, they suffer from certain limitations, such as high cost, complex sample pre-treatment, expensive equipment, and low sensitivity, which restricts their practicability for onsite analysis. Therefore, electroanalytical techniques have received notable interest due to their simple procedure, fast response, portability, low cost, and high sensitivity [16–18]. However, they still lack

✉ Devendra Kumar  
dkumar@dce.ac.in

<sup>1</sup> Department of Applied Chemistry, Delhi Technological University, Delhi 110042, India



# Plagiarism Report

 Page 1 of 121 - Cover Page

Submission ID trn:oid:::27535:125306186

## Divya Hudda

### Thesis\_Final (2K20PHDAC501) - Plag.docx

 Delhi Technological University

#### Document Details

Submission ID

trn:oid:::27535:125306186

Submission Date

Dec 29, 2025, 12:37 PM GMT+5:30

Download Date

Dec 29, 2025, 12:42 PM GMT+5:30

File Name

Thesis\_Final (2K20PHDAC501) - Plag.docx

File Size

7.1 MB

111 Pages

23,051 Words

132,083 Characters

 Page 1 of 121 - Cover Page

Submission ID trn:oid:::27535:125306186



## 9% Overall Similarity

The combined total of all matches, including overlapping sources, for each database.

### Filtered from the Report

- ▶ Bibliography
- ▶ Quoted Text
- ▶ Cited Text
- ▶ Small Matches (less than 10 words)

### Match Groups

- 180 Not Cited or Quoted 9%**  
Matches with neither in-text citation nor quotation marks
- 0 Missing Quotations 0%**  
Matches that are still very similar to source material
- 0 Missing Citation 0%**  
Matches that have quotation marks, but no in-text citation
- 0 Cited and Quoted 0%**  
Matches with in-text citation present, but no quotation marks

### Top Sources

- 5% Internet sources
- 6% Publications
- 4% Submitted works (Student Papers)

### Integrity Flags

#### 0 Integrity Flags for Review

No suspicious text manipulations found.

Our system's algorithms look deeply at a document for any inconsistencies that would set it apart from a normal submission. If we notice something strange, we flag it for you to review.

A Flag is not necessarily an indicator of a problem. However, we'd recommend you focus your attention there for further review.



## Curriculum Vitae

Divya Hudda

---

Delhi Technological University, Shahbad Daultpur, Main Bawana Road, Delhi-110042

Contact: +919582902389

E-mail: [divyahooda96@gmail.com](mailto:divyahooda96@gmail.com)

DOB: February 11, 1997; Nationality: Indian

### ACADEMIC QUALIFICATIONS

---

---

- ❑ **Doctor of Philosophy** (Pursuing) from Delhi Technological University, Delhi (India)-110042  
**Thesis title:** “*Electrochemical Sensor for Antibiotic Detection*”.
- ❑ **Master of Science** (2018-2020) from the Department of Chemistry, Banasthali Vidyapith, Rajasthan (India) -304022, with distinction.
- ❑ **Bachelor of Science** (2015-2018) from School of Basic Sciences and Research (Chemistry), Sharda University, Greater Noida, Uttar Pradesh (India)-201310 with first division.

### RESEARCH HIGHLIGHTS

---

---

- Synthesis and Characterizations of 2D materials (MXene) and its composites with different metal oxides and sulfides.
- Electrochemical characterization by using CV, DPV, and EIS techniques.
- Electrochemical response studies of the MIP-electrochemical sensor for antibiotic detection.
- Selectivity, reproducibility, and real samples applicability studies of fabricated MIP- electrochemical sensor.

## INSTRUMENTAL SKILLS

---

---

Potentiostat/Galvanostat: Cyclic Voltammetry, Differential Pulse Voltammetry, Chronoamperometry, Electrochemical Impedance Spectroscopy, X-Ray Diffractometer, Fourier Transform Infrared Spectrometer.

## AWARDS

---

---

1. “Best Poster Presentation Award” was awarded in the International Conference on “Recent Advances in Agriculture, Engineering, Applied & Life Sciences for Environmental Sustainability, Uttarakhand University, Dehradun, Uttarakhand, India, during October 25-27, 2024.
2. “Commendable Research Award” in recognition of excellence in research to publish a paper, “Molecularly imprinted polypyrrole decorated  $Ti_3C_2T_x$  electrochemical sensor for highly selective and sensitive detection of levofloxacin” by Delhi Technological University, Delhi, during the year 2025.
3. Commendable Research Award” in recognition of excellence in research to publish a paper, “A novel acetylcholinesterase-based electrochemical biosensor using  $gC_3N_4@MoS_2$  nanohybrid for the detection of trichlorfon”, by Delhi Technological University, Delhi, during the year 2025.

## RESEARCH PAPERS

---

---

- ❖ **Divya Hudda**, Devendra Kumar, Molecularly imprinted polypyrrole decorated  $Ti_3C_2T_x$  electrochemical sensor for highly selective and sensitive detection of levofloxacin, Journal of Materials Science, 59 (2024) 21684-21695.
- ❖ **Divya Hudda**, Devendra Kumar, Titanium dioxide grafted MXene-based molecularly imprinted electrochemical sensor for the ultrasensitive determination of levofloxacin, Journal of Solid State Electrochemistry, 29 (2025) 5283-5295.

- ❖ Deeksha Thakur, **Divya Hudda**, Devendra Kumar, Yi-Ting Lai, Prateek Sharma, Quantum-Dots Based Nanocomposites as Biosensors, *Quantum Dots Based Nanocomposites: Design, Fabrication and Emerging Applications*, Springer, (2024) 231-255.
- ❖ Srijita Chatterjee, Harshita Singh, **Divya Hudda**, Sweety, Devendra Kumar, A novel acetylcholinesterase-based electrochemical biosensor using  $gC_3N_4@MoS_2$  nanohybrid for the detection of trichlorfon, *Applied Organometallic Chemistry*, 38(12) (2024) e7721.
- ❖ Poornima Bohra, Priya, Sweety, **Divya Hudda**, Devendra Kumar,  $CuS@rGO$  grafted PEDOT:PSS paper based electrochemical biosensor for fenitrothion detection, *Applied Organometallic Chemistry*, 39(2) (2025) e70002.
- ❖ Sweety, **Divya Hudda**, Devendra Kumar, A novel conducting paper-based immunosensor grafted by using  $Ag@Ti_3C_2T_x/PEDOT:PSS$  for EpCAM antigen detection, *Applied Organometallic Chemistry*, 39(7) (2025), e70264.
- ❖ Yashaswini, Sweety, **Divya Hudda**, Devendra Kumar, Non-enzymatic  $CeO_2$  grafted  $Ti_3C_2T_x$ -based electrochemical sensor for fenitrothion detection 61(2026) 5860-5876.
- ❖ Diksha, Nishul Khanna, **Divya Hudda**, Sweety, Ritu Sharma, Devendra Kumar, MXene decorated graphitic carbon nitride-based electrochemical biosensor for the ultrasensitive determination of trichlorfon (Under revision).
- ❖ Sweety, **Divya Hudda**, Devendra Kumar, Green one-pot synthesized  $CeO_2@MXene$  coupled with molecularly imprinted polymer for the selective analysis of EpCAM as a cancer biomarker (Communicated).
- ❖ **Divya Hudda**, Devendra Kumar, Fabrication of highly sensitive  $CuS@Ti_3C_2T_x$  supported molecularly imprinted impedimetric sensing platform for the ultra-trace detection of levofloxacin (Communicated).

- ❖ **Divya Hudda**, Devendra Kumar, A highly stable molecularly imprinted polymer-coated Ag/TiO<sub>2</sub>-Ti<sub>3</sub>C<sub>2</sub>T<sub>x</sub> nanohybrid electrochemical sensing platform for the selective analysis of levofloxacin determination (Communicated).
- ❖ Ritu Sharma, **Divya Hudda**, Sania Sangwan, Sanjit Nayyar, Rajinder K. Gupta, Phytochemicals, antioxidant, and antimicrobial activity of Neolamarckia cadamba Fruit (Communicated).
- ❖ **Divya Hudda**, Tanushee, Devendra Kumar, Development of highly sensitive and selective detection of levofloxacin using molecularly imprinted polymer modified Ag@Ti<sub>3</sub>C<sub>2</sub>T<sub>x</sub> (Communicated).

### CONFERENCES

---

- ❖ Poster presentation at International Conference on Recent Advancements in Materials and Chemical Sciences, SRM University, Sonipat, India (September 2025).
- ❖ Poster presentation at 11th International Conference on Recent Advances in Agriculture, Biological & Applied Sciences for Eco-Friendly Development, Maya Devi University, Dehradun, Uttarakhand, India (July 2025).
- ❖ Poster presentation at 10th International Conference on Recent Advances in Agriculture, Engineering, Applied & Life Sciences for Environmental Sustainability, Uttarakhand University, Dehradun, Uttarakhand, India (October 2024).
- ❖ Attended International Conference & Workshop on Addressing Antibiotics Abuse in Community using Biosensing Technologies, organized by Bhagini Nivedita College, University of Delhi, held during August 25-27, 2023.
- ❖ Oral presentation at International Conference on Chemical & Allied Science and their Applications, Delhi Technological University, New Delhi, India (January 2023).

- ❖ Poster presentation at Virtual International Conference on Surface Chemistry, Annamalai University, Annamalainagar, India (February 2022).
- ❖ Attended (online mode) the “International Conference on Materials Engineering and Characterization, organized by Mattest Research Academy, Chennai, India, held during January 28-30, 2022.
- ❖ Attended (online mode) a one-day national webinar on “Achieving Excellence in Chemistry in India in 21<sup>st</sup> Century: Challenges and Opportunities, organized by the Department of Chemistry, Zakir Hussain Delhi College, University of Delhi, India, held on 18<sup>th</sup> January, 2022.

#### **ACADEMIC EXPERIENCE (During PhD)**

---

1. B.Tech. Lab (AC101 Chemistry), B.Tech. 1<sup>st</sup> year: January 2022–April 2022, Delhi Technological University, New Delhi.
2. B.Tech. Lab (AC102 Chemistry), B.Tech. 1<sup>st</sup> year: May 2022–August 2022, Delhi Technological University, New Delhi.
3. B.Tech. Lab (AC101 Chemistry), B.Tech. 1<sup>st</sup> year: November 2022–March 2023, Delhi Technological University, New Delhi.
4. B.Tech. Lab (AC102 Chemistry), B.Tech. 1<sup>st</sup> year: March 2023–June 2023, Delhi Technological University, New Delhi.
5. B.Tech. Lab (AC101 Chemistry), B.Tech. 1<sup>st</sup> year: January 2022–April 2022, Delhi Technological University, New Delhi.
6. M.Sc. Lab (MSCH-209c), M.Sc. 2<sup>nd</sup> year: August 2023–November 2023, Delhi Technological University, New Delhi.

7. M.Sc. Lab (MSCH-108), M.Sc. 1<sup>st</sup> year: January 2024–May 2024, Delhi Technological University, New Delhi.
8. B.Tech. Lab (CH208), B.Tech. 1<sup>st</sup> year: January 2025–May 2025, Delhi Technological University, New Delhi.
9. B.Tech. Lab (AC101 Chemistry), B.Tech. 1<sup>st</sup> year: July 2025–November 2025, Delhi Technological University, New Delhi.